ABSTRACT

Title of Document: THE ROLE OF NEGATIVE BUOYANCY AND URBANIZATION IN WARM SEASON PRECIPITATION PROCESSES OVER THE U.S.

Manisha Ganeshan, Doctor of Philosophy, 2013

Directed By: Prof. Murtugudde, Department of Atmospheric and Oceanic Science

This thesis investigates some important processes for better understanding and modeling warm season rainfall characteristics over the US. In the first part, the causes for commonly observed biases in the simulation of the diurnal cycle of warm season rainfall are explored. Model sensitivity analyses are carried out to identify potential deficiencies in two popular cumulus parameterization schemes, viz. Betts-Miller-Janjić (BMJ) and Kain-Fritsch (KF) schemes, considered suitable for use in mesoscale simulations. A novel approach using remote sensing observations to better understand the relevant trigger processes for convection is demonstrated. The convective trigger in both schemes is found to include weak, implicit constraints above the lifting condensation level (LCL), which may contribute to premature, light rain. In order to adjust for this behavior, a simple modification is made to the KF scheme to allow moist convection to begin only from the level of free convection (LFC). Even with the seemingly strict constraint, the scheme performs adequately in a

mesoscale seasonal simulation producing an improvement in the nocturnal phase propagation of rainfall in the Central Plains region. The resolvable processes in the mesoscale model are able to overcome the negative buoyancy below the LFC, thereby reducing biases caused by sensitivity of the scheme's trigger to the grid-scale forcing at the LCL. In the future, such a modified scheme will be tested in regional and global simulations, to evaluate its robustness in varying convective regimes.

In the second part of this thesis, a multi-city analysis using high-resolution surface observations over the US, investigates the impact of the Urban Heat Island (UHI) on warm season precipitation. Statistical methods are employed to study the rainfall anomalies associated with propagating and non-propagating storms. A strong variability is observed in the UHI-influence on rainfall based on geographical setting and diurnal forcing mechanisms. Coastal cities may experience a more pronounced positive rainfall anomaly during daytime due to the UHI-sea breeze (or lake breeze) interaction. Apart from the late-afternoon rainfall enhancement, a nocturnal rainfall increase occurs over and downwind of inland cities. The nocturnal urban instability, and its interaction with propagating thunderstorms, is explored in detail using model sensitivity analyses. It appears that urban areas act as "hot spots" during the nighttime favoring convergence of propagating storm cells due to the UHI and enhanced frictional drag. In the future, a better understanding of the contribution of thermal and dynamical effects is needed while planning strategies to reduce the urban land cover impact on climate. The results of this study also suggest that the varying influence of the UHI for coastal and inland cities must be further investigated for improving forecasts, urban water resources management, flood disaster planning, etc.

THE ROLE OF NEGATIVE BUOYANCY AND URBANIZATION IN WARM SEASON PRECIPITATION PROCESSES OVER THE U. S.

By

Manisha Ganeshan

Dissertation submitted to the Faculty of the Graduate School of the
University of Maryland, College Park, in partial fulfillment
of the requirements for the degree of
Doctor of Philosophy
2013

Advisory Committee:
Professor Raghu Murtugudde, Chair
Dr. Marc Imhoff
Professor Da-Lin Zhang
Professor Xin-Zhong Liang
Adjunct Professor Vernon Kousky
Associate Professor Michael Evans

Acknowledgements

I would like to thank my advisor, Prof. Raghu Murtugudde, for being encouraging, patient, and extremely cooperative as my mentor through graduate school. I am especially grateful to him for giving me immense freedom to pursue my research ideas while ensuring that I deliver timely progress. His insight on diverse research topics has helped me adopt a broad outlook and holistic approach towards my work. I would also like to thank my committee members for their useful comments and timely advice at the initial stages of my research. I want to express gratitude to Dr. Marc Imhoff for giving me an opportunity to involve in urban-climate studies, and for being a constant support while reviewing journal manuscripts and writing job recommendations for me. I would also like to thank Dr. John Strack who has been invaluable in giving me technical guidance with WRF, as well as other professional assistance. I'm grateful to Dr. Phil Arkin and others at ESSIC for funding my visit to CIMSS (Madison, WI) where I had the great opportunity to learn remote sensing techniques from Dr. Elizabeth Weisz and her team. I would like to thank the NASA GSFC/ESSIC fellowship program for providing me with impressive computational facilities to perform research.

I'll always remain indebted to the staff, faculty, professors, and colleagues, at ESSIC and AOSC Department for being wonderfully generous and helpful at all times. Lastly, I'd like to thank my family, friends and especially my parents, for being highly accommodating and supportive throughout my academic journey.

Table of Contents

List of Tables

List of Figures

Chapter 1: Introduction

1.1 Negative Buoyancy and its representation in cumulus parameterization schemes

Atmospheric moist convection is broadly classified into two categories (Type I and Type II). Although simplistic, such a classification is typically used to represent sub-grid scale convective processes within numerical models. Type II is used for closure assumptions in most cumulus parameterization schemes. It assumes statistical equilibrium between small-scale convection and the large-scale environment. In order to maintain a nearly negligible rate of change of convective available potential energy ($\Delta CAPE/\Delta t \approx 0$), cumulus schemes based on statistical equilibrium may initiate moist convection whenever there is large-scale destabilization (increase in CAPE) due to processes such as radiative cooling, moisture advection, increased surface sensible and latent heat fluxes, etc. (Emanuel 1994). Examples of such schemes include Manabe (Manabe et al. 1965), Arakawa-Schubert (Arakawa 1969; Arakawa and Schubert 1974), Grell (Grell et al. 1991; Grell 1988; 1993), and so on. These schemes may work favorably for particular types of convective regime, for example, in tropical maritime regions where convection may be continually produced whenever there is external forcing. This equilibrium response to the large-scale environment is referred to as convective adjustment. In midlatitudes, the problem of convective initiation, however, is more constrained because external forcing is not the only limiting factor (Banacoz and Schultz 2005). The presence of negative buoyancy (or convective inhibition; CIN) below the level of free convection (LFC), allows the potential energy to build-up

substantially ($\Delta CAPE/\Delta t > 0$) before it is released. This type of non-equilibrium convection (Type I), referred to as triggered or activated, can be far more challenging to predict (Emanuel 1994). In order to represent Type I convection in cumulus schemes, the response to the large-scale forcing is delayed, either by relaxing the time period for convective adjustment or by imposing additional trigger criteria for convective initiation. For example, schemes such as the Betts-Miller-Janjić (Betts 1986; Betts and Miller 1986; Janjić 1994), Kain-Fritsch (Kain and Fritch 1993; Kain 2004), and Tiedtke (Tiedtke 1989), use a trigger function that takes into account thermodynamic constraints (CIN). In recent years, a number of schemes have transitioned from representing a purely diagnostic, instantaneous convective response (equilibrium) to a triggered or relaxed adjustment to the large-scale destabilization (disequilibrium). Such a shift towards a more prognostic approach is considered useful for parameterizing convection in the current generation mesoscale models (Jones and Randall 2011; Arakawa 2004; Kain and Fritsch 1992).

This is because, with increasing model resolution (along with a vastly growing suite of observations), the robustness of statistical or quasi-equilibrium is tested and debated (Davies et al. 2013; Jones and Randall 2011; Zhang 2002; Masunaga 2012). In general, this assumption is found to be more suitable for coarse resolution climate models characterized by *slow-varying* dynamical processes (Jones and Randall 2011; Davies et al. 2013). It has been observed that convective quasi-equilibrium is valid only when the time-scale for variation in the resolved (large-scale) forcing is longer than 30 hours (Jones and Randall 2011). This implies that the assumption, although useful for coarse resolution models, may not be adequate to represent the diurnal cycle

of convection (Jones and Randall 2011; Bechtold et al. 2013; Davies et al. 2013). Within the mesoscale modeling framework, high-frequency interaction between the grid-resolved forcing and cumulus clouds is common (Jones and Randall 2011; Kain and Fritsch 1992). At this resolution, the diurnal cycle of rainfall is considered to be better represented using the non-equilibrium assumption (Jones and Randall 2011; Davies et al. 2013; Bechtold et al. 2013). For this purpose, apart from considering the grid-resolved forcing, many cumulus schemes designed for use in mesoscale models may include implicit or explicit trigger constraints for CIN below the LFC (Kain and Fritsch 1992). In this thesis, these constraints are explored for two such cumulus parameterization schemes, namely the Kain-Fritsch and the Betts-Miller-Janjić.

Even with the additional trigger criteria, models have considerable difficulty simulating the diurnal cycle of warm season precipitation. In a recent climate modeling experiment, a premature peak in daytime warm season rainfall was predicted over the continental US using the Tiedtke scheme at resolutions ranging from 125 km to 10 km (Dirmeyer et al. 2010). Moreover, nocturnal rainfall was hardly captured in regions such as the US Central Plains, and the scheme's performance showed little sensitivity to horizontal resolution (Dirmeyer et al. 2010). In another mesoscale climate modeling experiment it was found that the Kain-Fritsch scheme is also geographically phase-locked, producing widespread daytime convection over the US (Liang et al. 2004).

The Grell scheme, on the contrary, is able to reproduce nocturnal precipitation and phase propagation across the Central Plains region (Liang et al. 2004; see Fig. 1.1 (c) and (d)). Zhang (2002; 2003) suggested a revised quasi-equilibrium assumption,

more sensitive to the free-tropospheric forcing (above the planetary boundary layer), for simulating nocturnal rainfall over this region. Similarly, Lee et al. (2008) also found that decoupling convection from the boundary layer is important for parameterizing nocturnal convective rainfall. However, such an assumption may not be appropriate for other midlatitude regions where boundary layer convection is known to produce a characteristic late afternoon rainfall maximum. For these regions, the daytime rainfall peak simulated by the Kain-Fritsch scheme agrees well with observations (Liang et al. 2004).

Thus, the Kain-Fritsch scheme's trigger function, although better designed to represent non-equilibrium convection and the diurnal cycle in mesoscale models (Kain and Fritch 1992), is only able to reproduce the daytime (not nocturnal) rainfall peak. The Tiedtke scheme also has similar biases, moreover, producing a premature peak in daytime convection (Dirmeyer et al. 2010). This suggests that the trigger constraints in these schemes, especially the role of negative buoyancy (or CIN), need further exploration. The Kain-Fritsch and Tiedtke schemes initiate moist convection based on dynamical constraints of grid-resolved mass and moisture convergence, respectively. They explicitly consider parcel buoyancy as a trigger criterion. The Tiedtke scheme, for example, assumes that the parcel's kinetic energy allows a constant additional positive buoyancy of 0.5 °K in the sub-cloud layer, i.e., the layer below the lifting condensation level (LCL) (Tiedtke 1989). The Kain-Fritsch scheme has a more sophisticated buoyancy trigger applied at the cloud-base, which incorporates the grid-resolved vertical velocity (horizontal mass convergence) in the parcel buoyancy equation (Kain 2004). Moist convection is allowed to begin at the LCL in both

schemes, with less stringent constraints on the negative buoyancy (CIN) above this level. This is discussed in more detail for the Kain-Fritsch scheme in Chapter 2. The efficiency of the trigger function in the Betts-Miller-Janjić scheme, which implicitly considers negative buoyancy based on enthalpy conservation, is also explored.

Not only is the consideration of negative buoyancy theoretically important for non-equilibrium convection, but it may have an actual influence on the diurnal cycle of warm season rainfall in mesoscale climate simulations. In Chapter 2, it is argued that the role of negative buoyancy in modeling mesoscale convection may be more critical than its current representation in cumulus schemes.

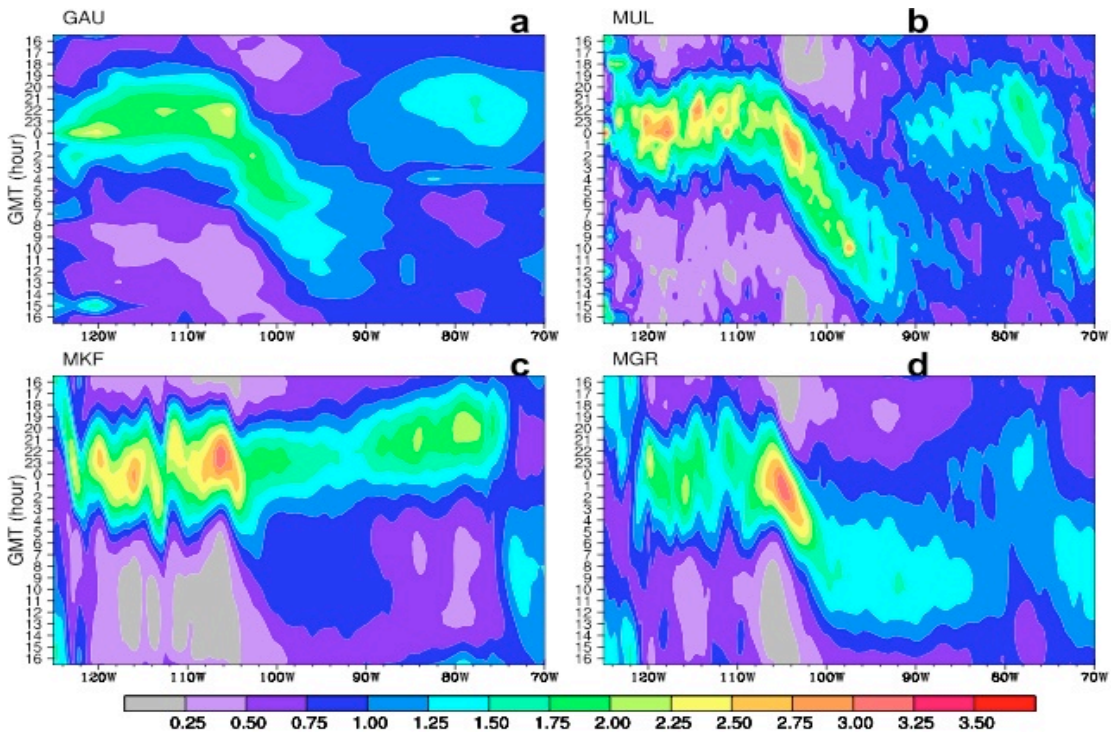

Figure 1.1 Hovmöller diagram (time versus longitude) of normalized rainfall diurnal variations averaged between 38-42°N from (a) rain-gauge records, (b) multi-sensor Stage IV precipitation observations, (c) model simulations using Kain-Fritsch scheme, and (d) model simulations using Grell scheme (from Liang et al. 2004).

1.2 The Urban Heat Island (UHI) and its impact on warm season precipitation

1.2.1 The Urban Heat Island

The Urban Heat Island, or UHI, is a commonly used term to denote the surface air temperature difference between a city and its surrounding rural environment (Oke 1973, 1982; Shepherd 2005). Construction materials used in the built environment have low albedo but high thermal conductivity, and therefore absorb more of the incoming shortwave radiation as compared to bare soil and naturally vegetated surfaces. As a result, the surface energy balance (Eq. 1.1) over urban regions may have considerable differences compared to its rural counterpart.

$$Q_{net} + Q_H + Q_E + A + \Delta Q_s = 0. \quad (1.1)$$

For the daytime urban environment, Q_{net} represents the net incoming radiation (shortwave + longwave), Q_H and Q_E are the turbulent sensible and latent heat fluxes from the ground to the atmosphere, A is the anthropogenic heat input from vehicular emissions, space cooling, industrial processes, etc., and ΔQ_s is the change in the storage heat flux. Although ΔQ_s refers to the net heat stored within the urban canopy, its major component is the surface to subsurface ground heat flux (G) (Grimmond and Oke 1995). It is assumed that Eq. 1.1 is balanced with respect to an equilibrium temperature at the surface.

Urban areas have higher ΔQ_s since impervious surfaces are typically more dense and better thermal conductors compared to loose soil (Grimmond and Oke 1999a). The skin temperature difference between the urban and rural regions is greatest during the afternoon when the incoming solar radiation is at its maximum

(Imhoff et al. 2010). At this time, the difference in the Bowen ratio (Q_H/Q_E) between the city and its surrounding rural environment may drive an atmospheric UHI. Urban areas are known to have higher sensible heat flux that warms the atmosphere, accompanied by lower latent heat flux that reduces evaporative cooling during the day (Grimmond and Oke 1995; Oke 1988; Oleson et al. 2008). The difference in air temperatures (i.e., the UHI), however, is known to peak at night (Oke 1973; Shepherd 2005; Chandler 1967).

The dominant terms in the nighttime surface energy budget (Eq. 1.1) are the net outgoing longwave radiation (Q_{net}), and ΔQ_s. The latter is mainly comprised of the upward heat flux from the subsurface to the surface (G). Sensible and latent heat fluxes are low in magnitude during nocturnal hours (Grimmond and Oke 2002). In rural areas, Q_H may turn negative as the radiation inversion may keep the nocturnal atmosphere warmer than the ground. However, for an urban area, G is quite pronounced and may continue to keep the temperature of the surface (skin) higher than the overlying air. Thus, Q_H may remain largely positive during nighttime in the built environment, thereby leading to anomalous warming of the nocturnal atmosphere (Oke 1988; Grimmond and Oke 2002).

The main sources of the nighttime Q_{net} are upwelling radiation from the ground, downwelling radiation from clouds and downwelling radiation from the atmosphere, mainly water vapor. In urban areas, a fourth source is the downwelling longwave radiation from vertical structures such as buildings which can further enhance the UHI. The warming effect of clouds and water vapor in the nocturnal atmosphere has been well documented in the literature and quantified by empirical

formulae (Swinbank 1963; Goforth et al. 2002). Clouds can substantially abate radiational losses in both the urban and the rural atmosphere, increasing nocturnal temperatures. Therefore, it is not surprising that the nocturnal peak in the UHI is most prominent during dry, cloud-free nights when the *differential* radiative cooling between urban and rural areas is maximum. In a number of previous studies, the nighttime UHI is indeed shown to be negatively correlated with cloud cover and humidity (Sundborg 1950; Duckworth and Sandberg 1954; Morris et al. 2001; Sheridan et al. 2000).

Thus, the atmospheric UHI may be distinguished from external influences resulting from topography, elevation, wind advection, etc., through the use of certain relations established *a priori.* In Chapter 3, the temperature anomaly (TA) between 28 prominent US cities and their rural environment is investigated for the presence of a distinct UHI signal. After identifying these cities, the UHI-influence on local and non-local warm season rainfall modification is examined.

1.2.2 Rainfall modification by urban areas

The warm season rainfall modification over urban areas has been investigated by several studies in the past. Changnon (1968) was one of the first to report a significant downwind rainfall increase in the La Porte region to the east of Chicago. Thereafter, similar rainfall increases observed over and downwind of many cities have been attributed mainly to the UHI (Ackerman et al. 1977; Shepherd et al. 2002; Shepherd and Burian 2003; Bornstein and Lin 2000; Dixon and Mote 2003; Bentley et al. 2010), but also to factors such as urban-enhanced aerosols (Diem and Brown 2003; Molders and Olson 2004, Van Den Heever and Cotton 2007), surface roughness

(Ackerman et al. 1977; Changnon et al. 1981; Bentley et al. 2010), and urban canyon (geometry) effects (Bornstein and LeRoy 1990; Niyogi et al. 2011; Bentley et al. 2010). The role of aerosols and increased cloud condensation nuclei (CCN) in influencing urban rainfall, however, remains uncertain (Shepherd 2005); some studies suggest a decrease in precipitation due to increased CCN (Ramanathan et al. 2001; Rosenfeld 1999, 2000; Givati and Rosenfeld 2004) whereas others indicate an opposite effect (Andreae et al. 2004; Rosenfeld et al. 2008). A recent modeling study (Van Den Heever and Cotton 2007) showed that the aerosol impact may produce enhanced downwind rainfall but the development of convection itself occurs due to the presence of the urban land cover and the associated surface convergence. Model dependence of these findings has not been explored yet.

The positive influence of the urban land cover on rainfall was first explained during METROMEX (Ackerman et al. 1977) and has since been confirmed by several subsequent modeling studies (Vukovich and Dunn 1978; Hjemfelt 1982; Baik et al. 2001). The rainfall increase has been proposed to occur due to enhanced convergence within the urban planetary boundary layer (PBL) as a result of the UHI and increased surface roughness (Ackerman et al. 1977). This leads to deeper mixing heights, more upward vertical velocity at cloud-base, and a downstream propagation of clouds and an instability along with a synoptic flow (Ackerman et al. 1977). This UHI-perturbed boundary layer circulation, observed typically during the afternoon period, invigorates existing storms but may also initiate new daytime convection (Ackerman et al. 1977, Shepherd 2005). This is one of the most well-known, commonly attributed causes for the enhanced rainfall observed over and downwind of cities (Ackerman et al. 1977;

Westcott 1995; Shepherd 2005; Shepherd et al. 2002; Shepherd and Burian 2003; Bentley et al. 2010). Even as observational evidence for this UHI-signature is building steadily, it has become increasingly important to carry out studies that investigate the role of the competing mechanisms. Factors such as varying synoptic conditions, differing storm-types, diversity in geographical setting of cities, and diurnal forcing mechanisms, warrant a detailed investigation of the old and new hypotheses for urban rainfall enhancement.

In recent decades, studies have made use of advanced high-resolution radar, lightning and rainfall datasets to investigate urban impacts on rainfall. Although useful, many of these studies only speculate about the causes for the observed spatial rainfall patterns based on previously established mechanisms (Shepherd et al. 2002; Shepherd and Burian 2003; Bentley et al. 2010; Ashley et al. 2012). Very few have actively pursued the identification of new hypotheses to explain the variability in UHI-rainfall impacts. Apart from studying rainfall patterns using the high spatial resolution of recent datasets, temporal analyses may help identify forcing mechanisms that enhance rainfall. For example, a diurnal trend analysis of the rainfall anomalies may determine whether the nocturnal UHI or the daytime UHI-perturbed boundary layer circulation drives the observed rainfall patterns. This has been carried out in the past (Ackerman et al. 1977; Huff and Changnon 1973; Westcott 1995), but is glaringly absent in more recent work that has mainly focused on analyzing spatial trends (Shepherd et al. 2002; Shepherd and Burian 2003; Bentley et al. 2010; Ashley et al. 2012). Some studies though have conducted more comprehensive analyses to understand the variability in rainfall anomalies. For example, Bornstein and LeRoy

(1990) have used radar data to show that propagating thunderstorms tend to bifurcate around New York City due to the building-barrier effect whereas rainfall can be initiated over the city under calm conditions. Niyogi et al. (2011) found that daytime thunderstorms passing through Indianapolis changed structure by splitting upwind and merging again downwind of the city. These studies do engender new hypotheses for urban modification of rainfall, but may be specific to individual cities and urban geometry. The results are not confined to discussing UHI impacts alone, and may therefore not be widely applicable.

Another issue that imposes a geographical constraint on the choice of cities for investigation is the difficulty in separating urban impacts from other local influences (such as sea breeze, topographical effects, etc.). For instance, a number of studies have been conducted over Atlanta because of its rapid urbanization in recent decades, relatively flat topography, and inland location. Bornstein and Lin (1990) showed that summer thunderstorm initiation may occur due to the UHI-induced convergence over Atlanta. Following this, recent studies over Atlanta have focused on investigating spatial rainfall distribution on synoptically benign days that are suitable for convective development (Dixon and Mote 2003; Bentley et al 2010). While it is useful to study the UHI's role in triggering air-mass type convection that is common in the southeast US, it is also worth exploiting high-resolution datasets to study the impacts on frontal storms and existing convective systems more common in other regions. These may have potentially severe risks such as flash floods and extreme rainfall. Moreover, apart from considering isolated cities like Atlanta, it is important to expand our understanding of UHI impacts on rainfall for cities located along coastlines and

complex terrain. A large coastal city may have a more significant UHI than an isolated but smaller inland city (Landsberg 1981). Therefore, such cities must not be excluded from investigating UHI-induced rainfall modification patterns. A comprehensive multi-city analysis using high-resolution datasets to explore the variability of UHI impacts on rainfall is currently lacking. In Chapter 3, the objective is to achieve the same without being too restrictive in the choice of cities and synoptic background conditions. The cities are chosen based on the occurrence of a well-defined UHI as opposed to size or favorable geographical location. In Chapter 4, modeling analyses are used to verify the observations from Chapter 3, and to test new hypotheses. The focus is on better understanding the impact of the UHI on nocturnal propagating thunderstorms. This has not been explored in detail in the past. Since the nocturnal UHI is a commonly observed phenomenon across the world, its interaction with existing rain-producing storms may have broad implications for our predictive understanding as well as for urban planning.

1.3 Thesis Outline

In Chapter 2, the cause of common biases in modeling warm season midlatitude convection is investigated through model sensitivity analyses. Several case studies are simulated to understand the deficiencies in two cumulus parameterization schemes popularly used in mesoscale modeling. The use of remote sensing observations to explore important trigger mechanisms in the atmosphere is demonstrated. It is shown that the problem of premature, light rainfall in mesoscale models may be related to the less stringent constraints on negative buoyancy,

especially in the layer between the LCL and the LFC. A simple modification is made to one of the schemes, and the scope for improvement in warm season rainfall characteristics is investigated using a mesoscale seasonal simulation.

In Chapter 3, a multi-city approach is adopted for studying the UHI-induced warm season rainfall modification by using surface observations of high spatiotemporal resolution. Statistical methods are employed to study UHI impacts on rainfall and its variability, by taking into account factors such as diurnal forcing mechanisms, geographical location (coastal versus inland), and predominant storm-type (propagating versus non-propagating). It is shown that UHI-induced rainfall modification may differ for coastal versus inland cities. For inland cities, the urban and downwind rainfall increase is shown to be significant during late-afternoon and nocturnal hours. The urban nocturnal instability has received considerably less attention in the past. In Chapter 4, the mechanisms that produce this instability and the related rainfall enhancement are investigated using model sensitivity experiments. Chapter 5 summarizes the significance of the results, and outlines the steps for future work.

Chapter 2: Negative buoyancy in midlatitude convection and its representation in cumulus parameterization schemes

Abstract

In this study, the premature onset and peak of parameterized convection in mesoscale models is investigated. Several warm-season, late-afternoon precipitation events over the Chesapeake Bay watershed are simulated using the Weather Research and Forecast (WRF) model. The performance of two popular cumulus parameterization schemes (Betts-Miller-Janjić and Kain-Fritsch) is evaluated through model sensitivity experiments. It is observed that the timing of rainfall is improved when convection is explicitly resolved. The early bias in parameterized convection appears to be associated with the inadequacy in representing CIN or negative buoyancy in the trigger, especially above cloud-base and below the level of free convection (LFC). Satellite-derived soundings suggest that even with extremely favorable conditions, negative buoyancy in this layer may delay the onset of surface-based or boundary layer convection. Other factors, such as enhanced mixing due to overactive shallow convection, may also contribute to the early rainfall bias. A simple modification to the Kain-Fritsch scheme suggests that more stringent buoyancy constraints may help reduce the bias, producing a small but positive improvement in the representation of the diurnal cycle of rainfall in mesoscale models. The scheme's performance, however, remains highly sensitive to the choice of the large-scale dynamical trigger. Stricter negative buoyancy constraints appear to reduce this sensitivity, but may not be sufficient to rectify all biases related to parameterized convection.

2.1 Introduction

An accurate representation of warm season rainfall remains a challenging issue for both regional and global climate models. In particular, the premature onset of convection and the occurrence of too frequent light rain are widely observed (Lee et al. 2007; Dai and Trenberth 2004). For example, authors have reported that the peak associated with daytime convection is predicted to occur too early in the morning hours by several cumulus parameterization schemes (e.g., Betts and Jakob 2002; Dai and Trenberth 2004; Lee et al. 2007; Dirmeyer et al. 2010). Dai and Trenberth (2004) speculated that weak thermodynamic constraints for CIN in the trigger for deep convection may be responsible for this, however, they did not explore the cause. Our current understanding of the importance of CIN or negative buoyancy for parameterizing convection in mesoscale models has been discussed in the Introduction (Chapter 1). The aim of this study is to investigate the constraints for the same in two cumulus schemes, using model sensitivity experiments and satellite observations. The rationale for the procedure adopted is outlined below.

The cause for premature convection in the Betts-Miller-Janjić (Betts 1986; Betts and Miller 1986; Janjić 1994) scheme and the Kain-Fritsch (Kain 2004) scheme is investigated by carrying out model simulations over the Chesapeake Bay watershed. The nature of warm season late-afternoon convection over this region is expected to be surface-based, i.e., driven due to boundary layer processes (Wallace 1975; Colman 1990). As discussed in Section 1.1, both schemes include a trigger function which is considered suitable for use in mesoscale models. The model runs are tested for sensitivity to horizontal resolution, treatment of convection (cumulus scheme on/off),

boundary layer physics, and cumulus physics. The important trigger mechanisms for initiating surface-based convection in the real atmosphere are also examined using satellite-derived soundings. Finally, a simple modification to the Kain-Fritsch scheme to include a more stringent buoyancy constraint for moist convection is proposed and tested using a seasonal climate simulation. The experimental procedure is explained in the next section, followed by a discussion of major results (section 2.3) and a summary of conclusions (section 2.4).

2.2 Methods

The methodology used to conduct model sensitivity experiments is described in this section, followed by the procedure to validate model results against rainfall observations and satellite-derived soundings.

2.2.1 Selection of events

Six daytime precipitation events of 1-2 day duration occurring over the Chesapeake Bay watershed during the warm season in a conditionally unstable atmosphere, and having rainfall beginning around 1200-1400 LST, are selected. In order to avoid selecting events of elevated convection (originating above the boundary layer), it is ensured that there was no upper-level disturbance in the form of thermal or vorticity advection, and also that precipitation did not occur on the cold side of a front. The convective to total precipitation ratio produced by the cumulus scheme during the time of convection is examined, and the cases are restricted to a minimum threshold ratio of 0.4. Analyses of surface and upper-air circulation for each event are carried

out using weather maps obtained from the Hydrometeorological Prediction Center (HPC) of the National Weather Service, and Unisys weather. Table 2.1 provides a list of meteorological conditions including the range of diurnal temperature maxima, surface dew point temperatures, and lifted index values observed across the region on each rain day, along with fronts at 0800 LST.

Table 2.1 The range of observed meteorological conditions over the Chesapeake Bay watershed.

Event	Diurnal Maximum Temp. (°C)	Dewpoint Temp. at 0800 LST (°C)	*Lifted Index at 0800 LST (°C)	Fronts at 0800 LST
Aug 4-5, 2010				
Day1	25-33	21-24	0 to -4	Surface trough oriented N-S
Day2	28-33	19-23	-2 to -4	Approaching cold front from NW
Jun 8-9, 2009				
Day1	27-29	17-20	0 to -2	Stationary front oriented E-W
Day2	27-31	19-21	-2 to -6	Squall line oriented N-S
May 24, 2009				
Day1	22-30	15-18	0 to -4	Approaching cold front from NW
Jun 3-4, 2008				
Day1	23-29	12-16	2 to -2	Approaching cold/stationary front from NW
Day2	27-29	18-21	0 to -5	Warm front oriented E-W
Aug 25-56, 2007				
Day1	29-37	21-24	-2 to -8	No surface fronts
Day2	30-38	20-25	0 to -4	Cold front oriented NE-SW
July 5-6, 2005				
Day1	30-33	19-22	0 to -3	Approaching cold front from W
Day2	29-33	20-23	0 to -2	Stationary front oriented N-S

**Lifted Index is defined as the difference in environmental temperature and parcel temperature at 500hPa. Negative values suggest the presence of CAPE.*

2.2.2 Design of model simulations

The control experiment consists of nested runs using the Weather Research and Forecast (WRF) model (Skamarock et al. 2008) at three different resolutions, viz., coarse (37.5 km), medium (7.5 km), and fine (2.5 km). The domain and the one-way nesting configuration of the model are shown in Figure 2.1.

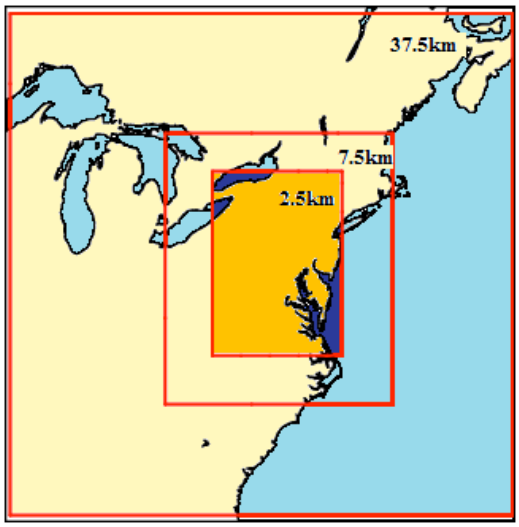

Figure 2.1 Model experimental domain (dark shaded) over the Chesapeake Bay watershed, shown along with the three-grid one-way nesting configuration that is used. The outermost grid resolution is 37.5 km, the middle grid is 7.5 km and the innermost grid resolution is 2.5 km.

The cumulus parameterization scheme is activated for the coarse and the medium resolution nested grids only, whereas the fine grid resolves convection explicitly. The model output from all three resolutions is evaluated over the dark shaded region (shown in Fig. 2.1). This enables examination of the sensitivity of model results not only to horizontal resolution but also to the treatment of cumulus physics. The control experiment is carried out using the Betts-Miller-Janjić (BMJ) cumulus parameterization scheme and the Yonsei University (YSU) boundary layer scheme (Hong et al. 2006). The BMJ scheme uses a convective adjustment method, and may

activate deep convection only if the cloud-depth exceeds 200 hPa. Although it doesn't explicitly consider parcel buoyancy in its trigger function, it includes an implicit constraint for cloud-layer CIN based on enthalpy conservation (Baldwin et al. 2002).

The model has 30 vertical levels in the terrain-following sigma coordinate system, eight within the lowest 1 km and the remaining spaced equally up to 100 hPa. The unified Noah Land Surface Model (Chen and Dudhia 2001) predicts heat and moisture fluxes at the surface while the WRF Single-Moment 5-class (WSM5) scheme (Hong et al. 2004; Hong and Lim 2006) is chosen for parameterizing microphysics. Two sets of sensitivity experiments are carried out, first by replacing the YSU with Mellor-Yamada-Janjić (MYJ) boundary layer scheme (Mellor and Yamada 1982), and the second by replacing the BMJ with the Kain-Fritsch (KF) cumulus parameterization scheme.

The 00 UTC forecast cycle from the Global Forecast System (GFS) model is used for initial and boundary conditions. In the past, studies involving long-term climate modeling experiments have reported the problem of premature convection. One reason for using the GFS model to drive WRF is to investigate whether similar timing errors also exist in "forecast" mode (i.e., when no data assimilation is active). For each event, the forecast is run up to 180 hours (seven and a half days) and a lead time of 12 hours is allowed for model spin-up. The effect of increasing lead time on the model results is also explored. In addition to the control run, 4 more ensemble runs are created by perturbing initial temperature and moisture values within the lower atmospheric levels (from the surface up to the lowest six sigma levels). It is expected that surface-based convection will be most sensitive to perturbations at these levels.

The perturbations are computed using a random normal distribution function with mean = 0, and standard deviation = 1.8 °K (for temperature) and 10% (for relative humidity). It is ensured that points of supersaturation are not produced.

2.2.3 Validation against observations

The 4.7 km resolution Stage IV precipitation dataset from the National Centers for Environmental Prediction's Environmental Modeling Center (NCEP's EMC) (Baldwin and Mitchell 1996; Lin and Mitchell 2005) is used as observational reference primarily to verify the modeled diurnal cycle of precipitation during each event. In addition, rainfall observations are used to compute the frequency bias score (referred to hereafter as BIAS in uppercase) at various precipitation thresholds, which serves as a measure of the precipitation intensity produced by the model. BIAS is calculated using the Development Testbed Center's Model Evaluation Tool (MET version 2.0) verification package (2009).

Satellite-derived soundings from the Atmospheric Infrared Sounder (AIRS) instrument onboard the National Aeronautics and Space Administration's (NASA's) Aqua Spacecraft is used to investigate relevant trigger processes. The AIRS Level 1B infrared, geolocated, and calibrated radiances product is used. Since atmospheric soundings from ground-based sources (radiosondes, aircraft profiles, etc.) are not available at sufficient spatiotemporal frequency, the high spatial resolution AIRS dataset is employed. Each AIRS satellite granule consists of 90 × 135 grid points at 13.5 km spatial resolution (at nadir) and a swath width of around 1650 km. Satellite pass occurs over the Chesapeake Bay watershed in the afternoon (between 1300–1500 LST), which is around the time of precipitation onset. Profiles of temperature and

moisture are obtained over locations with observed rainfall recorded soon after the satellite pass. This provides a snapshot of the real atmosphere just prior to the initiation of convection.

2.2.4 AIRS satellite retrievals

The AIRS instrument contains 2348 channels, thus providing atmospheric profiles with impressive vertical resolution. Hyperspectral soundings of temperature and moisture are obtained at 101 levels using separate clear-sky (Weisz et al. 2007a) and cloudy (Weisz et al. 2007b) regression retrieval algorithms. The AIRS retrievals tend to have a slightly cool and dry bias. However, the algorithm is known to produce reasonably good results for optically thin cloud conditions (Weisz et al. 2007b). Thus, in order to filter out grid points with thick clouds, cloud-thickness values using the University of Wisconsin's AIRS regression retrieval algorithm package are obtained (UWAIRS version 3.0; Smith et al. 2012). This algorithm uses a dual regression technique that determines the presence of a cloud and associated cloud-thickness value based on the differences between clear-trained and cloudy-trained solutions at each grid point (Smith et al. 2012). The assigned cloud-thickness values may range from 0-3 with 0 indicating clear or thin cloud conditions and 3 representing locations with thick clouds (Smith et al. 2012). In this study, only grid points with 0 cloud-thickness, are considered. After applying this filter, the cloudy and clear-sky regression algorithms produce soundings that are fairly realistic. Comparison with radiosonde observations obtained from the National Climatic Data Center's Integrated Global Radiosonde Archive (IGRA) yields good agreement, thus confirming that the cloud-filtered AIRS data is able to accurately represent the thermodynamic properties of the

atmosphere. As an example, a comparison of cloudy and clear-sky soundings against co-located radiosonde measurements is shown in Figures 2.2 (a) and 2.2 (b), respectively. The soundings are recorded during a warm season convective event that occurred over South Africa on November 28, 2006. The locations correspond to the World Meteorological Organization (WMO) stations in Pretoria (Fig. 2.2 (a)) and De Aar (Fig. 2.2 (b)). The satellite pass occurs at around 1135 UTC over this region,

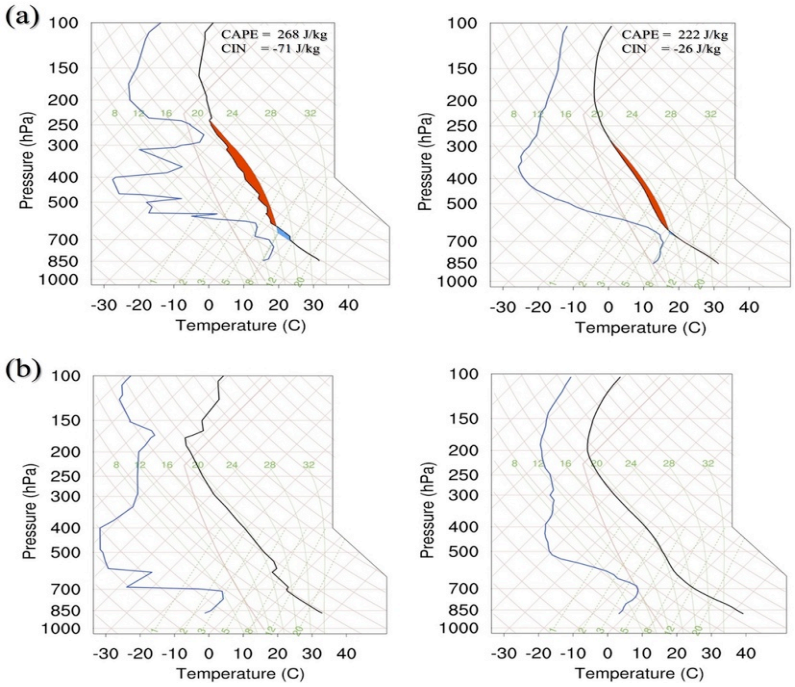

Figure 2.2 Comparison of co-located skew T-log P soundings obtained from radiosonde (IGRA) measurements at 1000 UTC (left panels), and AIRS satellite data at 1135 UTC (right panels) using (a) cloudy regression retrieval algorithm over Pretoria and (b) clear-sky regression retrieval algorithm over De Aar. CAPE and CIN areas are represented by red and blue shadings, respectively. The soundings are recorded on November 28, 2006 during a warm season convective event that occurred over South Africa.

which approximately coincides with the timing of the daily radiosonde measurements (1000 UTC). AIRS is able to successfully capture the observed spatial variability in the vertical structure of the atmosphere. The presence of instability and a well-

developed boundary layer with low CIN values, is accurately reproduced over Pretoria. On the other hand, the absence of CAPE in the sounding over De Aar, is also correctly indicated by the AIRS data. This gives us confidence that the high spatial information contained in the AIRS dataset is usable to study location-specific soundings over grid points with observed rainfall.

2.2.5 Convective and pre-convective soundings

The regression retrieval is performed over grid points that have precipitation beginning at a time closest to, but soon after the satellite pass (1400-1600 LST). These atmospheric profiles represent the soundings of the convective atmosphere, since they are observed right before precipitation occurs. Similarly, profiles are also retrieved over grid points with rainfall beginning two hours after satellite pass (1600-1800 LST). These time-lagged profiles may be referred to as soundings of the pre-convective atmosphere. The observed differences between convective and pre-convective soundings may help infer the processes that are relevant to the triggering of surface-based convection.

The step-wise procedure to obtain these representative skew T-log P soundings is described below.

1.) Using Stage IV gridded precipitation, locations with observed rainfall beginning within the hour or next of satellite pass (i.e., 1400-1600 LST) are identified. Latitude and longitude values of these locations are obtained.
2.) This information is used to co-locate corresponding location indices within the AIRS satellite granule.

3.) Retrievals of temperature and moisture profiles are obtained at these locations using the regression algorithms, and skew T-log P soundings representative of the convective atmosphere are generated. (Points with cloud contaminated retrievals or non-positive surface CAPE are disregarded).

4.) The above steps are repeated for locations with observed precipitation beginning approximately two hours after satellite pass (1600-1800 LST). The soundings from these grid points are used as a proxy to represent the pre-convective atmosphere.

As an example, Figure 2.3 (a) shows the satellite-derived skin temperature over the region of interest retrieved using the clear-sky regression algorithm, on August 5, 2010 (1447 LST). The point marked with a black '•' symbol indicates a location with

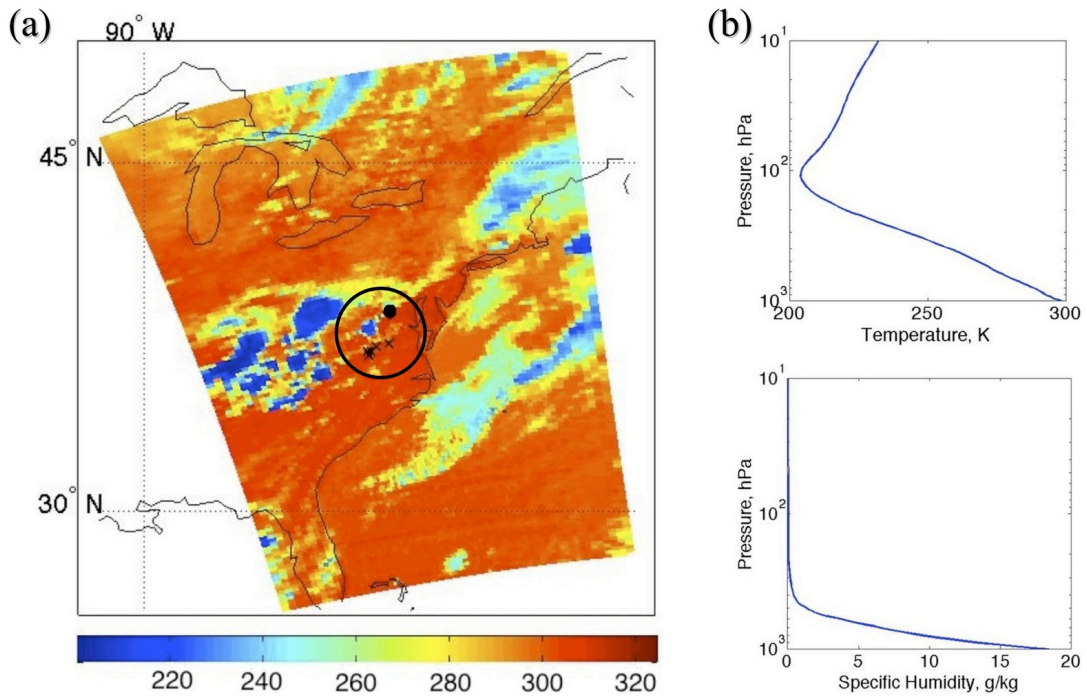

Figure 2.3 (a) Satellite-derived skin temperature (°K) on August 5, 2010 at 1447 LST, along with locations used for retrieving atmospheric soundings representing the convective atmosphere (grid point marked with '•' symbol) and pre-convective atmosphere (grid points marked with '**x**' symbol); and (b) is the temperature (top) and moisture (bottom) profiles obtained at the grid point marked with '•' symbol.

precipitation beginning between 1400-1500 LST, that is used to obtain temperature and moisture profiles representative of the convective atmosphere (see Fig. 2.3 (b)). Similarly, grid points with precipitation beginning between 1600-1700 LST are marked with black '**x**' symbols in Figure 2.3 (a). These are subsequently used to retrieve soundings of the pre-convective atmosphere. Note that retrievals at the hour closest to observed rainfall are not as abundantly available due to contamination by clouds.

2.3 Results

2.3.1 Early bias in parameterized convection

Figure 2.4 compares the temporal evolution of the domain-averaged ensemble mean precipitation at each resolution with observations. It can be seen that the onset and peak of convection often occurs too early in the parameterized grids (left panels of Fig. 2.4 (a)-(f)). Moreover, the sensitivity to model resolution remains low when convection is parameterized. Explicit convection does not always improve the mean precipitation but it appears to rectify the early bias and thereby improving the temporal evolution of rainfall (companion panels of Fig. 2.4 (a)-(f)). Note that such an improvement in the model diurnal cycle with explicit convection is clearly evident at lead times shorter than 72 hours. For longer lead times, it appears that the forecast errors are driven primarily due to sensitivity to initial and boundary conditions, causing the model solution to be less divergent between parameterized and explicit grids (not shown). Thus, Fig. 2.4 suggests that the problem of early convection in

parameterization schemes, reported extensively in climate-modeling literature, may also appear in short-range deterministic forecasts.

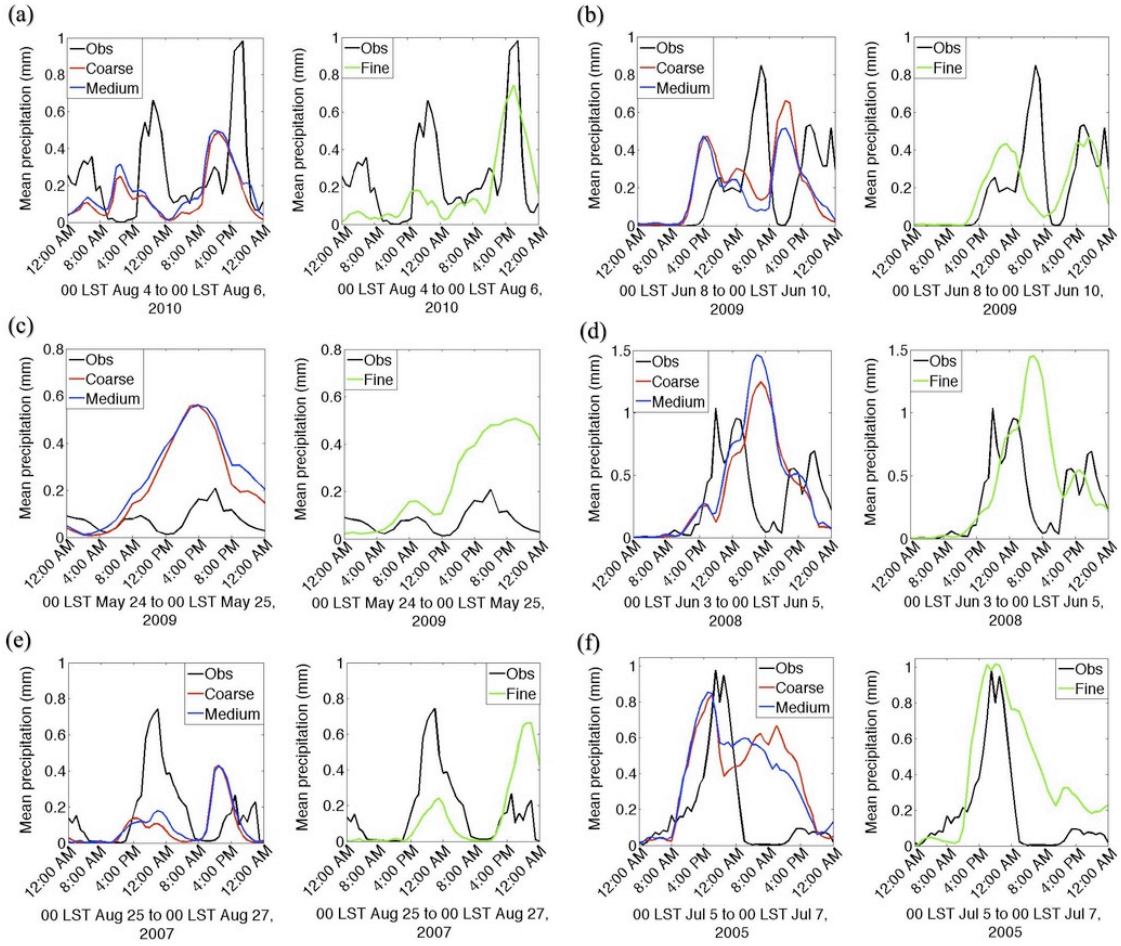

Figure 2.4 Temporal evolution of ensemble mean precipitation forecasts for coarse (red), medium (blue) and fine (green) resolutions against observations (black), respectively, on (a) August 4-5, 2010, (b) June 8-9, 2009, (c) May 24, 2009, (d) June 3-4, 2008, (e) August 25-26, 2007 and (f) July 5-6, 2005.

In order to quantify the improvement with explicit convection, especially in the temporal evolution of model forecast, the diurnal cycle of precipitation (shown in Fig. 2.4) is first normalized with respect to the daily mean for each ensemble member. The time-derivative is then computed at hourly intervals. The mean squared error (MSE) is

calculated by subtracting the temporal change in the observed precipitation ($\Delta O/\Delta t$) from that in the precipitation forecast ($\Delta F/\Delta t$) at each resolution using the following equation:

$$MSE = 1/n \sum \left(\frac{\Delta F}{\Delta t} - \frac{\Delta O}{\Delta t} \right)^2 . \quad (2.1)$$

In Eq. 2.1, n is the number of hourly samples, and the summation is performed over the entire convective period for each event. The MSE values calculated from Eq. 2.1 for various ensemble members, appear to be normally distributed as indicated by the Shapiro-Wilks test (*significance level = 0.05*). Table 2.2 compares the ensemble-averaged MSE between parameterized and explicit grids.

Table 2.2 Comparison of ensemble-averaged mean squared error (MSE) of the time-evolution of normalized mean precipitation between paramaterized and explicit grids.

Event	Model Resolution (km)	Ensemble-averaged MSE in time-evolution of normalized mean precipitation	t-value for the improvement in MSE calculated for explicit grid	Significance level ($p \leq 0.05$)	Sample size (No. of ensemble members)
Aug 4-5, 2010	37.5	0.4851	2.3797	0.05	5
	7.5	0.5260	6.0536	0.005	5
	2.5	0.3860			5
Jun 8-9, 2009	37.5	0.4447	10.8269	0.001	5
	7.5	0.4467	6.0802	0.005	5
	2.5	0.2962			5
May 24, 2009	37.5	0.2287	2.6173	0.05	5
	7.5	0.2163	1.5896	-	5
	2.5	0.2001			5
Jun 3-4, 2008	37.5	0.2911	0.9124	-	5
	7.5	0.2981	2.9894	0.05	5
	2.5	0.2798			5
Aug 25-26, 2007	37.5	0.5774	12.7879	0.001	5
	7.5	0.4486	18.7217	0.0005	5
	2.5	0.2603			5
Jul 5-6, 2005	37.5	0.2370	4.3118	0.025	5
	7.5	0.2298	9.6471	0.005	5
	2.5	0.1943			5

The MSE is lower when explicit convection is used. The results from a matched pairs t-test indicate that explicit convection indeed leads to a statistically significant improvement in the MSE values, for most cases. Thus, the premature triggering of convection is most likely due to deficiencies in the cumulus parameterization scheme. As a supplementary test, the model output from the medium resolution grid (7.5 km) is compared with a simulation carried out by turning off the cumulus scheme. For horizontal resolutions between 4 and 10 km, the use of a cumulus scheme is often regarded contentious. In this study, it is observed that an improvement with explicit convection may occur even at 7.5 km resolution, although this may be case-dependent. The following subsection compares the representation of thermodynamic parameters (CAPE and CIN) at the time of convective initiation in the parameterized and explicit grids.

2.3.2 Diurnal Cycle of CAPE and CIN

Baldwin et al. (2002) identified certain characteristic features produced by the BMJ scheme's shallow convective mechanism that may erroneously eliminate the capping inversion or CIN, which is crucial in suppressing surface-based deep convection. The scheme's shallow convection does not include any constraints on negative buoyancy, and is easily triggered as long as there is instability (CAPE) in the atmosphere. It causes warming and drying near the cloud-base but cooling and moistening near the cloud-top. This mixing process consequently removes stable layers or negative buoyancy (Baldwin et al. 2002). In order to inspect whether this is responsible for the early onset of convective rainfall, the diurnal cycles of CAPE and CIN are compared between parameterized and explicit grids (Fig. 2.5). While there is

no major difference in the phase, some amplitude differences do exist. The CIN, however, is higher during the initiation of parameterized convective rainfall suggesting that there is no significant contribution to premature precipitation by BMJ scheme's

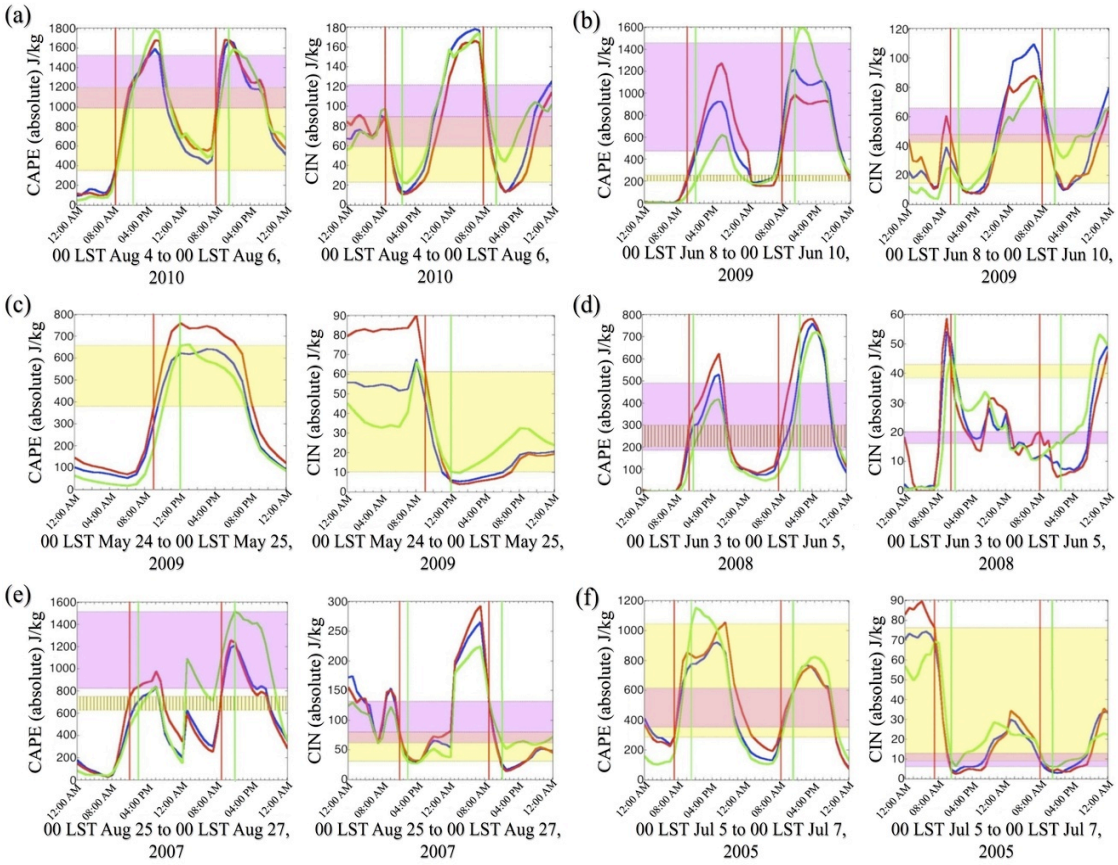

Figure 2.5 Temporal evolution of ensemble mean absolute CAPE (positive buoyancy) and absolute CIN (negative buoyancy) averaged over grid points with precipitation for coarse (red), medium (blue) and fine (green) resolutions on (a) August 4-5, 2010, (b) June 8-9, 2009, (c) May 24, 2009, (d) June 3-4, 2008, (e) August 25-26, 2007 and (f) July 5-6, 2005, respectively. The colored vertical lines represent the timing of onset of deep convection within the coarse (red) grid with parameterized convection and fine (green) grid with explicit convection. The yellow and magenta shading represent buoyancy differences between coarse and fine grids observed during convective initiation on the first and second days of the events, respectively. Differences in positive buoyancy are calculated by subtracting the absolute mean CAPE values of coarse grid from that of fine grid ($|CAPE_{fine}| > |CAPE_{coarse}|$). Differences in negative buoyancy are calculated by subtracting the absolute mean CIN values of fine grid from that of coarse grid ($|CIN_{coarse}| > |CIN_{fine}|$). Negative differences are hatched.

shallow convection. In fact, the relatively high CIN values at the time of rainfall onset indicate that the deep convective trigger function is unable to recognize the presence of a moderate to strong capping layer during morning hours. The convective adjustment method in the scheme only produces precipitation if there is a net warming and drying within the cloud, thus automatically imposing an implicit trigger constraint on negative buoyancy (CIN) (Baldwin et al. 2002). Baldwin et al. (2002) posit that in the presence of strong CIN or a stable inversion layer above the LCL, the adjustment process will entail extensive cooling and moistening thereby failing to initiate deep convection. It appears that such an implicit trigger may not always be sufficient to suppress convection. This is further investigated using model soundings in section 2.3.6. Figure 2.5 also shows that, for most cases, the instability (CAPE) is weaker when parameterized convection begins compared to the values at the start of explicit convection. This, in turn, may negatively influence the rainfall intensity produced by the scheme. In order to investigate such a possibility, the frequency bias at various precipitation thresholds is compared between the parameterized and explicit grids.

2.3.3 Comparison of Frequency Bias

Observations and model output are first transformed using the budget interpolation or remapping method (described in Accadia et al. 2003) onto NCEP's grid 227 (5 km resolution). It is checked to ensure that differences in the maximum and mean precipitation introduced due to this interpolation are not significant for model output at any resolution. The BIAS is defined based on the elements of the contingency table computed for 24-hr accumulated precipitation over the interpolated

grid. It is the ratio of the total number of forecasts to the total number of observations given by the following equation,

$$BIAS = \frac{a+b}{a+c}. \tag{2.2}$$

The quantities *a*, *b* and *c* represent the total number of hits, false alarms and misses, respectively. A ratio below (above) 1, implies that the precipitation at that threshold is underestimated (overestimated) by the model. If the BIAS steadily decreases below the value of 1 (or drops to 0) with increasing precipitation thresholds, then the model may have a low-intensity bias. Likewise, a steadily increasing BIAS ratio (greater than 1) signifies a high-intensity bias in simulated precipitation. The MET software computes sampling uncertainty of the BIAS using the bootstrap resampling method (Diaconis and Efron 1983) wherein the data are resampled 1000 times in order to calculate an uncertainty range for the true frequency bias value at a significance level of 0.05. Figure 2.6 compares the ensemble mean BIAS between the three resolutions at various precipitation thresholds, for rain days that have significant differences against the sampling uncertainty. It can be seen that the parameterized grids tend to underestimate rainfall at higher thresholds (>10 mm), suggesting that the precipitation predicted by the BMJ scheme does have a low-intensity bias (see Fig. 2.6 (b), (d), (f), (h)). The forecast of high rainfall amounts is sometimes improved at the medium (7.5 km) resolution (Fig. 2.6 (e), (g)) on days when the BMJ scheme is found to be less active (i.e., when the convective to total precipitation ratio is low). Explicit convection may significantly improve the low BIAS ratios at higher thresholds, although it tends to introduce a high-intensity bias in most cases (Fig. 2.6 (b), (d), (h), (i)). Figures 2.5 and 2.6 suggest that the lower CAPE values observed during premature parameterized

convection may be responsible for the low-intensity bias. However, it should be noted that such an effect can easily be masked by factors such as the cloud-layer moisture, which is known to have a profound influence on the BMJ scheme's convective adjustment process and the subsequent precipitation intensity produced by it.

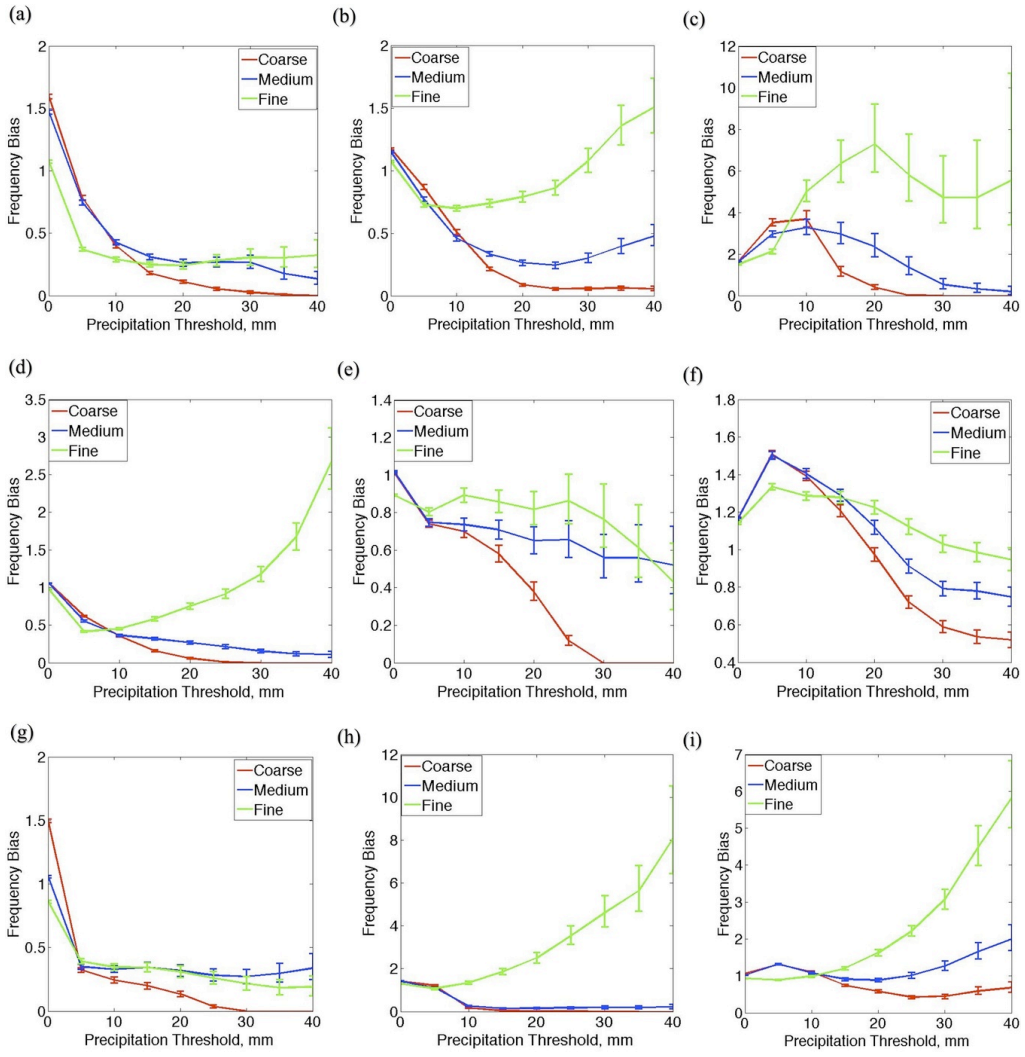

Figure 2.6 The ensemble mean frequency bias and sampling uncertainty for 24-hr accumulated rainfall at various precipitation thresholds for coarse (red), medium (blue), and fine (green) resolutions on (a) August 4, 2010, (b) August 5, 2010, (c) June 8, 2009, (d) June 9, 2009, (e) June 3, 2008, (f) June 4, 2008, (g) August 25, 2007, (h) August 26, 2007 and (i) July 5, 2005, respectively.

In the following subsection, the results from the sensitivity experiments are discussed. These experiments primarily test the influence of boundary layer and cumulus physics on the timing bias observed in parameterized convection.

2.3.4 Sensitivity of parameterized convection to boundary layer and cumulus physics

While it appears that the premature convection (shown in Fig. 2.4) is the result of deficiencies in the cumulus scheme, it may also be influenced by errors in the simulated boundary layer and its interaction with convective parameterization. In order to investigate this, results from the sensitivity experiment using the MYJ boundary layer scheme are compared with output from the control run for parameterized grids. The temporal evolution of the mean precipitation from the control (red) and sensitivity (blue) runs shows very little divergence for the coarse grid (see left panel of Fig. 2.7 (a)-(f)). The model solution is more sensitive to cumulus physics as indicated by the results from the second set of sensitivity experiments performed using the KF cumulus parameterization scheme (see right panel of Fig. 2.7 (a)-(f)). Similar results are also obtained for medium resolution (7.5 km). The early bias in the onset and peak of parameterized convection, however, persists when the KF scheme is used. This warrants an investigation of the KF scheme's trigger function in addition to that of the BMJ scheme. In subsection 2.3.6, co-located model soundings within the parameterized and explicit grids are compared and plausible reasons for the premature onset of parameterized convection in both schemes are discussed. It is, however, useful to first inspect the characteristics of observed atmospheric soundings obtained prior to the start of convection.

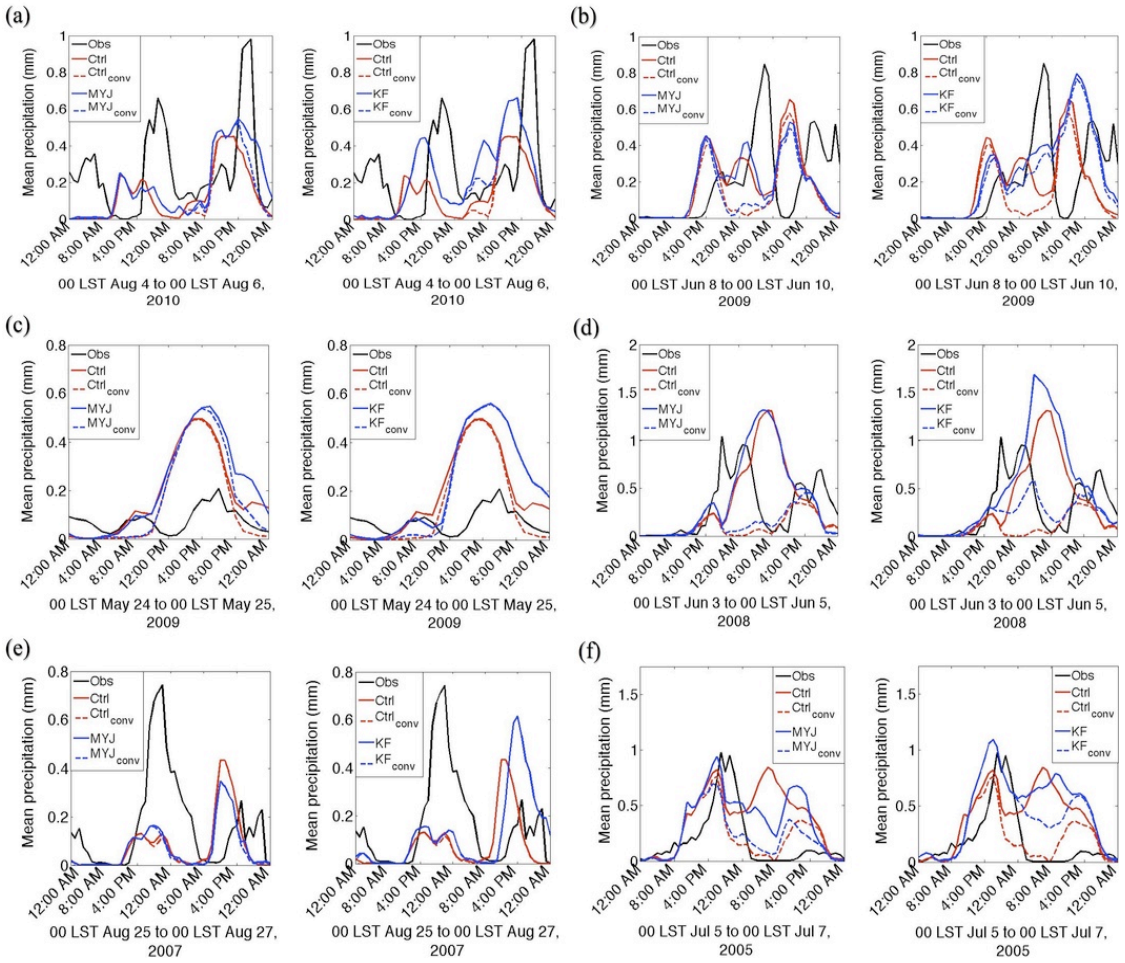

Figure 2.7 Mean precipitation forecast at coarse (37.5 km) resolution from control run (red) and sensitivity run (blue) against observations (black) on (a) August 4-5, 2010, (b) June 8-9, 2009, (c) May 24, 2009, (d) June 3-4, 2008, (e) August 25-26, 2007, and (f) July 5-6, 2005, respectively. For each subfigure, the sensitivity run using MYJ boundary layer scheme is shown in the left panel, and the sensitivity run using KF cumulus parameterization scheme is shown in the right panel. The dotted lines represent the convective component of mean precipitation produced by control run (red) and sensitivity run (blue).

2.3.5 Satellite-derived soundings

Convective soundings are obtained at grid points with rainfall recorded at the hour closest to satellite pass. As a result, cloud contamination becomes a significant problem. For most cases, only a single representative clear-sky or (thin) cloudy retrieval sounding is obtained. No data are available for Aug 4, 2010, May 24, 2009,

Jun 3-4, 2008 and Jul 6, 2005. As discussed in section 2.2.5, the pre-convective soundings are obtained at locations with delayed rainfall. The top (clear-sky) and bottom (cloudy) panels of Figures 2.8 (a) and 2.8 (b), compare the pre-convective and convective soundings obtained on Aug 5, 2010 and Aug 25, 2007, respectively. (Note that in all skew T- log P soundings hereafter, red and blue shadings represent CAPE and CIN areas, respectively).

The convection occurs ahead of an approaching cold front from the west during the first case (Aug 05, 2010), while there are no mesoscale boundaries in the vicinity of rainfall during the second event (Aug 25, 2007) (see Table 2.1). Near-saturated relative humidity values at the surface and a well-developed boundary layer are observed in the convective soundings indicating that the atmosphere was thermodynamically primed for surface-based convection. High surface relative humidity may also be evident in some of the pre-convective soundings (top left panels of Fig. 2.8 (a), (b)). In these soundings, however, there appears to be CIN between the LCL and LFC that has not yet been overcome by processes such as boundary layer growth. The low-level (surface to 850 hPa) structural differences between the convective and pre-convective soundings (right panel of Fig. 2.8) suggest that the development of an unstable lapse rate is most crucial for the removal of CIN. Differences in the clear-sky retrievals (top right panels of Fig. 2.8 (a), (b)) show a decrease in specific humidity at the surface but an increase near the top of the boundary layer. This is suggestive of mixing processes that transport moisture from the surface to upper levels. Additionally, differences in cloudy retrievals (bottom right

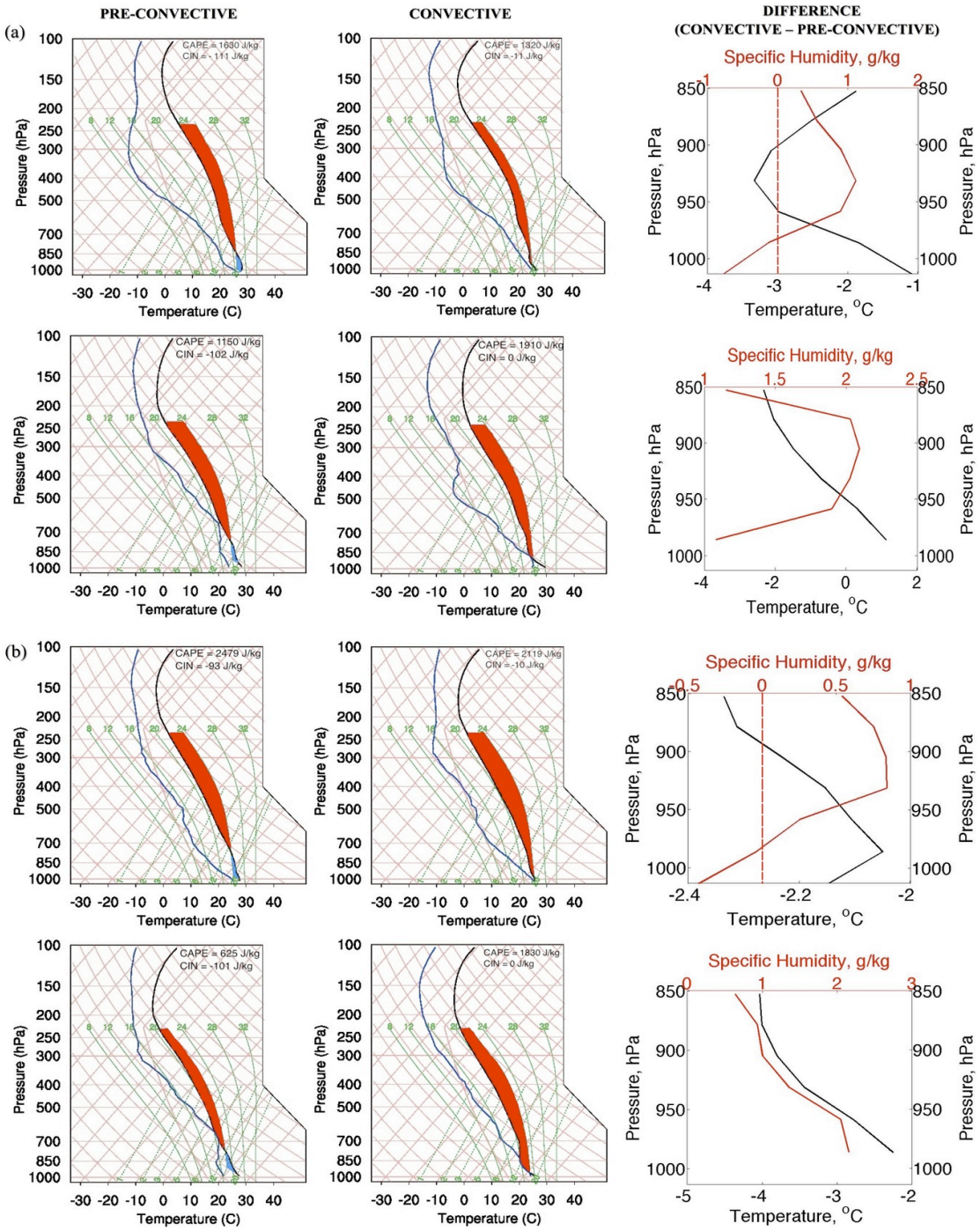

Figure 2.8 Representative skew T-log P soundings of observed pre-convective atmosphere (left panel), convective atmosphere (center panel) and their differences (right panel) obtained using the clear-sky retrieval algorithm (top) and the cloudy retrieval algorithm (bottom) for the cases of observed convection on (a) Aug 5, 2010, and (b) Aug 25, 2007. Satellite pass occurred at 1447 LST on Aug 5, 2010 and at 1441 LST on Aug 25, 2010. Soundings of convective and pre-convective atmosphere correspond to locations with precipitation beginning between 1400-1500 LST and 1600-1700 LST, respectively (see Appendix for location indices).

panels of Fig. 2.8 (a), (b)) show an increase in the boundary layer specific humidity indicating that low-level moistening may occur prior to convection. Note that a substantial growth in CAPE due to large-scale destabilization (such as boundary layer moistening) is only observed for one of the cases (compare bottom left and center panels of Fig. 2.8 (b)). This suggests that statistical equilibrium, which requires convection to be produced based on the rate of generation of instability (CAPE), is not a necessary condition for surface-based convection in this region. The removal of CIN, or the assumption of non-equilibrium convection, appears to be valid.

In fact, the most consistent feature distinguishing convective from pre-convective soundings is the lack of negative buoyancy, mainly due to differences in the low-level lapse rate. A stable layer, as often observed in the pre-convective soundings, may easily delay the onset of convection. Such a layer of negative buoyancy is conspicuously absent in all soundings of the convective atmosphere. This confirms that the buoyancy below the LFC is an important trigger constraint for surface-based or boundary layer convection.

2.3.6 Representation of negative buoyancy in model soundings

Model soundings at grid points with early parameterized convection are compared against co-located soundings from the explicit grid at the time of convective initiation. (Only grid points with convective to total precipitation ratio in excess of 0.9 are selected). At the hour of early rainfall, it is evident that the layer of negative buoyancy above the LCL inhibits explicit convection but fails to suppress the occurrence of parameterized convection. The left and center panels of Fig. 2.9 show examples of model soundings from co-located grid points in the coarse (37.5 km) and

fine (2.5 km) grids, respectively, obtained at the time of premature convective rainfall by the BMJ scheme. There is negative buoyancy between the LCL and LFC at this

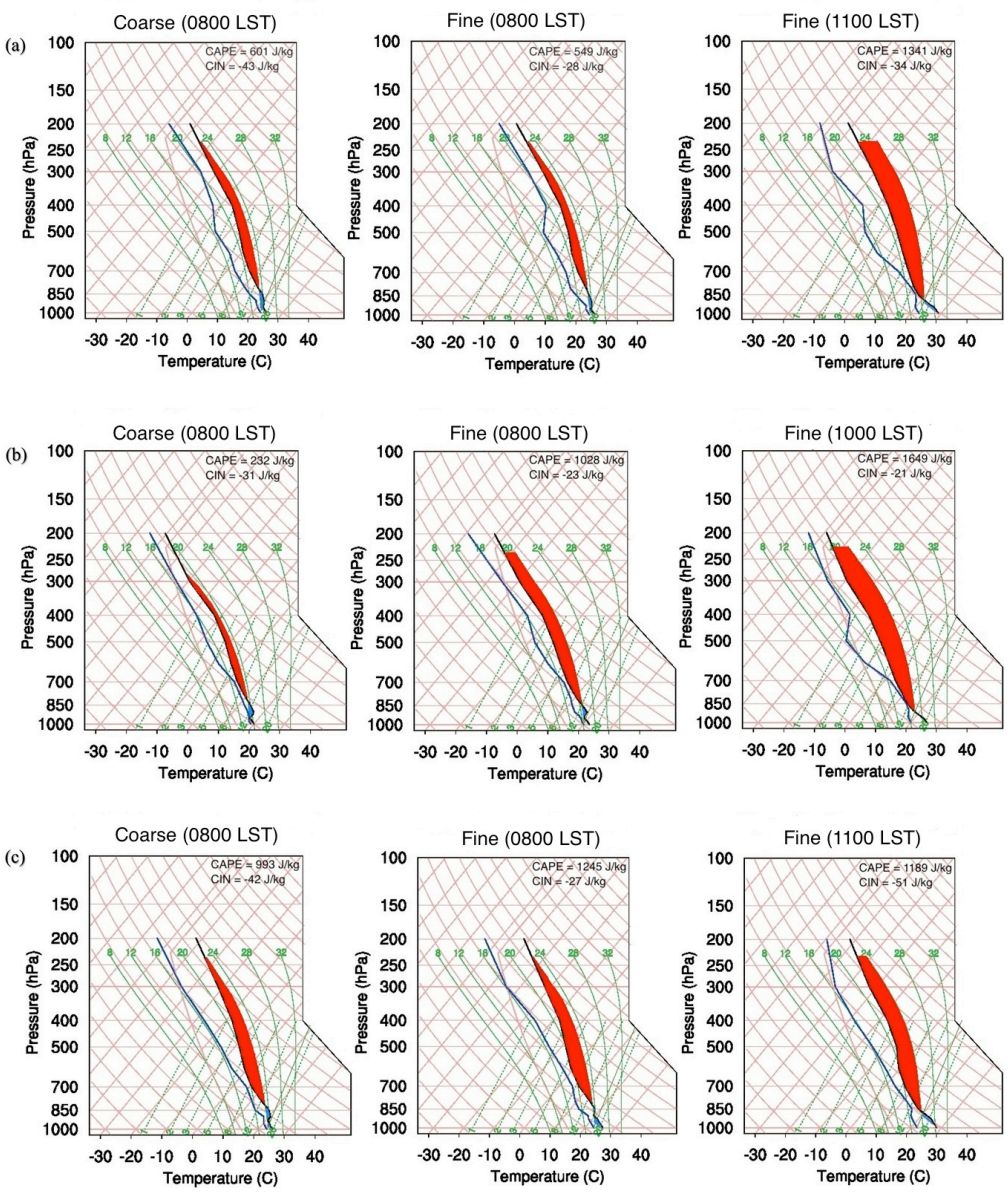

Figure 2.9 Representative skew T-log P soundings obtained over co-located grid points in the coarse (left) and fine (center) grids at the hour of initiation of parameterized deep convection, and at the hour of initiation of explicit convection in the fine grid (right) for (a) August 5, 2010; (b) Jun 9, 2009 and (c) July 5, 2005, respectively. Parameterized convection begins at 0800 LST for soundings in (a), (b), (c). Explicit convection begins at 1100 LST for soundings in (a) and (c), and at 1000 LST for sounding in (b). The soundings in this figure are obtained from the control run using BMJ scheme (see Appendix for location indices).

time, but the implicit constraint on CIN imposed by the scheme is clearly insufficient to suppress deep convection. Explicit convection begins later during the day only after the convective boundary layer and the instability are well developed (right panel of Fig. 2.9).

The maximum rainfall predicted over grid points corresponding to the soundings shown in Figs. 2.9 (a), (b) and (c), are 1.9, 3.5 and 2.4 mm, respectively, with parameterized convection, and 4.5, 27.3 and 7.1 mm, respectively, with explicit convection. The left panels of Figure 2.9 (a)-(c) suggest that although there is deep cloud-layer moisture, which is a recipe for intense precipitation in the BMJ scheme, the lower CAPE values at this hour may contribute to the low-intensity bias. Comparison of left and right panels of Fig. 2.9 (c) show that higher CAPE values develop at a subsequent hour without significant changes to the relative humidity in the cloud. Thus, by delaying convection and allowing the growth of the instability, it may be possible to rectify the scheme's low-intensity bias to some extent.

Similar to Fig. 2.9, the left and center panels of Fig. 2.10 (a)-(b) show examples of co-located soundings obtained from the sensitivity run (using the KF scheme), at the time of the onset of parameterized convective rainfall. Once again, there is negative buoyancy below the LFC. This layer of CIN does not suppress parameterized deep convection, but successfully delays explicit convection which begins only after the CIN is overcome (right panels of Fig. 2.10 (a), (b)). The trigger for moist convection in the KF scheme, unlike the BMJ scheme, explicitly accounts for CIN by using a parcel buoyancy equation, but applying it only at the LCL (cloud-base). The scheme first forms a well-mixed updraft source layer (USL) starting from

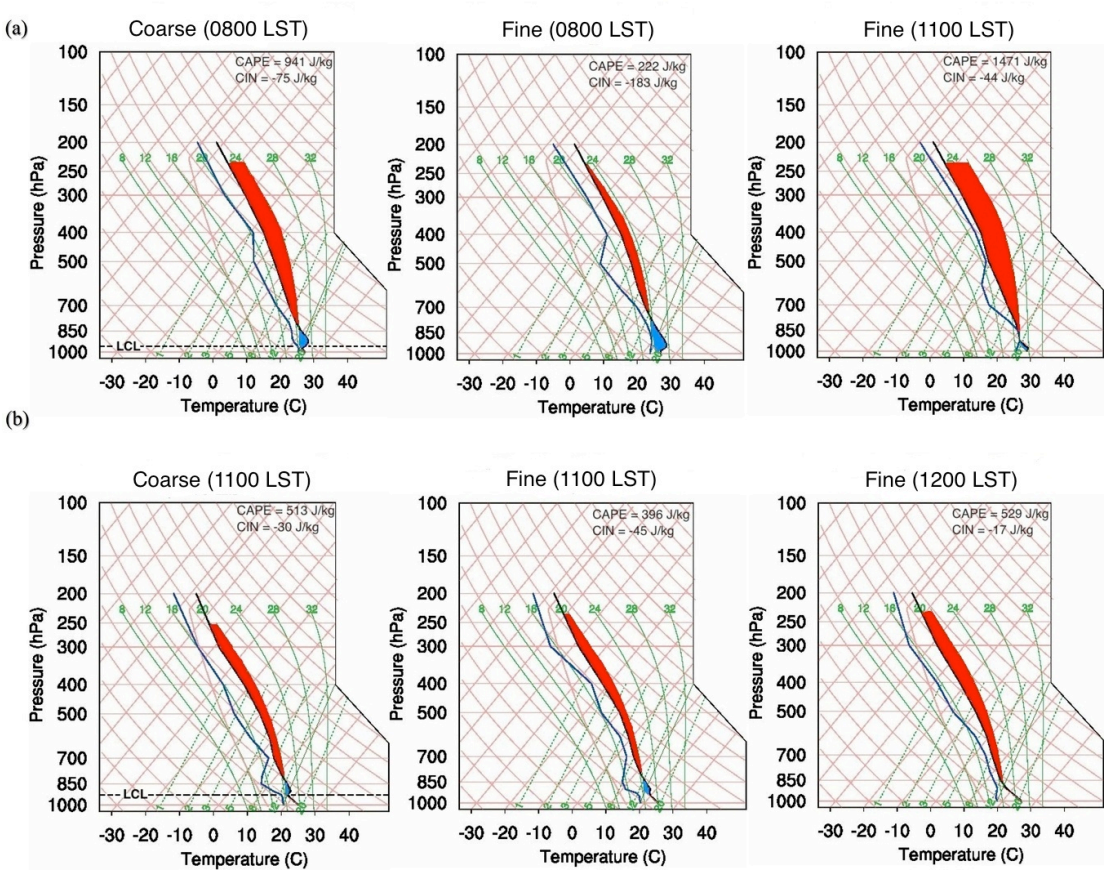

Figure 2.10 Representative skew T-log P soundings obtained over co-located grid points in the coarse (left) and fine (center) grids at the hour of initiation of parameterized deep convection, and at the hour of initiation of explicit convection in the fine grid (right) for (a) August 5, 2010 and (b) Jun 8, 2009, respectively. Parameterized convection begins at 0800 LST for sounding in (a) and 1100 LST for sounding in (b), whereas explicit convection begins at 1100 LST for sounding in (a) and at 1200 LST for sounding in (b), respectively. The soundings in this figure are obtained from the sensitivity run using KF scheme (see Appendix for location indices).

the lowest model level up to a layer-depth of at least 60 hPa (Kain 2004). The USL is raised to its LCL at which point a perturbation temperature (δT), proportional to the grid-resolved vertical velocity at that level (w_g) is assigned to it (see Eq. 2.3; Kain 2004). The term c_z refers to a threshold vertical velocity in cm s^{-1}, which is proportional to the height of the LCL, and k is a unit number with dimensions °K $s^{1/3}$

$cm^{-1/3}$. For details on calculation of c_z, refer to Kain (2004). The perturbation temperature is computed as;

$$\delta T = k[w_g - c_z]^{1/3}. \quad (2.3)$$

Moist convection, or the formation of convective updrafts is allowed if the sum of the parcel temperature and δT, exceeds the environmental temperature at the LCL (Kain 2004). This means that even for a slightly positive large-scale vertical velocity (the order of a few centimeters per second), a marginally stable parcel at its cloud-base can become a convective updraft. Note that theoretically, moist convection may occur only when the parcel is able to reach its LFC, not LCL. The constraint described above appears to be satisfied for the case of the soundings shown in Fig. 2.10 (left panels), since the parcel is nearly neutral at the LCL and a small perturbation may easily make it positively buoyant. This, in fact, is true for both soundings. The vertical velocity (w_g) computed at the cloud-base is found to be small but positive, viz., 1.24 and 2.5 cm s^{-1}, respectively. The resulting temperature perturbation calculated from Eq. 2.3 will then be around 1 and 1.25 °K, respectively, which is sufficient to satisfy the buoyancy criteria at the cloud-base. After the decision to activate moist (shallow/deep) convection is made, the USL (now updraft) is released with its original unperturbed temperature and moisture at the LCL, and with a vertical velocity given by Eq. 2.4 (Kain 2004). The terms Z_{LCL} and Z_{USL} refer to the heights of the LCL and base of the USL, respectively, while T_{ENV} refers to the temperature of the environment at LCL;

$$w_{p0} = 1+1.1[(Z_{LCL}-Z_{USL})* \delta T/T_{ENV}]^{1/2}. \quad (2.4)$$

According to Kain (2004), the above formula yields starting velocities up to several meters per second. Thus, a marginally buoyant parcel at the LCL, is now a full-fledged convective updraft with a significantly positive vertical velocity. For the soundings shown in Fig. 2.10 (a), (b), Eq. 2.4 approximately yields vertical velocities (w_{p0}) of 2 and 2.4 m s^{-1}, respectively, which are two orders of magnitude greater than the original vertical velocities (w_g) at the LCL. The scheme then uses the Lagrangian parcel method to simulate the ascent of the convective updraft including effects such as entrainment, detrainment and water loading (Kain 2004). Kain (2004) suggests that the updraft model formulation acts as additional trigger criteria for deep moist convection above the LCL, by determining whether or not the required minimum cloud-depth (2-4 km) is achieved. The updraft may be prevented from reaching this minimum depth criterion if entrainment of environmental air causes it to become negatively buoyant within the cloud. While this may be true, such a formulation to account for negative buoyancy above the LCL is only an implicit constraint which can often times be too weak. Consider, for example, the sounding shown in the left panel of Fig. 2.10 (b). Immediately above the LCL, the convective updraft rises through layers of negative buoyancy and low environmental relative humidity where detrainment dominates, and the entrainment rate is expected to be only a minimum as opposed to being a maximum (Kain 2004). In such a case, the dilution with the environmental air clearly does not work to inhibit the updraft from reaching its LFC. Thus, it appears that the present considerations for parcel buoyancy above the LCL do not effectively suppress deep convection at all times. The decision to activate moist convection or convective updrafts at the LCL, with weak or implicit constraints for CIN above it, is common in

other schemes as well (Tiedtke 1989, Fritsch and Chappell 1980). Not only can this assumption result in premature deep convection, but it may also produce overactive shallow convection.

Sometimes, an updraft may reach the LFC through the layers of negative buoyancy but is unable to fulfill the minimum cloud-depth criterion. In this case, the scheme may activate shallow convection, which brings about mixing within the cloud and preconditions it for the occurrence of deep convection at a later time. Such an example is shown in Fig. 2.11. The sub-cloud layer shows similar properties for both parameterized and explicit grids. However, it appears that shallow convection has removed the negative buoyancy above the LCL (seen in right panel of Fig. 2.11), thereby enabling an easy triggering of parameterized deep convection which occurs at this hour (left panel of Fig. 2.11). Note that explicit convection is inhibited at this grid point. The effect of overactive shallow convection is analogous to that reportedly

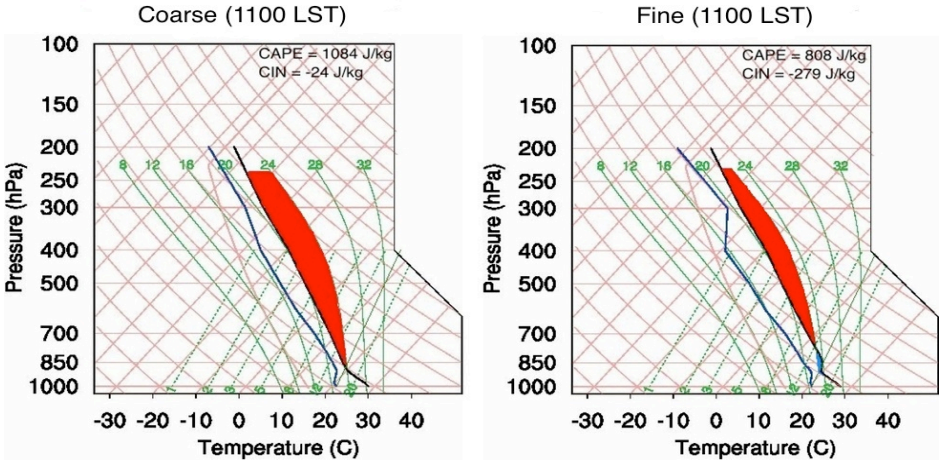

Figure 2.11 Representative skew T-log P soundings obtained over co-located grid points in the coarse (left) and fine (right) grids at the hour of initiation of parameterized deep convection (1100 LST), on Aug 26, 2007. The sounding in this figure is obtained from the sensitivity run using KF scheme (see Appendix for location index).

observed in the BMJ scheme (Baldwin et al. 2002), and appears to contribute to premature convection. Thus, it is evident that the negative buoyancy above the LCL needs more stringent or explicit considerations, and must be accounted for *prior to* the triggering of moist (shallow and deep) convection.

2.3.7 A simple modification to the Kain-Fritsch scheme

In order to further investigate the KF scheme's sensitivity to the negative buoyancy above cloud-base, a simple modification is made such that moist convection begins only when the LCL and LFC are at the same pressure level. By doing so, it is assumed that the mesoscale resolvable model processes (such as mass convergence, moisture advection, mixing due to diurnal heating) will overcome CIN and raise the LCL to the LFC prior to activating shallow or deep moist convection (similar to explicitly triggering convection). Such an assumption may perhaps be too stringent for coarse resolution models, since it is often argued that weak parcel buoyancy constraints are necessary to produce sub-grid scale convection at large horizontal grid-spacing. As a result, cumulus parameterization schemes are typically designed to trigger convection from the LCL (not LFC), using only modest considerations for CIN above it (if at all). In this study, the modified scheme (referred to as KF_{CIN}) is tested using 37.5 km horizontal resolution to investigate whether the mesoscale model is able to overcome CIN, and rightly trigger parameterized convection from the LFC.

A new version of WRF (3.4.2) is used because it includes an alternative trigger function for the KF scheme based on the large-scale three-dimensional moisture advection (KF_{MA}; Ma and Tan 2009). Just like the original KF scheme, this revised trigger initiates moist convection from the LCL but uses the grid-resolved moisture

advection instead of vertical velocity in the buoyancy criteria (Eq. 2.3). This large-scale trigger has been shown to be more useful for tropical cyclone prediction in a synoptically weak environment where "lifting" mechanisms are not that important for convective initiation (Ma and Tan 2009). The performance of the modified scheme (KF_{CIN}) is compared with both the original (KF) and the revised (KF_{MA}) schemes. Other than the choice of the cumulus scheme, the model configuration remains the same as the control simulation. Model ensemble simulations are performed for five (out of six) convective cases using KF_{CIN}. Results suggest that although adequate rainfall is produced with the modified trigger (KF_{CIN}), there may not be a large improvement in the phase and amplitude of mean rainfall. However, the improvement is in the right direction. Figure 2.12 compares the temporal evolution of the mean forecast for Aug 25, 2007 and Aug 05, 2010 (both cases discussed in section 2.3.5). For the first case with no surface fronts, both the large-scale triggers (KF and KF_{MA}) are unable to capture the magnitude of the convective peak (Fig. 2.12 (a)). The KF_{CIN} marginally improves the amplitude. For the second case (Fig. 2.12 (b)), it delays the initiation as well as peak of convection compared to the original KF scheme, thereby improving the overall representation of the phase. Thus, although the simple modification to account for CIN only introduces a slight delay in the phase, it is in the positive direction. If buoyancy constraints were to be better designed, it is possible that a greater improvement may result, and the discrepancies between the two large-scale triggers (KF and KF_{MA}) may be further reduced. It is worth inspecting the performance of KF_{CIN} in a climate simulation over the US.

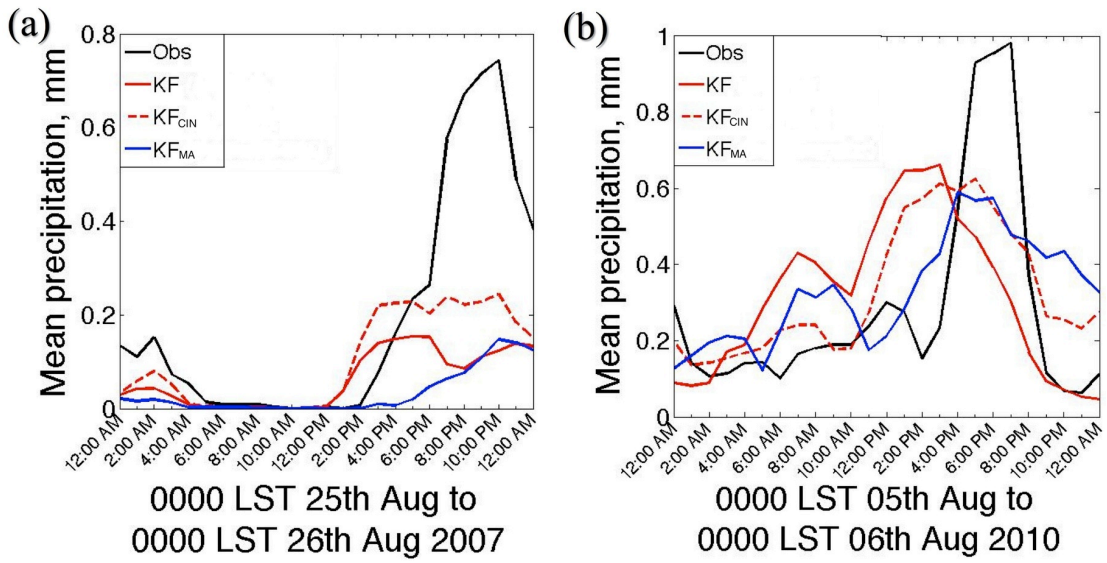

Figure 2.12 The diurnal cycle of mean precipitation for (a) Aug 25, 2007; and (b) Aug 05, 2010 obtained using Stage IV observations (Obs), the original Kain-Fritch scheme (KF), the modified Kain-Fritsch scheme (KF_{CIN}) and the Kain-Fritsch scheme with revised large-scale trigger (KF_{MA}).

2.3.8 Performance of the modified Kain-Fritsch scheme in a climate simulation

In order to ensure that the modified scheme (KF_{CIN}) does not produce drought in other midlatitude regions, a seasonal simulation is carried out with WRF (3.4.2) model, using forcing conditions from the North American Regional Reanalyses (NARR; Mesinger et al. 2006) for the warm season months (JJA) of 2009. A spin-up time of 7 days is used. The model configuration remains the same but a horizontal resolution of 32 km (same as NARR) is used. The seasonal total accumulated precipitation is compared in Fig. 2.13. The model has a dry bias compared to the Stage IV observations in almost all parts of the country, but especially in the Great Plains region. The KF_{CIN} simulation does not appear to worsen this bias. For example, the region around the Great Lakes in the Midwest receives lesser rainfall totals when KF_{CIN} is used, but in most places of the Southeast US as well as northern Texas, the

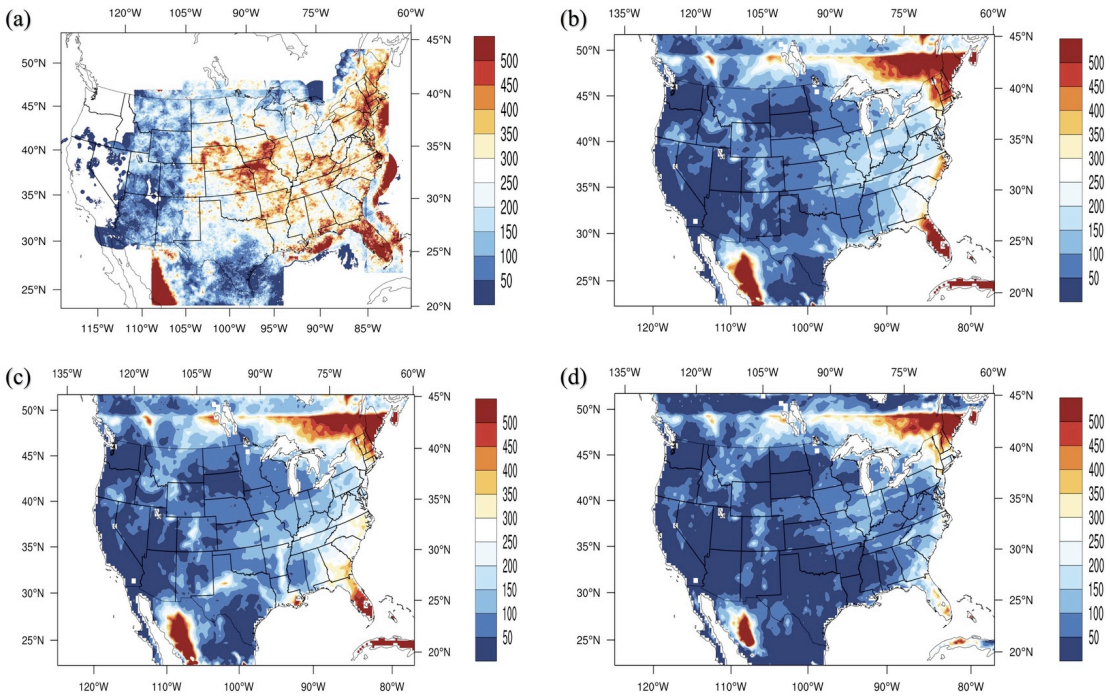

Figure 2.13 The seasonal accumulated rainfall (JJA 2009; mm) over the continental US, for (a) Stage IV observations, and for model output using (b) KF scheme, (c) KF_{CIN} scheme, and (d) KF_{MA} scheme.

dry bias is reduced to some extent. Thus, by employing proper buoyancy constraints, the rainfall amount predicted by the model may even increase in some areas. Note that the dry bias, especially in the southeast, is more significant when KF_{MA} is used. This could be because the large-scale trigger based on moisture advection is less suitable for this region where moisture may not be a limiting factor for the occurrence of convection. The presence of lifting mechanisms (mass convergence) may be more important for convective initiation.

The phase and amplitude of the diurnal cycle simulated by the three versions of the KF scheme are shown in Figure 2.14 and 2.15, respectively. No striking differences are observed between the performance of KF and KF_{CIN}. In the KF_{MA} simulation, the amplitude of the diurnal cycle is widely overestimated over the Great

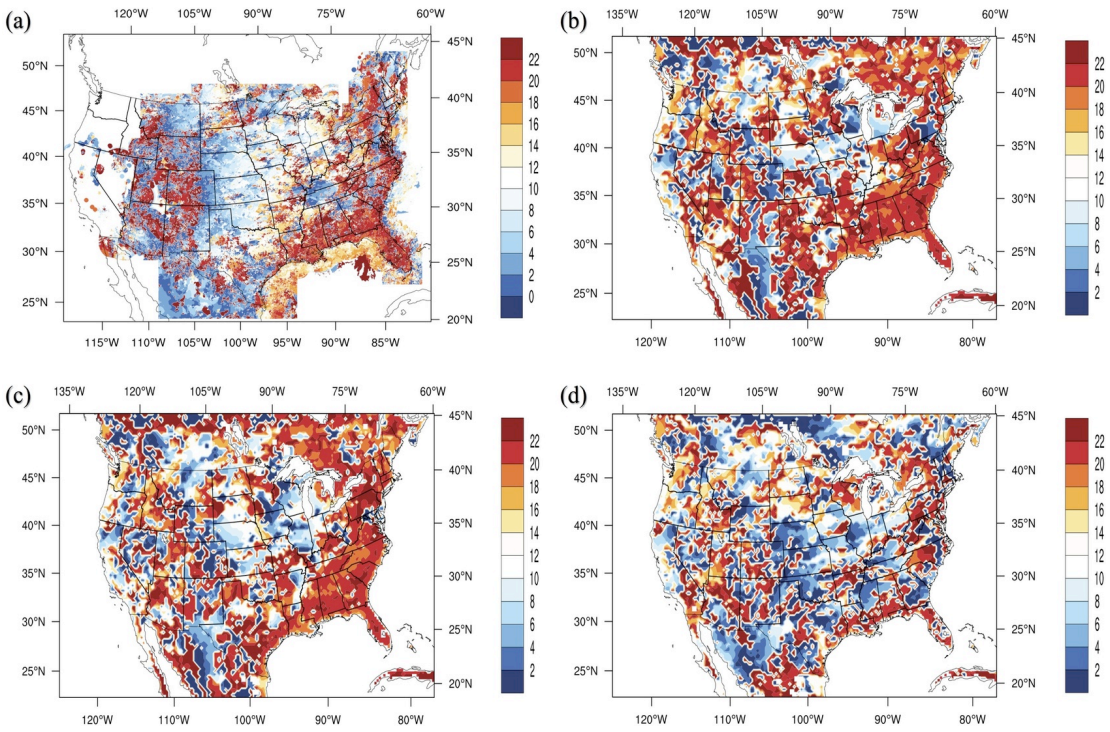

Figure 2.14 The phase of warm season rainfall (JJA 2009) representing the hour at which the diurnal rainfall maxima occurs over the continental US, for (a) Stage IV observations, and for model output using (b) KF scheme, (c) KF_{CIN} scheme, and (d) KF_{MA} scheme. The time coordinate is UTC.

Plains region. The KF and KF_{CIN} simulations, on the other hand, underestimate the amplitude over the western mountainous and southwest regions of the US. The KF_{CIN} appears to improve the representation of the phase of warm season rainfall in the Central Plains region, between 35° N and 45° N latitude (see Fig. 2.14 (c)). Time-longitude Hovmöller diagrams are used to investigate this feature more closely (Fig. 2.16). It appears that the stricter negative buoyancy constraint used in KF_{CIN}, may curb daytime convection east of 105° W, and thereby improve the nocturnal phase propagation of warm season rainfall. Both KF and KF_{MA} using varied large-scale triggers are unable to satisfactorily inhibit daytime convection in this region. Thus far, studies have shown that schemes using the free-tropospheric forcing work best for

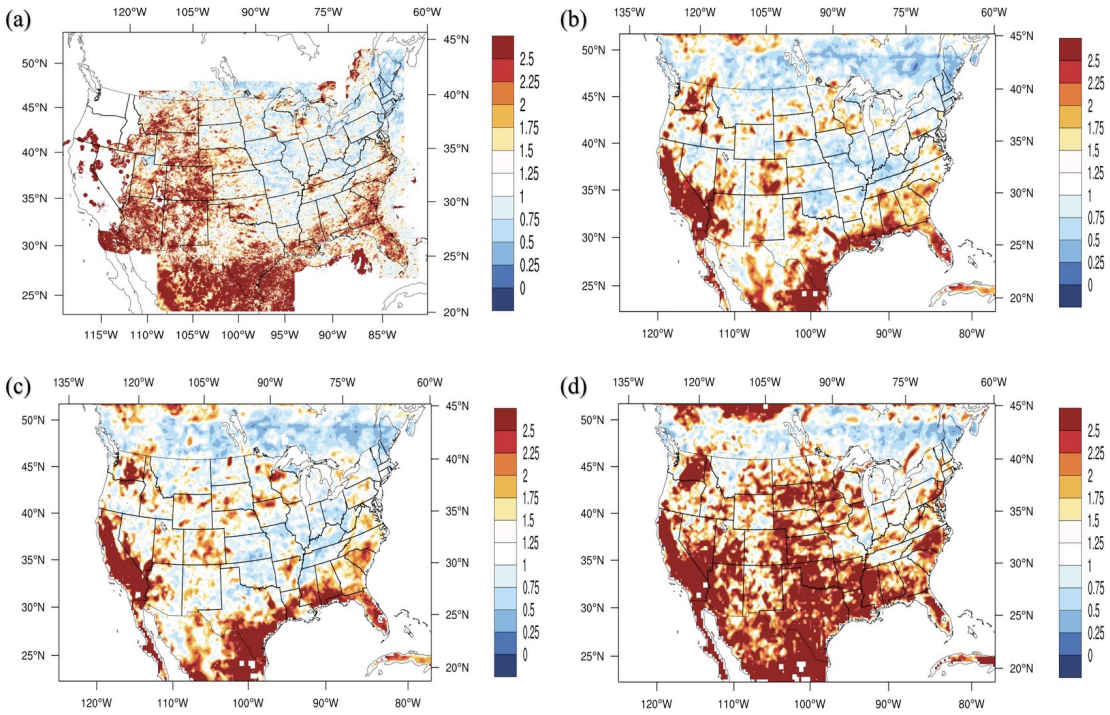

Figure 2.15 The amplitude of warm season rainfall (JJA 2009) over the continental US, for (a) Stage IV observations, and for model output using (b) KF scheme, (c) KF_{CIN} scheme, and (d) KF_{MA} scheme. The amplitude is the maximum hourly rainfall normalized with respect to the mean precipitation at each location.

capturing nocturnal rainfall (Zhang 2002; 2003; Lee et al. 2008). In fact, since the CAPE (or instability) has a daytime maximum for a surface-based or PBL-based parcel, authors have suggested decoupling convection from boundary layer processes in cumulus schemes for the purpose of producing the nocturnal phase of rainfall over the Great Plains region (Zhang 2002; 2003). Figure 2.16 (c) suggests that this may be achieved by a simple modification to the buoyancy trigger, and without excluding the boundary layer forcing which can be important for predicting daytime convection in other regions. Since the KF scheme's USL may originate from anywhere within the lowest 300 hPa of the atmosphere, the simulation of elevated (above boundary layer) nocturnal convection is also possible but only if the CAPE is not consumed by

overactive daytime convection. It therefore appears that by strengthening the trigger criteria in the Kain-Fritsch scheme (for e.g., KF_{CIN}), it is possible to better capture the geographical variability in the diurnal phase of warm season rainfall. Deficiencies and biases, along with the resolution sensitivity of the revised KF_{CIN} scheme, will be investigated in future studies.

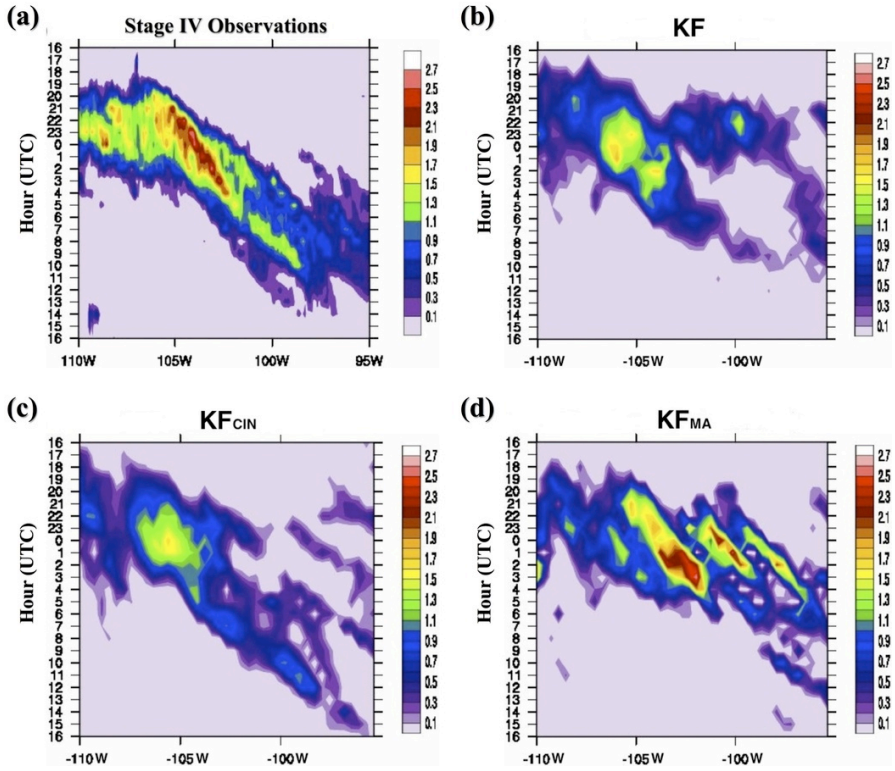

Figure 2.16 Hovmöller diagram (time versus longitude) representing the diurnal variation of normalized precipitation (positive only) averaged between 38° N –42° N, for (a) Stage IV observations, and for model output using (b) KF scheme, (c) KF_{CIN} scheme, and (d) KF_{MA} scheme. Normalized precipitation is the hourly rainfall normalized with respect to the mean at each location. The time coordinate is UTC.

2.4 Conclusions

An early bias in the onset and peak of surface-based convection is observed in the simulations of late-afternoon warm season precipitation events, using both the

BMJ and the KF cumulus parameterization schemes. The sensitivity of the simulated diurnal cycle of rainfall to model resolution and boundary layer physics is relatively low when convection remains parameterized. In contrast, the time-evolution of rainfall (including the early bias) displays higher sensitivity to explicit convection at increased horizontal resolution, and is significantly improved in comparison with observations. The contribution of the BMJ scheme's shallow versus deep convection to the problem of premature rainfall is investigated further. Although previous work has suggested an overactive shallow convection for the BMJ scheme (Baldwin et al. 2002), the present analysis indicates that an inadequate representation of CIN in the deep convective trigger may be responsible for the early rainfall bias.

Satellite-derived atmospheric soundings confirm the importance of this low-level negative buoyancy in influencing the timing of surface-based convection. The BMJ scheme includes an implicit constraint for the CIN between the LCL and LFC, which does not suppress deep convection but reduces its intensity. The KF scheme's decision to activate moist convection depends on the parcel buoyancy and the large-scale vertical velocity at cloud-base. This constraint also appears too weak, allowing moist convection (shallow and deep) to occur prematurely from the LCL (Fig. 2.10 and 2.11). A simple modification is made to strengthen the buoyancy criteria in the scheme, such that convection is only allowed to begin when the LCL and LFC are at the same pressure level. Even with this seemingly stringent constraint, the scheme is able to reproduce adequate rainfall, and in some cases may improve the early bias (Fig. 2.12 (b)). The scheme is tested in a mesoscale climate simulation to investigate whether widespread drought or other issues arise due to this modification. While there

are no major biases, an improvement in the nocturnal phase propagation of rainfall in the Central Plains (between 38° N to 42° N) is observed due to the curbing of daytime convection east of 105 °W (see Fig. 2.16). This suggests that the trigger constraints (especially the CIN below the LFC) used to represent non-equilibrium convection in mesoscale models are important, and need to be properly considered for improving the representation of the diurnal cycle of warm season rainfall (discussed in section 1.1). The ability of the modified KF scheme to produce daytime as well as nighttime phase of rainfall suggests that the Type I assumption for triggering convection may be favorable for mesoscale climate modeling. However, the model's performance appears to fall short in a number of places (for example, the dry bias observed in Fig. 2.13), which may not solely be related to random forecast errors. It is possible that the Kain-Fritsch scheme (both KF and KF_{CIN}) may have region or regime-specific biases. Moreover, the sensitivity of convective precipitation to the type of dynamical forcing (mass convergence versus moisture advection) is clearly evident in the large discrepancies observed between the KF and KF_{MA} simulations (section 2.3.8). This will be explored in future studies.

Chapter 3: A multi-city analysis of the UHI-influence on warm season rainfall.

Abstract

This study evaluates the influence of the Urban Heat Island (UHI) on warm season precipitation for several US cities by using contemporary high-resolution observations. Spatial (local and downwind) rainfall anomalies associated with propagating and non-propagating storms are analyzed using statistical methods. A diurnal trend analysis suggests that the UHI has a dominant influence on precipitation for inland cities (Minneapolis and Washington D.C.), especially during afternoon and nocturnal hours. Propagating storms appear to converge over the urban region, but the rainfall intensification occurs downwind of the city. The nocturnal precipitation anomaly, which has received less attention in the past, is significant and comparable to the daytime anomaly. For coastal cities (New York City, Providence and Cleveland), a local increase in the frequency and intensity of extreme positive rainfall anomalies may occur during the daytime due to the UHI-sea breeze interaction. For non-propagating storms, nocturnal rainfall enhancement is evident downwind of an inland city (Dallas), whereas a local daytime increase in the frequency of heavy rainfall events is observed for a coastal city (Houston). Downwind and nocturnal UHI impacts on rainfall appear less obvious for coastal cities. Further studies are clearly needed to better understand the variability in processes that produce urban rainfall enhancement, for example, rainfall increase in nocturnal propagating storms, and extreme positive rainfall anomalies due to UHI-sea breeze interaction.

3.1 Introduction

In the past, two approaches have been adopted to study climatological urban impacts on rainfall. The first consists of a multi-city approach to quantify the urban and downwind precipitation increase. The climatological mean wind direction has typically been used to determine the downwind impact region (Shepherd et al. 2002; Shepherd and Burian 2003; Westcott 1995; Huff and Changnon 1973; Ashley et al. 2012). For example, Huff and Changnon (1973) found a 9-17% increase in rainfall associated with cold frontal storms observed over and downwind of Midwest cities, and a similar increase for air-mass type thunderstorms over coastal cities in the US. They found that the maximum increase in storm frequency occurred during the late night and early morning hours (when the UHI is a maximum). The mechanism producing the nocturnal rainfall anomaly, also observed during METROMEX (Changnon et al. 1977; Changnon and Huff 1986), was not explored in detail. In another study (Westcott 1995), the analysis of cloud-to-ground lightning flashes over 16 central US cities indicated a similar increase in the flash rate associated with existing convective storms. Since the peak was observed during afternoon hours, the author attributed the cause to the UHI-perturbed boundary layer circulation (Westcott 1995). More recently, Shepherd et al. (2002) showed that an average of 28% increase in monthly mean rainfall rate was observed downwind of six US cities, and speculated that the UHI was mainly responsible. Although a common spatial rainfall anomaly pattern was observed across multiple cities, their study did not investigate the cause and variability, such as the storm-type (air-mass versus existing convective systems), diurnal trend (afternoon versus nighttime events), and so on. Similarly, Ashley et al.

(2012) used radar and lightning data to show urban and downwind effects on precipitation across several southeastern US cities. Once again, a temporal analysis was not carried out to investigate a diurnal effect, and the data were only analyzed during synoptically benign days when large-scale forcing is negligible. The observed spatial anomalies were not attributed to any specific urban mechanism.

A second approach that has been widely used in recent studies enables a more comprehensive understanding of climatological rainfall patterns observed over a single, selected city. This method typically uses high-resolution datasets (such as radar, lightning), which allow a more sophisticated spatiotemporal analysis compared to the METROMEX and older studies. Such analyses for propagating thunderstorms over New York City (Bornstein and LeRoy 1990) and Indianapolis (Niyogi et al. 2011) are discussed in Chapter 1 (section 1.2.2). The tendency of selecting an inland, isolated city such as Atlanta is also discussed (section 1.2.2). For example, Bentley et al. (2010) analyzed climatological radar data, and found a maximum in the medium to high reflectivities over Atlanta as well as the downwind region. They speculated that the UHI and enhanced surface roughness led to the urban maximum, whereas the storm bifurcation effect and the UHI-perturbed boundary layer circulation may cause the downwind maximum. That study did not use a diurnal trend analysis to further explore the speculated mechanisms. Moreover, the analyses only included synoptically benign days since previous studies had suggested that the UHI-induced convergence is most evident during calm conditions (Dixon and Mote 2003).

Thus, one problem with recent studies is that they are too restrictive in their approach which limits our understanding of the variability in UHI-rainfall impacts. In

this study, a broader, multi-city approach is adopted to exploit current high-resolution surface datasets. The goal is to investigate the UHI as a dominant mechanism in producing urban and downwind rainfall anomalies, and to explore its variability. Several US cities are considered based on the occurrence of a well-defined UHI. This increases the possibility of observing a UHI-signature on rainfall patterns that may otherwise be overshadowed due to external influences such as coastal mesoscale circulations, aerosols, etc. Statistical methods are employed to analyze trends in the rainfall anomalies by considering factors such as diurnal variability, differences in geographical setting (coastal versus inland cities), and storm-type (propagating versus non-propagating). For propagating storms, the downwind impacts are explored by tracking each individual storm as opposed to using the climatological wind direction. Note that Perryman and Dixon (2013) recently adopted a similar approach for analyzing UHI impacts associated with propagating winter snowstorms. My focus here is the on the warm season precipitation.

3.2 Material and Methods

3.2.1 Datasets

The 30 m resolution National Land Cover Dataset (NLCD 2006) (Homer et al. 2012) is used to identify urban regions over the continental US based on Impervious Surface Area (ISA) classification. The 5 km resolution Real-Time Mesoscale Analysis (RTMA) dataset (Manuel et al. 2011) is used to obtain surface meteorological variables such as temperature, dew point and cloud cover, which will help determine

the presence of a robust UHI. The NCEP/EMC Stage IV precipitation dataset (Baldwin and Mitchell 1996; Lin and Mitchell 2005), available at 4.7 km resolution, is used for analyzing precipitation patterns. Surface pressure and above-surface wind data are obtained from the North American Regional Reanalysis (NARR) (Mesinger et al. 2006). Since the RTMA data is currently available for a 2-year period from 2007 to 2008, the analyses in this study are carried out for these two summer seasons (JJA) only.

3.2.2 Selection of cities

The NLCD land cover data is mapped onto the native RTMA grid at 5 km resolution using the nearest neighbor interpolation approach. Twenty-eight largest cities are identified using three types of land cover as criteria for constructing urban polygons, namely, low (20-49% ISA), medium (50-79% ISA) and high (80-100% ISA) intensity developed land, but excluding developed open space (ISA < 20% of total cover). The criteria appear to define all major city boundaries reasonably well barring Atlanta. Atlanta has two overlapping contours of ISA ≥ 20% that merge into one urban polygon after including open developed spaces in the above criteria. Daily meteorological parameters from the RTMA dataset such as temperature, dew point and cloud cover, are calculated for the warm season (2007-08), by averaging the variables within each city polygon. The rural temperature is calculated by averaging within a surrounding ring located at a distance of 30-60 km away from the city polygon boundary (see Fig. 3.1). Rural grid points are masked in order to exclude water bodies and points with considerable elevation differences (> 100 m with respect to the urban mean elevation). Cities that have more than 75% of surrounding grid points masked

(Denver, Los Angeles, San Diego, Portland, and Seattle) are disregarded. If the rural ring contains land cover points with ISA ≥ 20% due to overlap with a neighboring urban center (for example, cities in the northeast US), then these points are also excluded from the temperature anomaly calculation.

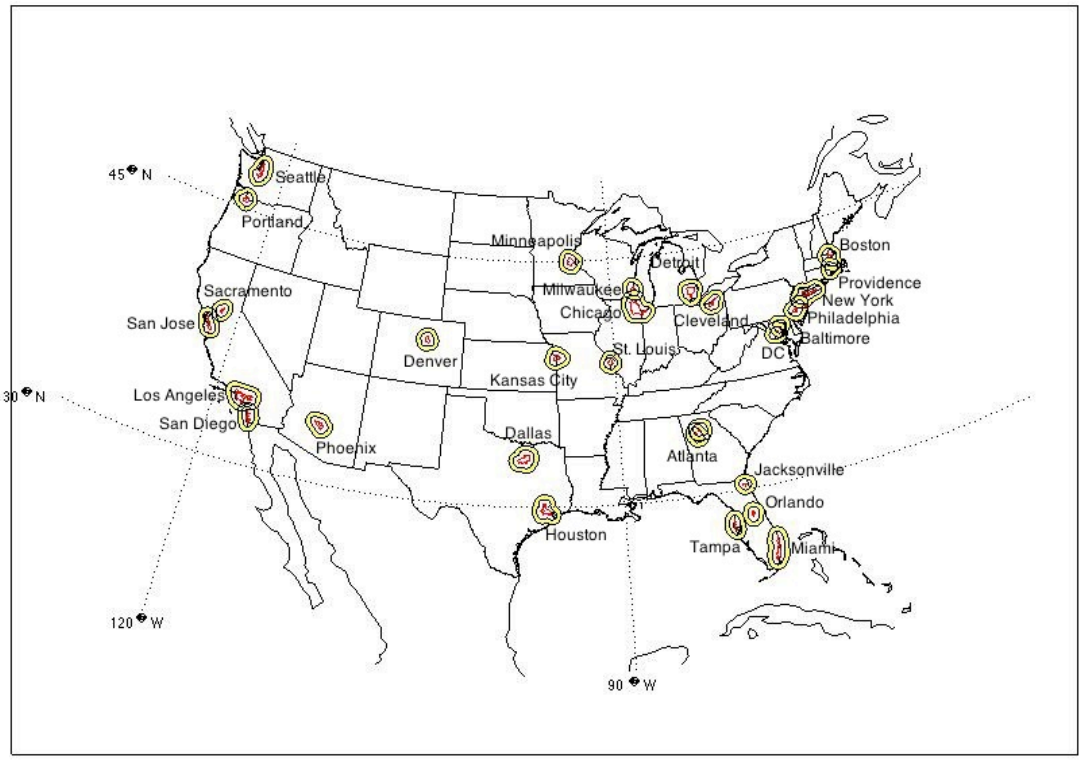

Figure 3.1 Twenty-eight largest urban regions (red polygons) over the continental US along with surrounding rural areas (yellow rings). The urban polygons are identified using ISA contours (≥20%) from the NLCD (2006) data, and are represented on the RTMA grid at 5 km horizontal resolution (see text for abbreviations).

Daytime temperature anomalies (TA_{day}) are calculated as the maximum temperature difference (urban minus rural) that occurs between 1000 to 1800 LST, while nighttime temperature anomaly (TA_{night}) is the same but observed between 2000 to 0700 LST. Both TA_{day} and TA_{night} are found to be significantly positive for all cities. With the exception of Baltimore and Sacramento, the nighttime temperature increase is found to

be more robust than daytime. The observed mean dew point temperature and mean cloud cover values over each city are also noted at the hour of nocturnal maximum temperature difference.

As discussed in Chapter 1 (section 1.2.1), previous studies have shown cloud cover and humidity to be negatively correlated with the nocturnal UHI (Sundborg 1950; Duckworth and Sandberg 1954; Morris et al. 2001; Sheridan et al. 2000). Table 3.1 lists the correlation coefficients for TA_{night} and synchronous observations of these meteorological parameters, computed for the 23 cities. The second and third columns in Table 3.1 provide the correlation coefficient (r_{cc}) corresponding to cloud cover along with the number of days with valid observations, respectively. A negative correlation is observed for a majority of the cities indicating that the differential radiative cooling may indeed be contributing to nighttime temperature anomalies. The fourth column lists correlation coefficient (r_{dpt}) for surface dew point temperature and TA_{night} computed from observations taken over the entire period of two summers (n = *181* days). Once again, the relationship is mostly negative, though a significant positive correlation exists for some cities (Boston, Jacksonville, Miami, Kansas City, Phoenix, and San Jose). For these cities, it is not entirely clear whether the temperature anomaly occurs due to the urban land cover. Since the aim is to investigate the UHI-influence on rainfall patterns, only those cities that have a negative correlation of TA_{night} with cloud cover and dew point are selected, requiring that at least one correlation be statistically significant ($p \leq 0.1$). In Table 3.1, the cities with a significant negative correlation with both meteorological parameters include Cleveland, Dallas, Minneapolis, New York City, Providence, and Sacramento (marked

with a '*' symbol). Apart from these, Houston and Washington D.C. (marked with a '+' symbol), are also selected. For these two cities, r_{cc} and r_{dpt} are both negative, but only the correlation with the dew point temperature is statistically significant.

Table 3.1 Correlation coefficients computed for daily nighttime temperature anomalies (TA_{night}) and synchronously observed meteorological parameters (cloud cover and surface dew point). Cities that have TA_{night} significantly correlated (negative) with both parameters are marked with a '*' symbol. Cities that have TA_{night} negatively correlated with both parameters with a significant relation only with dew point are marked with a '+' symbol.

City	**Correlation coefficient for TA_{night} and cloud cover (r_{cc})**	**Days with cloud cover data**	**Correlation coefficient for TA_{night} and dew point (r_{dpt})**
Atlanta	-0.1391	79	-0.0852
Baltimore	-0.0561	82	0.0114
Boston	-0.1513	82	0.1848
Chicago	0.0731	70	-0.0169
*Cleveland	-0.1565	78	-0.3524
*Dallas	-0.1921	73	-0.3031
+DC	-0.1160	80	-0.1205
Detroit	0.0079	67	-0.1014
+Houston	-0.1303	74	-0.2323
Jacksonville	-0.0225	78	0.1120
Kansas City	0.1355	74	0.1818
Miami	0.0514	59	0.1842
Milwaukee	0.0592	70	0.0908
*Minneapolis	-0.2481	54	-0.1287
*New York	-0.4493	75	-0.1745
Orlando	0.0393	74	0.0860
Philadelphia	0.0401	76	0.0477
Phoenix	-0.1103	67	0.2567
*Providence	-0.1853	82	-0.1377
*Sacramento	-0.3863	17	-0.0976
San Jose	0.1622	18	0.3396
St.Louis	0.0292	67	-0.0663
Tampa	-0.0672	86	-0.0230

The nocturnal and daytime temperature anomalies for 6 out of the 8 selected cities are positively correlated, indicating that TA_{day} may also carry an UHI signal. In order to confirm this, the correlation between TA_{day} and the logarithm of the city size is explored based on previously established log-linear relationships for North American cities (Landsberg 1981; Imhoff et al. 2010). City size conventionally refers to population data (Landsberg 1981) that are obtained from the United States Census (2010) for this study. A significantly positive correlation is found between TA_{day} and the logarithm of population (Fig. 3.2 (a)). This gives us confidence that the selected cities have a discernible nighttime as well as daytime UHI. Imhoff et al. (2010) established a log-linear relationship between the urban surface area defined by percent impervious cover and the skin temperature difference (urban minus rural) for Northeastern US cities. Figure 3.2 (b) shows that a similar relation between the surface area of urban polygons and TA_{day} exists for the selected cities.

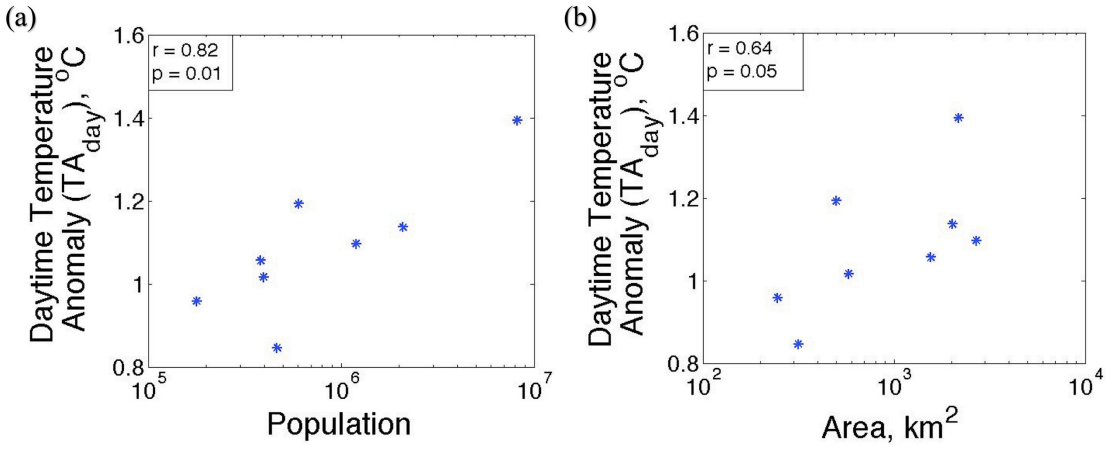

Figure 3.2 The mean daytime temperature anomaly (TA_{day}; Y-axis) and the city size (logarithmic X-axis) for the selected cities along with the correlation coefficient (r) and p-value of significance (p). The city size refers to (a) population and (b) urban polygon area based on percent impervious cover (ISA ≥20%). The selected cities include Cleveland, Dallas, Minneapolis, New York City, Providence, Sacramento, Houston, and Washington D.C.

3.2.3 Climatological rainfall and storm classification

Prior to analyzing warm season rainfall patterns, the climatological precipitation and the prevalent storm-type for each of the selected cities are examined. Sacramento receives a climatological average of only 6.9 mm (0.27") rainfall during summer (Western Regional Climate Center, 2013). Moreover, the years 2007 and 2008 were drought years in the Western US, and no rainfall accumulation is recorded over Sacramento. This city is therefore excluded from my analyses. The rest of the cities are classified considering the major climatological storm-type, i.e., propagating versus non-propagating. For this purpose, sub-synoptic surface weather maps from the National Weather Service's Hydrometeorological Prediction Center and Unisys Weather are used to identify propagating mesoscale boundaries including fronts, low-pressure systems, surface troughs, outflow boundaries, and squall lines. In addition to the Stage IV rainfall observations, the 2 km radar reflectivity images (obtained from the Mesoscale and Microscale Meteorology Image Archive and College of DuPage's Next Generation Weather Lab) are used to determine the direction of propagation for rain-producing storms. Minneapolis, Cleveland, Providence, Washington D.C. (DC), and New York City (NYC) received more than half of the warm season precipitation from such propagating systems during 2007-08. Both the southern cities of Dallas and Houston, on the other hand, experience less than 30% rainfall from well-defined mesoscale propagating boundaries during summer (2007-08). Therefore, the major storm-type associated with these cities is considered to be stationary or non-propagating.

In previous long-term studies that assessed urban effects on precipitation, the

upwind control and the downwind impact regions were typically determined from the most frequent direction of the climatological storm movement or the 700 hPa level winds (Shepherd et al. 2002; Huff and Changnon 1973). In this study, a similar approach will be adopted but only for Dallas and Houston. For the remaining cities, each propagating rain-producing storm is tracked, and the upwind and downwind regions are defined according to the direction of propagation. The propagation axis is classified based on the 8 standard directions of the compass, viz., NS, NE-SW, EW, SE-NW, SN, SW-NE, WE or NW-SE. The schematic shown in Fig. 3.3 illustrates the control and impact regions along with the storm propagation axis for an eastward propagating storm. Such a classification of impact regions is quite redundant, primarily because the high temporal resolution of the rainfall (hourly) and radar (30-minute) data allows for the spatiotemporal tracking of the storm's movement through the urban environment. The storm typically propagates through the region over a period of 3-4 hours, providing at least a one-hour interval between the time of its occurrence at upwind, urban and downwind locations. (Note: For DC, the grid points

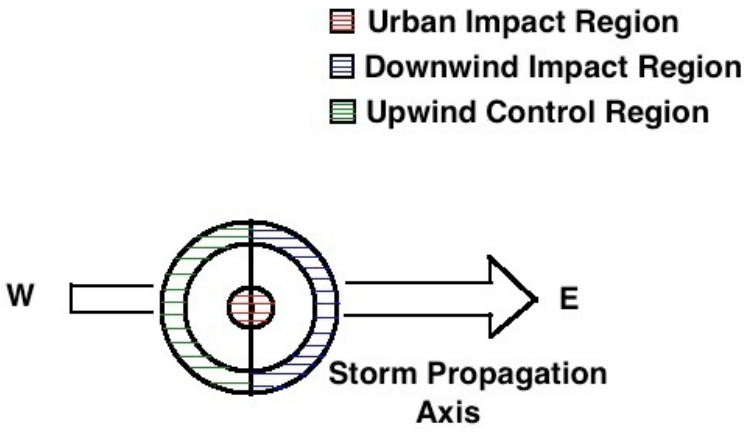

Figure 3.3 Schematic representing the storm propagation axis along with the upwind control, urban impact and downwind impact regions defined based on the direction of storm movement for an eastward propagating storm.

in the downwind impact region are often masked by the Chesapeake Bay. Therefore, the surrounding rural ring is extended inwards to enclose a region that is 10-60 km away from the urban polygon boundary).

3.2.4 Calculation of rainfall anomaly over urban and surrounding regions

The rainfall in the urban and downwind impact regions is compared against the upwind control region using two ratios; mean and maximum rainfall anomaly. For each region, the mean rainfall is computed as the spatial average over grid points with measurable precipitation (P > 0.25 mm). The percent urban and downwind mean rainfall anomaly is then calculated using the following equations.

$$\text{Urban Mean Rainfall Anomaly } (URA_{mean}) = \frac{[\text{Urban Mean Rainfall} - \text{Upwind Mean Rainfall}]}{\text{Upwind Mean Rainfall}} \times 100. \quad (3.1)$$

$$\text{Downwind Mean Rainfall Anomaly } (DRA_{mean}) = \frac{[\text{Downwind Mean Rainfall} - \text{Upwind Mean Rainfall}]}{\text{Upwind Mean Rainfall}} \times 100. \quad (3.2)$$

The maximum precipitation intensity (hourly rainfall rate) recorded within each region is used to compute the maximum rainfall anomaly using equations 3.3-3.4. This anomaly is a useful measure of the rainfall intensification of existing storms as they pass through an urban area.

$$\text{Urban Maximum Rainfall Anomaly } (URA_{max}) = \frac{[\text{Urban Maximum Rainfall} - \text{Upwind Maximum Rainfall}]}{\text{Upwind Maximum Rainfall}} \times 100. \quad (3.3)$$

$$\text{Downwind Maximum Rainfall Anomaly } (DRA_{max}) = \frac{[\text{Downwind Maximum Rainfall} - \text{Upwind Maximum Rainfall}]}{\text{Upwind Maximum Rainfall}} \times 100. \quad (3.4)$$

Although the above calculations are fairly simplistic, the percentages are not used to quantify the "absolute" UHI impact on rainfall. The main purpose is to compare the spatial rainfall patterns observed during different events. More specifically, to investigate the probability that urban and downwind regions act as favored zones of convergence and intensification of propagating storms. In some cases, a reverse calculation is employed to compute an upwind rainfall anomaly with respect to the downwind and urban regions (see Eq. 3.5). If it is assumed that an urban influence will not be present in the upwind region, then such a calculation serves to distinguish UHI effects from those due to other local mesoscale circulations especially for coastal cities.

$$\text{Upwind Rainfall Anomaly} = \frac{[\text{Upwind Rainfall} - \text{Downwind (Urban) Rainfall}]}{\text{Downwind (Urban) Rainfall}} \times 100. \quad (3.5)$$

The following section discusses the observed UHI impacts on propagating storms over Minneapolis, DC, Providence, NYC, and Cleveland (section 3.3.1), and non-propagating events over Dallas and Houston (section 3.3.2).

3.3 Results

3.3.1 The UHI impact on propagating storms

3.3.1.1 Distribution of rainfall anomalies

Figures 3.4 and 3.5 represent the distribution characteristics of urban and downwind rainfall anomalies associated with propagating storms for each city.

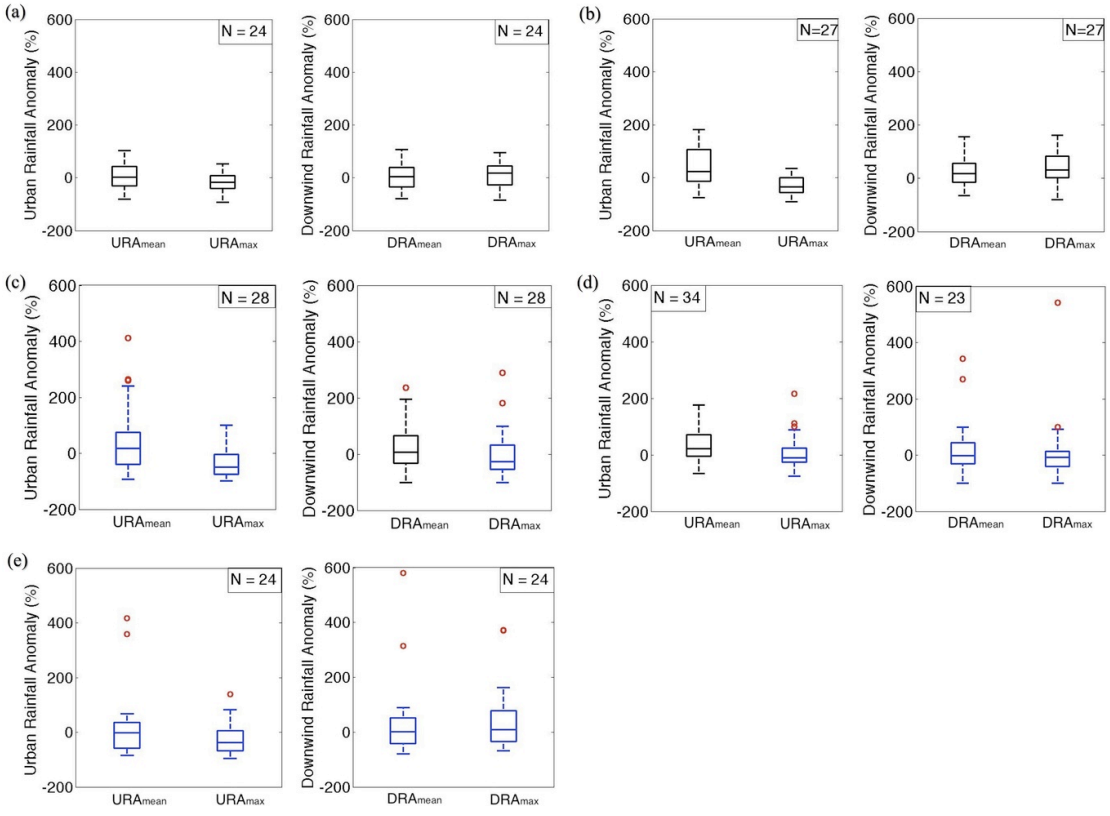

Figure 3.4 Box-and-whisker plots representing the quartiles of rainfall anomalies for (a) Minneapolis, (b) DC, (c) Providence, (d) NYC, and (e) Cleveland. Outliers (red circles) are data points that exceed the third quartile (75th percentile) by a distance greater than 1.5 times the interquartile range. Black boxes represent distributions that may be considered Gaussian whereas blue boxes represent distributions that deviate significantly from normality as determined by the Shapiro-Wilks test. The number of events considered for each city is denoted by *N*.

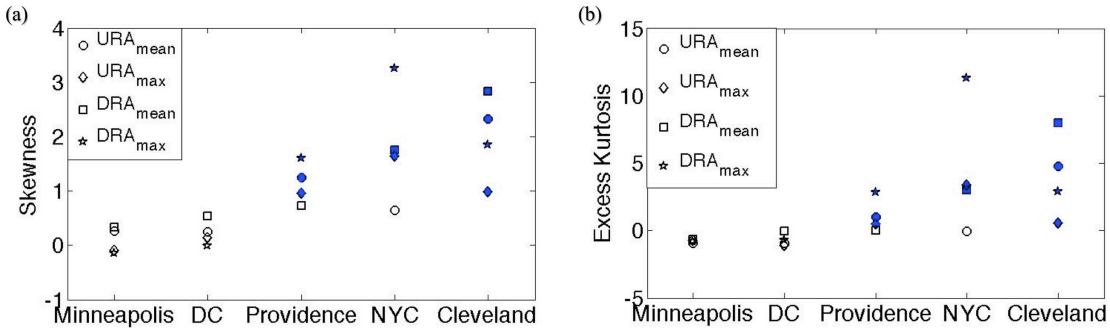

Figure 3.5 The skewness and excess kurtosis of rainfall anomaly distribution for various cities. The blue symbols represent anomalies that deviate significantly from normality as determined by the Shapiro-Wilks test.

The number of events considered is denoted by *N* (see Fig. 3.4). Other than the maximum rainfall anomalies over Minneapolis (URA_{max} and DRA_{max}) and DC (DRA_{max}), all other distributions are positively skewed (Fig. 3.5 (a)). This is expected since the anomaly calculation (Eq. 3.1-3.4) imposes a lower bound (-100%), which may naturally introduce right skewness in the distribution. Despite this, the rainfall anomalies over Minneapolis and DC are found to have low skewness and kurtosis, indicating a nearly symmetric distribution with short or thin tails. For example, Figure 3.6 (a) shows that the distribution of downwind maximum rainfall anomalies for Minneapolis is well-represented by the normal probability density function. For the remaining cities, an increase in both skewness and excess kurtosis (Fig. 3.5) suggests a more heavy-tailed distribution. In fact, the colored (blue) symbols in Figures 3.4 and 3.5, represent anomaly distributions that deviate significantly from normality as determined by the Shapiro-Wilks test ($p = 0.05$). The probability density function for such anomalies resembles a Generalized Extreme Value (Type II) distribution (for e.g., 3.6 (b)). This non-Gaussian behavior is a result of outliers associated with extreme positive anomaly events.

Positive outliers are defined as data points exceeding the 75^{th} percentile by a distance greater than 1.5 times the interquartile range (red circles in Fig. 3.4). These events tend to occur in the coastal cities of Providence, NYC, and Cleveland. A reverse calculation used to compute upwind rainfall anomalies with respect to the downwind or urban region (Eq. 3.5), indicates that similar outliers may also exist in the upwind region. This suggests that the extreme rainfall anomalies (outliers) observed in coastal cities arise due to the local sea breeze or lake breeze circulations

which may introduce considerable mesoscale heterogeneity in storm precipitation characteristics. For Minneapolis, which lies in the Central Plains, and for the DC urban area that lies inland of the Chesapeake Bay, the mesoscale variability in spatial precipitation patterns appears to be less pronounced. These cities are more likely to represent pristine UHI effects on rainfall modification.

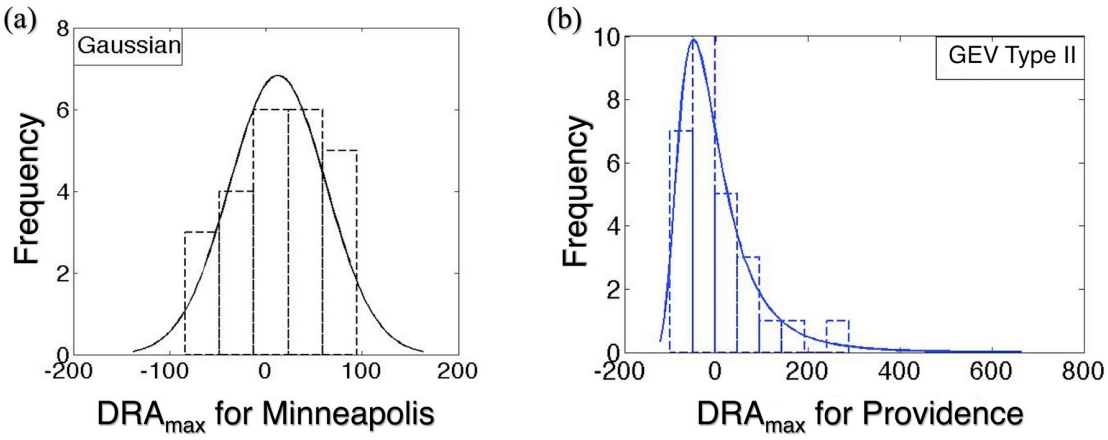

Figure 3.6 Histogram and probability density function using the Maximum Likelihood Estimate (MLE) method of curve-fitting for DRA_{max}. The anomalies follow (a) Gaussian distribution for Minneapolis, and (b) Generalized Extreme Value (GEV) Type II distribution for Providence.

3.3.1.2 Rainfall anomalies for inland cities

Figure 3.7 shows the diurnal distribution of rainfall anomalies over Minneapolis. Positive anomaly events are mainly observed during the night and afternoon hours (shaded in Fig. 3.7 (a)). This suggests that an urban-induced thermal forcing may indeed be present since the atmospheric UHI typically peaks at night whereas the UHI-perturbed boundary layer circulation is most pronounced during the daytime (Ackerman et al. 1977, Shepherd 2005). It is possible that the perturbations caused due to each of these phenomena are responsible for the distinct pattern of

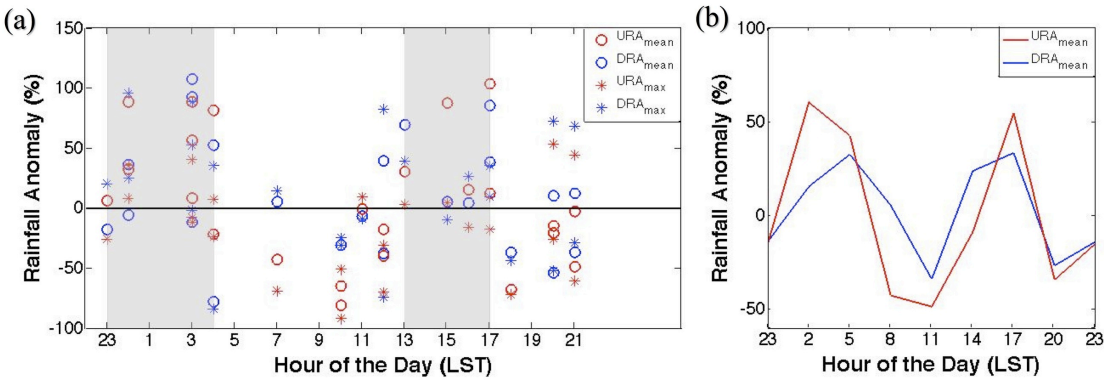

Figure 3.7 The diurnal pattern of rainfall anomaly associated with propagating storms over Minneapolis represented by (a) individual events, and (b) the 3-hour average anomaly computed from selected individual events. The shaded regions in (a) represent the nocturnal and afternoon periods when the anomalies are largely positive. Note that the range of the Y-axis in (b) is intentionally smaller to emphasize on the bimodal peak of the diurnal rainfall anomaly distribution.

diurnal rainfall anomaly distribution observed in Fig. 3.7. A similar double peak was also observed during METROMEX but only in the region downwind of St. Louis (Changnon et al. 1977). As discussed in Chapter 1 (section 1.2.2), the afternoon peak was related to the downstream propagation of the UHI-perturbed boundary layer circulation, but the nocturnal downwind rainfall increase was not investigated in detail (Ackerman et al. 1977; Changnon and Huff 1986). Changnon and Huff (1986) reported that this nocturnal anomaly was mainly associated with well-organized convective systems. In a following subsection (3.3.1.5), I will explore a possible cause for the nocturnal PBL instability that may enhance rainfall associated with propagating storms. For the present study, the mean anomaly (percent increase) observed over Minneapolis and the downwind region is listed in Table 3.2. Note that the urban region has a significant increase in the mean (URA_{mean}) but not the maximum rainfall anomaly (URA_{max}). This is because even though storms often converge over the urban area, the intensification of rainfall occurs mainly in the downwind region. Studies

during METROMEX also reported that the strongest urban-related stimulation of propagating storms occurred in the downwind region (Changnon et al. 1977; Ackerman et al. 1977). Figure 3.8 shows the accumulated rainfall associated with a daytime and a nighttime propagating event over Minneapolis. The downwind rainfall enhancement is evident for both cases.

Table 3.2 The mean urban and downwind rainfall anomaly (%) and standard deviation observed during afternoon (1300 to 1700 LST) and nocturnal (2300 to 0800 LST) periods over Minneapolis. The p-value is mentioned for a significantly positive increase in the mean rainfall anomaly (≤ 0.1).

Anomaly	Mean Rainfall Anomaly (%)	Standard Deviation	p-value
Afternoon			
URA_{mean}	49.4	42.5594	0.05
DRA_{mean}	40.2	36.7110	0.05
URA_{max}	-9	11.4455	-
DRA_{max}	19.8	20.2657	0.05
Night			
URA_{mean}	32.6667	48.7827	0.05
DRA_{mean}	19.7778	58.1007	-
URA_{max}	-5.4444	33.3396	-
DRA_{max}	27	52.9363	0.1

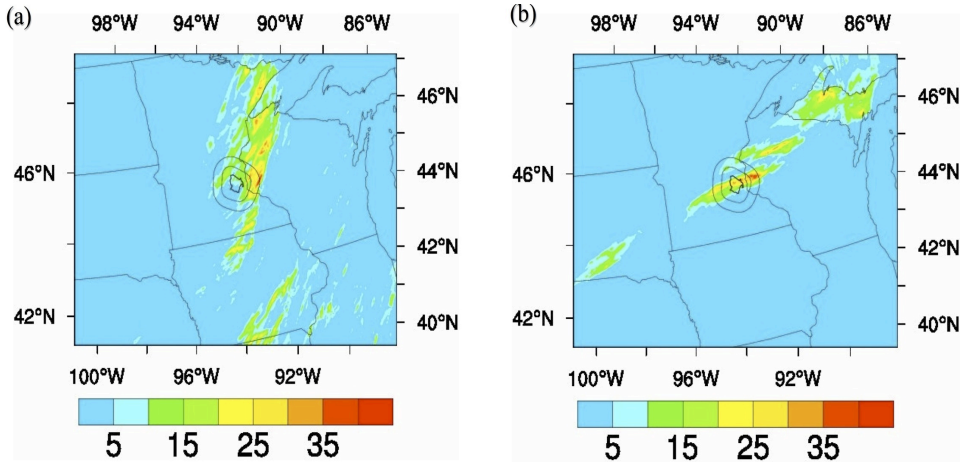

Figure 3.8 (a) 4-hr accumulated precipitation associated with a westerly cold front, and (b) 3-hr accumulated precipitation associated with a westerly surface low-pressure system, propagating through Minneapolis between 1000 to 1400 LST on 18 June, 2007, and 0100 to 0400 LST on 28 August, 2007, respectively. Bold solid line represents the city polygon and thin solid lines represent the surrounding rural ring.

A bimodal pattern in the diurnal distribution of urban mean rainfall anomaly is also observed over DC (Fig. 3.9). Once again, there is a statistically significant increase in the urban mean rainfall but not URA_{max} values (Table 3.3). The downwind anomalies are significantly positive during nocturnal and afternoon hours (Table 3.3), but do not show a prominent double peak such as the urban mean anomaly (Fig. 3.9 (b)). The increase in downwind rainfall is observed almost throughout the day, barring events occurring between 2000 and 2200 LST (see Fig. 3.9 (a)). One explanation is that in addition to the UHI impact, the downwind region may experience a bay breeze convergence effect which is known to be prevalent in the western Chesapeake Bay area (Flood 2004; Zhang et al. 2011). Since most of the storms (more than 85%) propagating through this region are westerly, the bay breeze convergence may favor positive downwind rainfall anomalies during the day. Between 1000 and 1900 LST, the DRA_{max} values are positive for all but one storm that propagates from the southeast around noon (Fig. 3.9 (a)). The magnitude of daytime anomalies is also much higher compared to nighttime increase (Table 3.3), suggesting that a bay breeze effect may be contributing. Thus, it is not clear whether the UHI or the bay breeze is responsible for the rainfall anomalies observed downwind of DC. In their model simulations, Zhang et al. (2011) showed that under a southerly or southwesterly flow regime, the interaction between the urban boundary layer and bay breeze circulations can sustain increased vertical velocity downwind of the DC metropolitan region, thereby suggesting that both mechanisms may be important. In the next section, the relation between the UHI-induced atmospheric instability and enhanced downwind rainfall is further explored by investigating the role of low-level advecting winds.

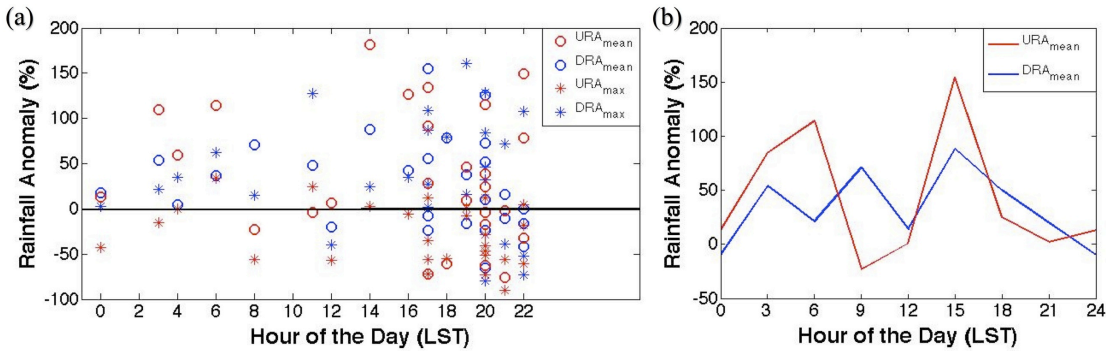

Figure 3.9 The diurnal pattern of rainfall anomaly associated with propagating storms over DC represented by (a) individual events, and (b) the 3-hour average anomaly computed from selected individual events. Note that the range of the Y-axis in (b) is intentionally smaller to emphasize on the bimodal peak of the diurnal rainfall anomaly distribution.

Table 3.3 The mean urban and downwind rainfall anomaly (%) and standard deviation observed during afternoon (1300 to 1700 LST) and nocturnal (2300 to 0800 LST) periods over DC. The p-value is mentioned for a significantly positive increase in the mean rainfall anomaly (≤ 0.1).

Anomaly	Mean Rainfall Anomaly (%)	Standard Deviation	p-value
Afternoon			
URA_{mean}	81.8333	91.0613	0.05
DRA_{mean}	51.5	65.4148	0.1
URA_{max}	-25.6667	34.0039	-
DRA_{max}	47.3333	41.3312	0.025
Night			
URA_{mean}	54.60	59.9358	0.1
DRA_{mean}	37	26.5989	0.025
URA_{max}	-16	35.6581	-
DRA_{max}	27.40	22.5455	0.05

3.3.1.3 Relation between UHI and the downwind rainfall anomaly

The destabilizing processes within the urban planetary boundary layer, responsible for modifying daytime convective precipitation, are well-known (discussed in section Chapter 1, section 1.2.2). In this section, I investigate whether the

downwind rainfall anomalies observed in the present study indeed result from the downstream advection of the urban PBL instability. This is carried out by exploring the relation between positive DRA_{max} events and the low-level advecting winds computed using NARR data. First, the line joining the urban center and the area of maximum precipitation ($P > 0.5*P_{max}$) in the downwind impact region is identified as the downwind propagation axis (see Fig. 3.10). Assuming that the instability (for e.g., the UHI-perturbed PBL circulation) will occur in the lower atmospheric levels, the mean advecting low-level (1000 to 700 hPa) wind vector is calculated over the urban region at the hour prior to the observed downwind rainfall maxima. The direction of this mean wind vector does not always coincide with the downwind storm propagation axis (Fig. 3.10). Depending on the nature of each individual storm, the steering winds can be considerably different from the mean low-level wind vector (for example, storms that occur in a high wind shear environment or surface storms that are propagated by an upper-level disturbance). The angle between the low-level mean wind vector and the downwind propagation axis (shown in Fig. 3.10) is referred to as the "wind deviation angle". If this angle exceeds 90°, then the advection from the urban area is considered to be zero.

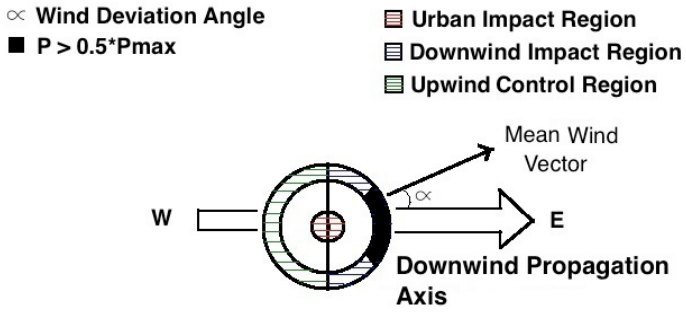

Figure 3.10 Same as Fig. 3.3 but depicting the downwind propagation axis determined based on the region of maximum precipitation in the downwind impact region (shaded in black). The mean low-level (1000-700 mb) wind vector and its deviation from the downwind propagation axis (α) are also shown.

Figure 3.11 (a) shows that the positive DRA_{max} events over Minneapolis are negatively correlated with the wind deviation angle, suggesting that the downwind rainfall intensification is more pronounced when the low-level urban instability is advected downstream. Additionally, a positive correlation is found to exist between the mean advecting wind speed and the DRA_{max} values (see Fig. 3.11 (b)). (Note that a projection of the mean wind vector on to the downwind propagation axis is used to compute the mean advecting wind speed). Since the downwind advection of the UHI-perturbed boundary layer instability is typically a daytime phenomenon, it is worth inspecting the correlation for nighttime and daytime events separately. In Fig. 3.11, the events occurring during nighttime (2300 to 0800 LST) are indicated by blue '**x**' signs. It is seen that the correlation with the mean wind vector may exist for both nocturnal and other events.

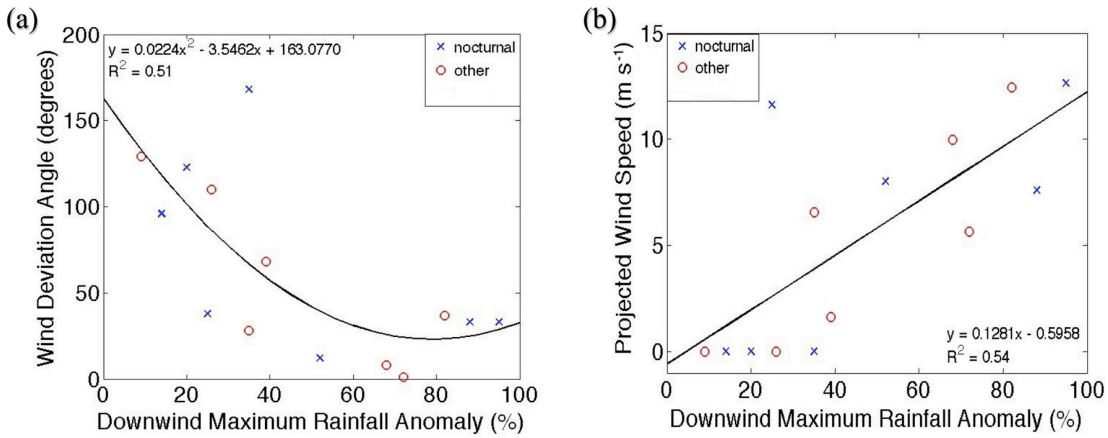

Figure 3.11 The relation between the positive downwind maximum rainfall anomaly (DRA_{max}) and (a) wind deviation angle, (b) projected wind speed, for storms propagating through Minneapolis. Storms that occur between 2300 to 0800 LST are considered as nocturnal events. Linear and non-linear relationships are derived using the least squares method of curve-fitting. R^2 represents the coefficient of multiple determination for the observed relationship.

For DC, a similar but rather weak correlation is found to exist between the low-level mean wind vector and the positive DRA_{max} anomalies (not shown). As discussed in the previous subsection (3.3.1.2), in addition to the UHI, daytime storms propagating through DC may be influenced by the bay breeze convergence effect. The correlation is therefore explored for all events occurring between 1000 and 1900 LST, during which the daytime bay breeze is likely to be active. The DRA_{max} values are negatively correlated with the wind deviation angle and positively correlated with the projected wind speed (Fig. 3.12 (a)). Therefore, although bay breeze effects may favor convergence, it appears that the UHI plays a major role in the downwind rainfall enhancement during this period. For nighttime events, a similar relationship with the mean wind vector is observed (Fig. 3.12 (b)) but the statistical significance is lower, likely due to the smaller sample size. For the rest of the events (occurring between 2000 to 2200 LST), no significant relationship is observed (Figure 3.12 (c)), confirming that the UHI's influence may be dominant only during select hours of the day. Note that in Fig. 3.12, the DRA_{max} values are higher for daytime events as compared to nighttime storms indicating that a UHI-bay breeze interaction may produce more significant rainfall anomalies. They are also more negative between 2000 to 2200 hours when the UHI-perturbed boundary layer circulation is not expected to be strong.

Thus, it appears that the UHI (nocturnal) or the UHI-induced PBL perturbation (daytime) can have a significant impact on precipitation associated with storms propagating through Minneapolis and DC. The rainfall anomalies over coastal cities

do not demonstrate such a clear UHI impact. Some characteristics of the anomalies observed for these cities are discussed in the next subsection.

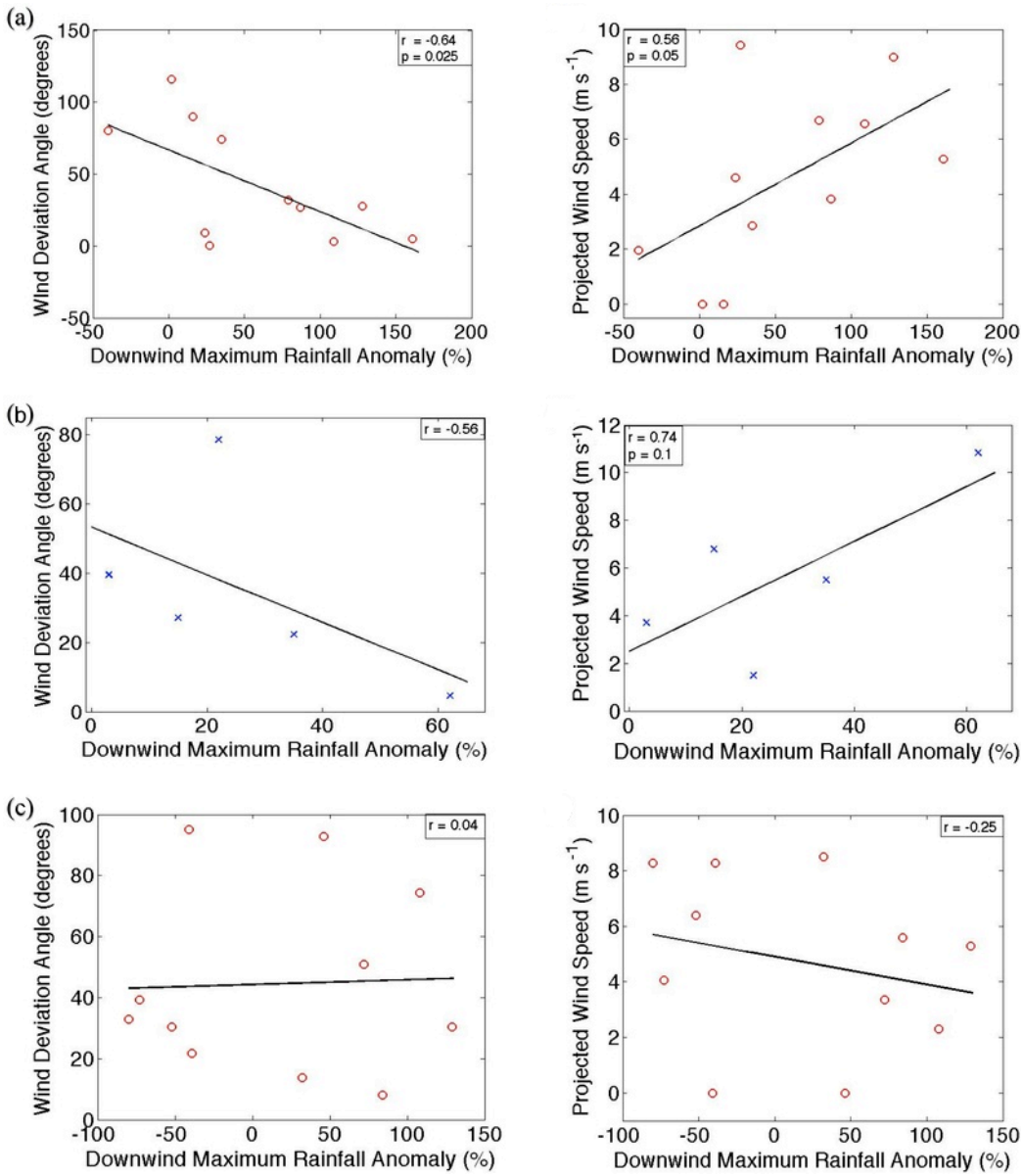

Figure 3.12 The correlation of wind deviation angle (left panel) and projected wind speed (right panel) with the downwind maximum rainfall anomaly (DRA_{max}) for storms propagating through DC occurring between (a) 1000 to 1900 LST, (b) 2300 to 0800 LST, and (c) 2000 to 2200 LST. The correlation coefficient is denoted by *r,* while the significance level (≤ 0.1) is denoted by *p*. Note that the range of the X-axis is dissimilar because the mechanisms that produce DRA_{max} values differ during the diurnal cycle (discussed in text).

3.3.1.4 Rainfall anomalies for coastal cities

Unlike Minneapolis and DC, the diurnal pattern of rainfall anomalies for Providence, NYC, and Cleveland do not show a clearly distinguishable UHI forcing. However, a statistically significant increase ($p = 0.05$) is observed in the URA_{mean} over NYC indicating that urban mechanisms may increase local rainfall over large coastal cities.

The outliers or extreme positive anomaly events ($\geq 75^{th}$ percentile) recorded over coastal cities may occur due to the local lake/sea breeze circulation but they are nevertheless inspected for the presence of a UHI-signature. First, the urban (and downwind) mean rainfall during such events is compared with the upwind mean rainfall from corresponding extreme events occurring in the upwind control region (identified using Eq. 3.5). The calculated mean rainfall is of comparable magnitude for the downwind and upwind regions, but is found to be 1.5 to 2 times higher for the urban region. This suggests that urban-related processes may enhance local mesoscale circulations to produce more extreme positive rainfall anomalies over coastal urban areas.

Coastal cities such as Boston, Tokyo, Chicago, and NYC, are known to experience local effects resulting from the interaction of the daytime sea breeze or lake breeze front with the UHI (Yoshikado and Kondo 1989; Barbato 1978; Keeler and Kristovich 2012). These fronts often slow down or stall over the urban area likely due to convergence induced by the UHI (Yoshikado and Kondo 1989; Keeler and Kristovich 2012; Kusaka et al. 2000). The inland propagation of such a front may be altered due to the UHI-enhanced land-sea temperature gradient (Barbato 1978;

Loughner et al. 2012). With the help of model analyses, one study showed that a strong sea breeze circulation is enhanced by the UHI to produce anomalously high convective precipitation in the vicinity of Sao Paulo, Brazil (Freitas et al. 2009). Shepherd and Burian (2003) observed positive anomalies in the climatological rainfall over and downwind of the coastal city of Houston that were mainly attributed to the interaction of the UHI with the local sea breeze circulation.

Fig. 3.13 shows that for Providence and Cleveland, a majority of the extreme anomalies occur between 1000 and 1800 LST. Moreover, positive anomalies are more pronounced during the late afternoon period for NYC and Cleveland. This hints at a possible interaction between the UHI and the daytime sea breeze front in producing more intense and frequent extreme positive anomaly events over coastal urban areas, and perhaps downwind.

The wind speed and wind deviation angle during events with extreme positive downwind rainfall anomalies ($DRA_{max} \geq 75^{th}$ percentile) are analyzed. For Cleveland, the two most positive DRA_{max} events are associated with projected wind speeds greater than 10 m/s and wind deviation angle less than 30°. However, no relation with low-level winds is found for Providence and NYC suggesting that the UHI impact on downwind rainfall may not be evident for these cities.

Additionally, the climatology of the mean low-level (1000-700 hPa) wind direction is compared for coastal versus inland cities by averaging for the years 2007-08. The wind direction is predominantly westerly to southwesterly, with no suggestive differences in the mean or the standard deviation. For coastal cities, a detailed

investigation of the UHI-sea breeze influence on propagating storms is beyond the scope of the present study and will be reported elsewhere.

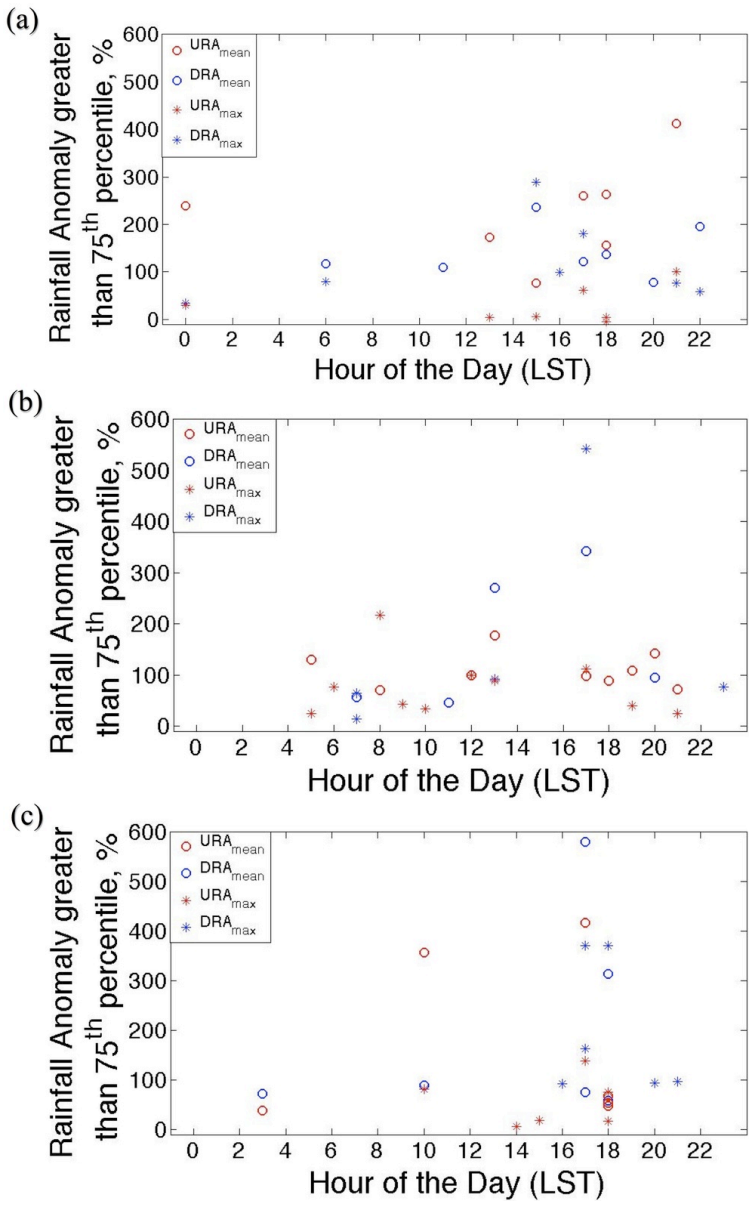

Figure 3.13 The diurnal pattern of extreme positive rainfall anomalies ($\geq 75^{th}$ percentile) associated with propagating storms over (a) Providence, (b) NYC, and (c) Cleveland.

3.3.1.5 Nocturnal Instability

In the present study, it is found that both nocturnal and afternoon rainfall anomaly can be significant for inland cities (Tables 3.2-3.3). The nocturnal instability, though, has not been investigated in detail in the past. In this section, I propose a hypothesis for the urban nocturnal PBL instability and the associated downwind rainfall maxima.

Although the UHI-perturbed PBL circulation is strongest during the afternoon, the UHI itself peaks at night. Thus, it is likely that the nocturnal PBL instability over the urban area is directly forced by increased surface temperature, and/or associated low-level thermodynamic instability within the stratified nighttime boundary layer. One hypothesis is that since net latent heat fluxes and associated urban-rural surface moisture differences are small during nighttime (Grimmond and Oke 1999b), the strong temperature anomaly (UHI) may drive positive differences in the surface equivalent potential temperature (θ_e) between the city and the rural environment. The prognostic applications of θ_e for convective precipitation are well known in the field of operational numerical forecasting (Campbell 1991; Smith 1993; Farina and DiStefano 1998). This important parameter is useful to predict regions of favored convection especially when synoptic scale forcing is at its minimum (Campbell 1991). High θ_e-values or θ_e-gradients in the lower atmosphere represent large instability (CAPE), and a lifting mechanism may favor convective development within such an area (Campbell 1991; Smith 1993). It is also observed that convective systems often propagate toward regions of low-level θ_e-*maxima*, and that positive θ_e-*advection* supports enhanced convection (Campbell 1991; Smith 1993). Therefore, it may be useful to understand

the impact of the urban land cover on surface θ_e-*values*, and its consequent influence on the development and enhancement of convective storms.

During METROMEX, the daytime surface θ_e-*values* over the urban area were examined to investigate the influence of ingesting dry, stable air in propagating storms (Ackerman et al. 1977). The daytime urban atmosphere was expected to be drier due to lower evapotranspiration, and it was speculated that the negative moisture anomaly may convert urban regions into a source of low surface θ_e air (Boatman and Auer 1974a,b). The spatial land use patterns in and around St. Louis, however, were not found to have a significant influence on the daytime surface θ_e values (Ackerman et al. 1977). It was thus concluded that the urban-enhanced rainfall in the downwind region was unrelated to a θ_e anomaly (Ackerman et al. 1977).

During nighttime, St. Louis was found to be more *moist* at the surface compared to the surrounding rural regions (Changnon et al. 1977; Ackerman et al. 1977). Ackerman et al. (1977) speculated that this is because the nocturnal surface air over the urban area does not lose its moisture due to condensation over vegetation (dew). Thus, a warm *and* moist surface atmospheric anomaly may exist over cities during the night, which may lead to increased equivalent potential temperature (θ_e) values within the nocturnal urban PBL. The presence of increased low-level θ_e gradients may contribute to the downwind intensification of rainfall through the advection of warm, moist unstable air.

In order to explore the above hypothesis, the surface temperature and dew point from the RTMA dataset are used to compute the hourly surface θ_e for each city, by assuming a standard atmospheric pressure of 1000 hPa. In Fig. 3.14, the diurnal

cycle of UHI (T_{urban}-T_{rural}), dew point difference ($DPT_{urban} - DPT_{rural}$) and the θ_e-*difference* ($\theta_{e\text{-}urban} - \theta_{e\text{-}rural}$) are plotted over 181 days (JJA, 2007-08).

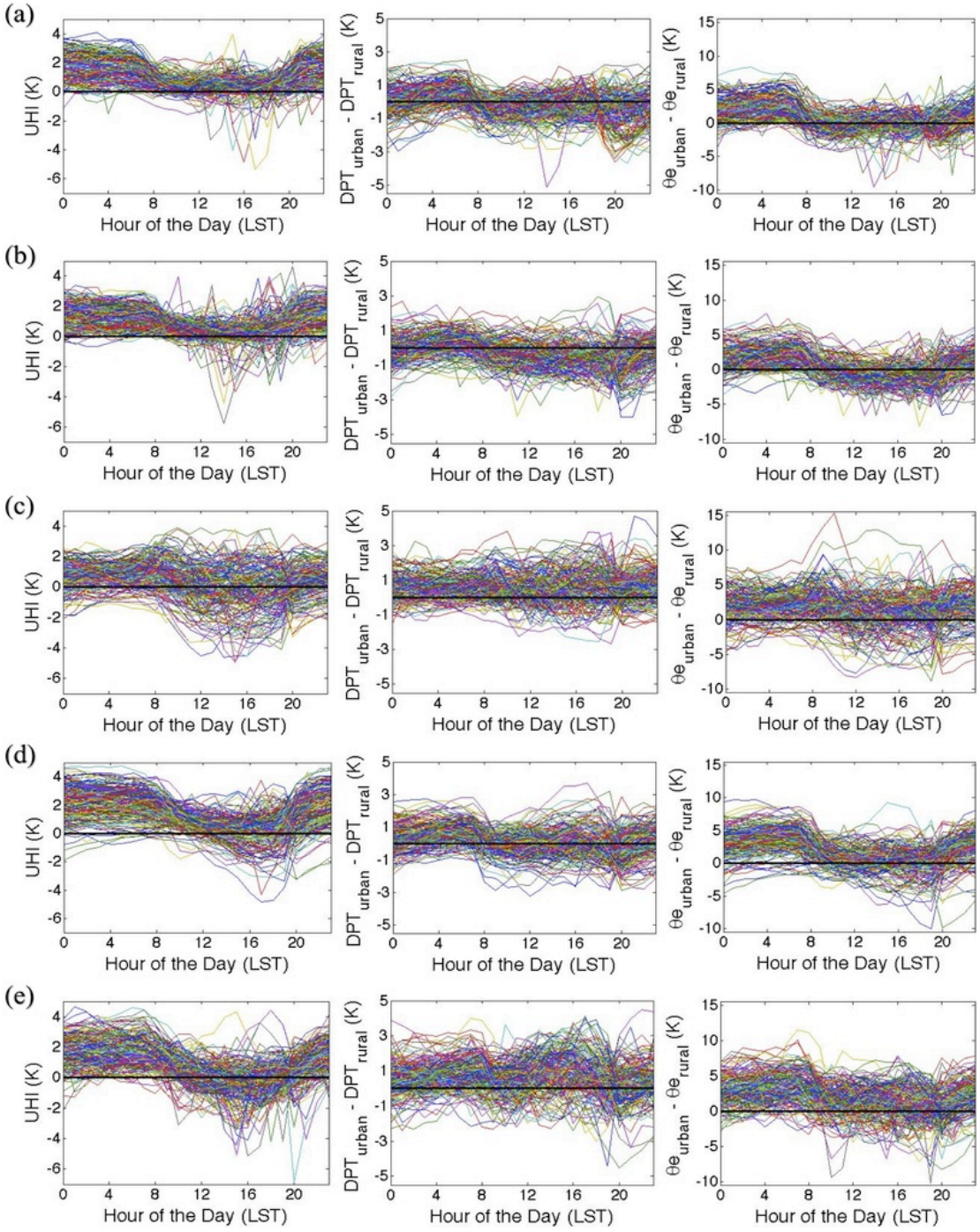

Figure 3.14 The diurnal cycle of differences in surface temperature (UHI; left panel), surface dew point temperature (center panel), and surface equivalent potential temperature (UHA; right panel) between the urban and the surrounding rural environment for (a) Minneapolis, (b) DC, (c) Providence, (d) NYC, and (e) Cleveland.

For all cities, the left panels of Fig. 3.14 show that the UHI is more robust during nighttime, as expected. The center panels of Fig. 3.14 indicate that the nocturnal dew point differences are also more positive and less variable as compared to the daytime differences for all cities (barring Cleveland, which mostly has positive differences throughout the day). As a result, the θ_e-*difference* between the urban and rural environment remains largely positive during nocturnal hours (0000 to 0700 LST) (see right panels of Fig. 3.14). During daytime, the UHI, the dew point difference as well as the θ_e-*difference* are found to be not robust for Providence, NYC, and Cleveland. Minneapolis and DC are more likely to experience a daytime UHI, however, the θ_e-*difference* is much more variable over these cities. This is because reduced latent heat fluxes during the day may easily counter the θ_e-*increase* resulting from UHI in the urban environment. These cities thus experience a warm but dry anomaly during daytime due to the presence of urban land cover, causing θ_e-values to be more variable. On the other hand, the nighttime increase in temperature over the urban area is often accompanied by an increase in the dew point, likely due to the small but positive latent heat flux differences at night. Therefore, much warmer and less dry conditions are observed over all cities during nighttime, which leads to a positive surface θ_e anomaly.

It thus appears that urbanization not only causes anomalous warming (UHI) but may also produce anomalously high surface equivalent potential temperature (θ_e) in the nocturnal atmosphere. This surface instability may be referred to as the urban hygrothermal anomaly (UHA). For the cities considered in this study, the UHA appears to be a prominent and robust feature that is comparable to the nocturnal UHI.

Future studies are needed to investigate in detail the influence of the urban land cover in inhibiting dew formation thus contributing to positive θ_e anomalies during nighttime. Moreover, if the UHA indeed introduces thermodynamic instability in the nocturnal urban atmosphere, then its role in producing anomalous urban and downwind nocturnal rainfall needs to be investigated for propagating as well as non-propagating storms.

3.3.2 The UHI impact on non-propagating storms

Prior to investigating the UHI impact on stationary or non-propagating storms, the upwind and downwind regions are identified for Dallas and Houston. In previous studies, several approaches were taken to determine the direction of steering winds or the climatological storm movement (Shepherd et al. 2002; Shepherd and Burian 2003; Westcott 1995; Huff and Changnon 1972, 1973; Ashley et al. 2012). As discussed earlier (in subsection 3.3.1.3), it appears that the 1000-700 hPa advecting winds are more important for the downstream propagation of the urban instability than the steering flow. Therefore, in this study, I compute the climatological low-level (1000-700 hPa) advecting winds from NARR (JJA; 2007-08) in order to identify the downwind direction and the impact region. Previous studies estimated the mean warm season 700 hPa flow to be from 225° for Dallas (Shepherd et al. 2002), and from 178° for Houston (Shepherd and Burian 2003). Here, it is found that the mean low-level advecting winds are from 160° for Dallas and 168° for Houston. Both upwind and downwind regions are selected to encompass a 150° sector centered around the mean wind vector. This value is chosen to incorporate the standard deviation of the mean wind direction (similar to the methodology adopted by Shepherd and Burian (2003)).

The seasonal accumulated rainfall for Dallas and Houston, along with the climatological downwind vector is shown in Fig. 3.15. Dallas experiences increased rainfall totals in the downwind direction within the rural ring, whereas Houston has higher amounts over the urban region. Note that Houston also has higher rainfall in the upwind region compared to downwind, which appears to be related to the sea breeze convergence effect along the coastline.

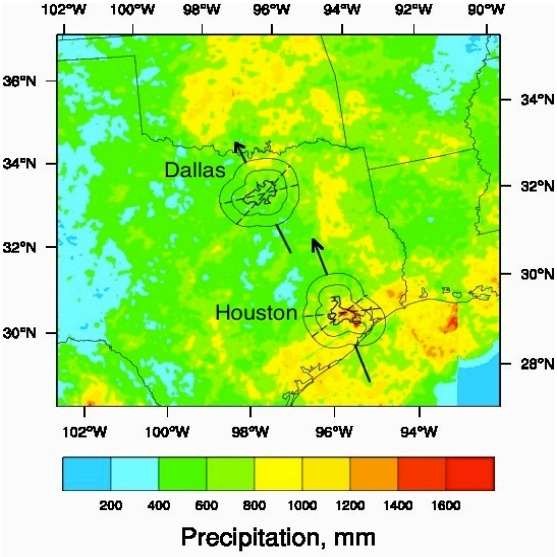

Figure 3.15 Seasonal accumulated precipitation (JJA; 2007-08) over Dallas and Houston along with the climatological mean downwind direction (bold arrow) calculated from the low-level (1000-700 hPa) winds. The bold solid line is used to represent each city polygon, the thin solid lines represent the surrounding rural ring. The dotted lines represent the 150° sector centered around the mean wind vector defining the boundaries for upwind and downwind regions. The mean wind vector is from 160° for Dallas and 168° for Houston.

In order to inspect the characteristics of the downwind rainfall anomaly over Dallas, precipitation recorded on non-propagating storm days is binned into hourly intervals. The diurnal cycle (3-hr running average) in the frequency of rainfall occurrence is shown in Fig. 3.16 (a). Although rainfall frequency peaks during daytime, there is a tendency for increased nighttime events in the downwind region compared to the

upwind. The mean hourly rainfall rates between the upwind and downwind regions are found to be comparable; however, heavy events or outliers are more pronounced during night to early morning hours in the downwind region (see Fig. 3.16 (b)). This suggests that rainfall initiation and intensification may be favored in the region downwind of Dallas during nocturnal hours, which may be related to the urban instability. The right panel of Fig. 3.17 shows that the nocturnal UHA, described in section 3.3.1.5, exists over this city as well as over Houston.

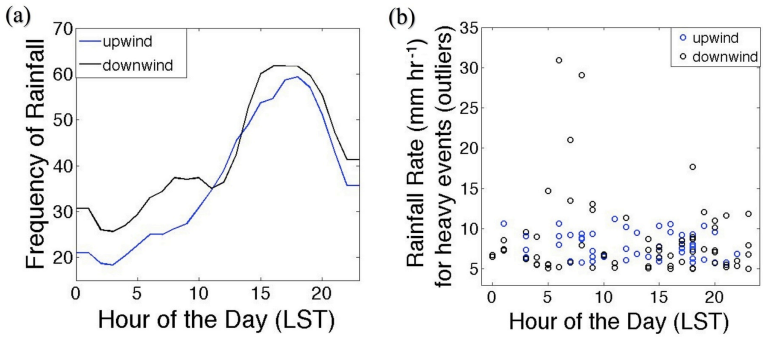

Figure 3.16 The diurnal cycle of (a) rainfall frequency (events), and (b) hourly rainfall rate associated with heavy events (outliers) observed in the upwind and downwind regions of Dallas. Outliers are data points that exceed the third quartile (75th percentile) by a distance greater than 1.5 times the interquartile range.

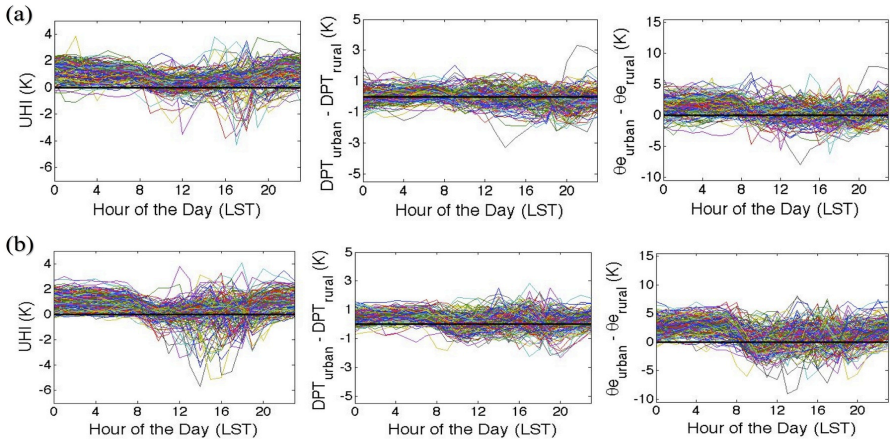

Figure 3.17 The diurnal cycle of differences in surface temperature (UHI; left panel), surface dew point temperature (center panel), and surface equivalent potential temperature (UHA; right panel) between the urban and the surrounding rural environment for (a) Dallas, and (b) Houston.

For Houston, a similar analysis of hourly rainfall frequency between upwind and urban regions suggests that there is a phase lag in the diurnal cycle (Fig. 3.18 (a)). This may be expected due to the relative distance from the coast and consequent lag in the occurrence of rain-producing sea breezes. The outliers or heavy rainfall rates over the urban and upwind regions are comparable in intensity (Fig. 3.18 (b)), however, they tend to occur more frequently during the afternoon period over the urban region (Fig. 3.18 (c)). This suggests that the interaction of the UHI with the daytime sea breeze circulation may increase the frequency of heavy rainfall events over urban Houston. This result agrees in part with Shepherd and Burian (2003) who proposed that the afternoon UHI-circulation and the sea breeze circulation could interact to produce increased warm season rainfall over and downwind of the Houston urban area. A downwind increase, however, is not observed in this study. A point worth noting is that the urban impacts discussed above for Dallas and Houston were observed during both years despite the fact that 2008 was a drought year in this region.

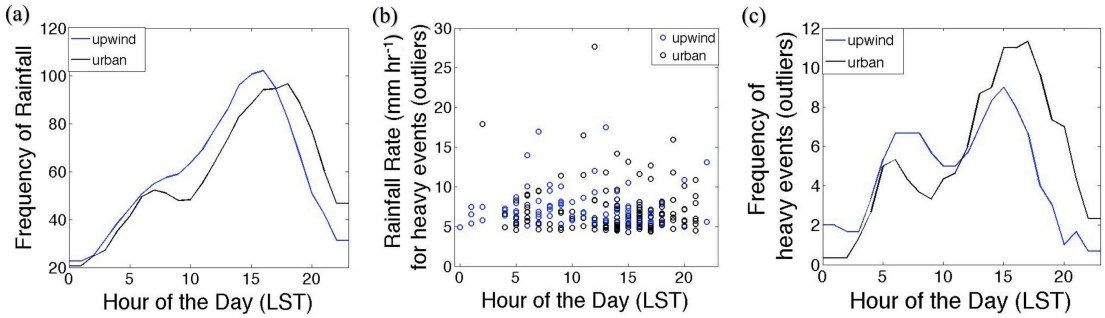

Figure 3.18 The diurnal cycle of (a) rainfall frequency (events), (b) hourly rainfall rate associated with heavy events (outliers), and (c) frequency of heavy events (outliers) observed in the upwind and urban regions of Houston. Outliers are data points that exceed the third quartile (75th percentile) by a distance greater than 1.5 times the interquartile range.

3.4 Conclusions

The aim of this study was to investigate the UHI impact on warm season rainfall using contemporary high-resolution observations over several US cities, and to explore its variability. Recent studies have used similar datasets in the southeast US to study the UHI-influence on thunderstorm development during synoptically benign days (Dixon and Mote 2003, Bentley et al. 2010, Ashley et al. 2012). In the present study, a UHI-induced rainfall increase is observed for stationary storms in the southern US, and similarly for propagating storms associated with fronts, low-pressure systems, troughs, outflow boundaries and squall lines, observed in other parts of the country. The results are compared with earlier literature (METROMEX; Changnon et al. 1977; Ackerman et al. 1977; Huff and Changnon 1972, 1973; Westcott 1995) that analyzed a similar UHI-effect for propagating storms. The outcome of this study suggests that it is useful to consider rainfall anomalies by tracking each individual propagating storm, apart from collectively studying the climatological rainfall patterns based on the most frequent wind direction as was done in the past (Shepherd et al. 2002; Shepherd and Burian 2003; Westcott 1995; Huff and Changnon 1972, 1973; Ashley et al. 2012). Using a diurnal trend analysis, it is found that the UHI is the dominant mechanism for rainfall increase over and downwind of inland cities, whereas the UHI-sea breeze interaction may produce significantly enhanced precipitation over coastal urban areas.

For the inland cities of Minneapolis and DC, the UHI-induced thermal forcing is clearly visible in the diurnal pattern of rainfall anomalies. A bimodal evolution with distinct peaks occurring during night and afternoon hours is observed over the urban as well as downwind regions. METROMEX found a similar double peak in the region

downwind of St. Louis, however, only a late afternoon rainfall maximum was reported over the urban region (Changnon et al. 1977). As a result, the mechanistic processes responsible for the daytime rainfall anomaly (UHI-perturbed boundary layer circulation) have been studied in detail, but the nighttime peak has received less attention in the past. The present study shows that the nocturnal anomaly associated with propagating storms can be as significant as the daytime rainfall increase for inland cities. Moreover, propagating storms appear to be steered towards the urban centers likely due to UHI-induced convergence, thereby increasing the urban mean rainfall. But the storm intensification occurs in the peripheral or the downwind impact region due to the advection of the urban instability, as indicated by the significantly positive downwind maximum rainfall anomalies (DRA_{max}). This result agrees with METROMEX observations, which demonstrated that the most significant urban impact over St. Louis was observed in the downstream stimulation of propagating storms (Changnon et al. 1977; Ackerman et al. 1977).

For coastal cities, propagating storms typically experienced more pronounced spatial rainfall anomalies likely because of the local mesoscale variability due to sea breeze or lake breeze fronts. The UHI appears to interact with the local mesoscale circulation leading to more extreme and frequent positive rainfall anomalies over the urban region during daytime. A number of modeling studies have simulated the interaction of the daytime sea breeze front with the UHI suggesting that the front propagation is often slower over the urban region (Kusaka et al. 2000; Yoshikado 1994; Ohashi and Kida 2002). Further studies are needed to decipher the urban and downwind precipitation enhancement due to such an interaction.

For non-propagating storms, the UHI's influence differs once again for an inland (Dallas) and a coastal (Houston) city. A positive nocturnal anomaly in the frequency and intensity of rainfall is observed downwind of Dallas. For Houston, a local daytime increase in the frequency of heavy or extreme positive anomaly events is observed.

In general, it appears that nocturnal and downwind UHI impacts are more visible for the inland cities of Minneapolis, DC, and Dallas. The precipitation anomalies over coastal urban areas on the other hand, are more significantly positive, likely due to UHI's interaction with the daytime sea breeze front. Future studies should consider these important differences for a complete understanding of the observed spatial rainfall anomalies.

An elementary investigation of the nocturnal instability suggests that in addition to the UHI, urban areas may experience anomalously high surface equivalent potential temperature due to less dry and warmer conditions during nighttime. This is termed as the Urban Hygrothermal Anomaly (UHA). If the UHA exists, then increased low-level θ_e-*gradients* and the downstream advection of positive θ_e may contribute to downwind rainfall enhancement in propagating nocturnal storms. Such an effect will be investigated using modeling studies in the future.

This study has laid the necessary groundwork for important urban related processes and their variability. Future studies will aim to investigate the nature and role of the nocturnal urban instability in rainfall modification, as well as the UHI-sea breeze interaction in producing more frequent and extreme daytime urban rainfall. Exploring and understanding the variability in the mechanisms for urban rainfall

enhancement is necessary for better forecasts, urban water resources management, flood disaster planning, and so on. In the next chapter, the impact of the urban land cover on nocturnal propagating storms over Minneapolis is investigated using model sensitivity analyses.

Chapter 4: A model-based study of the urban influence on nocturnal propagating storms over Minneapolis

Abstract

Two nocturnal propagating storms that occur over urban Minneapolis are simulated using the WRF model. Ensemble sensitivity simulations are carried out (by replacing developed land with surrounding croplands) to inspect the role of the urban land cover in producing anomalous nocturnal precipitation. In the sensitivity simulations, storm cells do not occur directly over the city, whereas the urban area in the control simulation behaves like a "hot spot" or favored location for propagating storm cells. Increased surface convergence due to the UHI, enhanced frictional drag, and a cyclonic turning of surface winds as the storm approaches, appear to introduce a low-pressure anomaly over the urban region thereby influencing the storm cell position. The ensemble simulation that shows the maximum urban influence on the storm cell location, also records the strongest UHI and the maximum surface convergence anomaly. Apart from the UHI, the enhanced frictional drag due to stronger wind speeds may contribute substantially to surface convergence on storm days. Future studies will aim to quantify the thermal and dynamical influence on the convergence field and the related rainfall anomaly.

While the UHI-perturbed boundary layer circulation does not appear to be active at night, the UHA (positive surface θ_e anomaly) may exist, leading to increased

θ_e values in the urban nocturnal PBL. Its contribution to nocturnal downwind rainfall intensification will be investigated in future studies.

4.1 Introduction

Urban areas introduce mesoscale atmospheric perturbations that may alter warm season precipitation either through the enhancement of existing storms or through the development of new convection (Changnon et al. 1977; Ackerman et al. 1977; Bornstein and LeRoy 1990; Dixon and Mote 2003). METROMEX and earlier studies found that the urban influence was mainly evident during propagating thunderstorms with moderate to heavy rainfall (Ackerman et al. 1977; Changnon and Huff 1986; Huff and Changnon 1973; Westcott 1995), but studies have also shown that the UHI may initiate new convection (Huff and Changnon 1973; Bornstein and LeRoy 1990; Bornstein and Lin 2000; Dixon and Mote 2003). The daytime perturbed PBL circulation with deeper mixing heights due to UHI-enhanced convergence is considered to be one of the main causes for the urban and downwind rainfall increase (Ackerman et al. 1977; Westcott 1995; Shepherd et al. 2002; Vukovich and Dunn 1978). There is also evidence that the enhanced mixing and stretching leads to more neutral (or unstable) lapse rates in the upper PBL which may strengthen cloud updrafts and enhance precipitation (Ackerman et al. 1977). A similar detailed mechanistic analysis, however, is lacking for the anomalous nocturnal downwind precipitation that was also observed during METROMEX. Changnon and Huff (1986), and Huff and Changnon (1973), observed a significant rainfall increase associated mainly with nocturnal propagating storms. Although this anomaly was not investigated, the

nocturnal UHI and the related surface convergence were speculated as the likely cause (Huff and Changnon 1973). More recently, Dixon and Mote (2003) studied the UHI impact on nocturnal thunderstorm development during calm conditions with low wind speeds. Since the UHI is typically strong during synoptically benign nights, an increased convergence is expected to occur over the urban area. The authors speculated that the UHI produces a low-pressure anomaly during such nights, thus resulting in a thermally driven circulation with air flowing from the surrounding rural areas into the city (Dixon and Mote 2003). Studies have observed similar thunderstorm development under calm conditions over New York City (Bornstein and LeRoy 1990) and Atlanta (Bornstein and Lin 2000). Propagating thunderstorms, however, are reportedly bifurcated around these cities producing maximum precipitation in the lateral edges and in the downwind region (Bornstein and LeRoy 1990; Bornstein and Lin 2000). This is attributed to the divergence caused by the building-barrier effect which appears to lead to a rainfall minimum over the urban area itself (Bornstein and LeRoy 1990). Thus, more recent studies point to a decrease in urban mean rainfall associated with propagating storms due to a divergence effect (Bornstein and LeRoy 1990; Bornstein and Lin 2000), contrary to a positive rainfall anomaly as was observed in the past (Ackerman et al. 1977; Huff and Changnon 1973; Changnon and Huff 1986).

Wong and Dirks (1978) studied the differences in airflow over an urban area during calm conditions (wind speed < 3.5 m s^{-1}) as well as under the influence of strong winds (wind speed > 3.5 m s^{-1}). During calm winds, they found an increase in urban wind speeds due to convergence of air from the surrounding rural regions. This

is consistent with recent studies reporting thunderstorm development under synoptically benign conditions (Bornstein and Lin 2000; Dixon and Mote 2003). For wind speeds greater than 3.5 m s^{-1}, a deceleration was observed as a result of the enhanced frictional drag due to increased surface roughness and vertical mixing height over the city (Wong and Dirks 1978). Despite frictional retardation, surface convergence was found to occur because of the UHI (Wong and Dirks 1978). The authors, in fact, argue that the UHI-induced convergence is aided by the frictional drag, which is consistent with METROMEX observations that reported a similar effect in the daytime boundary layer (Ackerman et al. 1977).

Thus, opposing effects that include dynamical divergence (building-barrier effect) and enhanced convergence (due to UHI and frictional dampening) have been associated with propagating thunderstorms over urban regions. In the previous chapter, an increase in urban mean rainfall was observed for storms occurring over the inland cities of Minneapolis and Washington D.C., during night as well as afternoon hours. This suggests that the UHI and related convergence is the dominant factor influencing rainfall over these cities. In this Chapter, I investigate if such an increase is also evident in model simulations. Two propagating storm events occurring during the nighttime over urban Minneapolis are simulated. The urban impact is investigated using land cover sensitivity experiments, and the role of thermal and dynamical convergence (divergence) is examined. Moreover, since a downwind intensification of rainfall was also observed in the previous chapter, the presence of a PBL instability in the urban nocturnal atmosphere (for example, increased θ_e values caused by the UHA) is also explored.

4.2 Methods

4.2.1 Model Configuration

The WRF model is used to carry out high-resolution (0.5 km) urban land cover sensitivity simulations over the Minneapolis-St. Paul region. The domain and nesting configuration is shown in Figure 4.1. The North American Regional Reanalyses (NARR) data are used as initial and boundary forcing conditions. The model's vertical resolution consists of 45 levels in the terrain-following sigma coordinate system, with eight levels in the lowest 1 km and the remaining equally spaced up to 100 hPa.

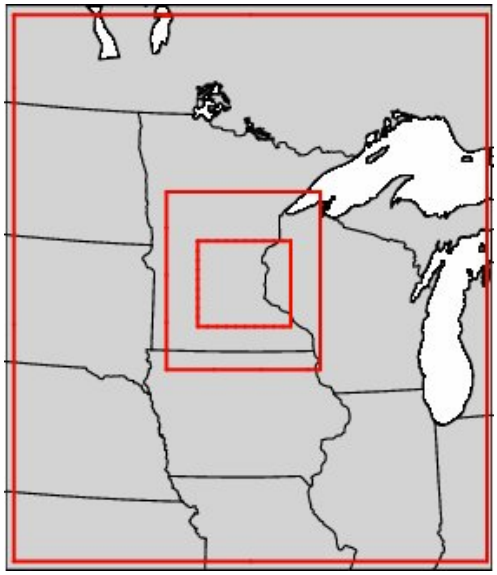

Figure 4.1 The one-way nesting configuration of the model. Red solid lines represent the location of the outermost grid (12.5 km resolution), middle grid (2.5 km resolution) and the innermost grid (0.5 km resolution) over the Minneapolis-St. Paul region. All analyses are performed over the innermost grid.

The unified Noah Land Surface Model (LSM; Chen and Dudhia 2001) is used for predicting heat and moisture fluxes from the surface to the atmosphere. The Mellor-Yamada-Janjic (MYJ) scheme (Mellor and Yamada 1982) is selected for boundary

layer and vertical diffusion processes while the Eta surface-layer scheme (Monin and Obukhov 1954) is used to represent surface fluxes. The WRF Single-Moment 5-class (WSM5) scheme (Hong et al. 2004; Hong and Lim 2006) is chosen for representing the microphysics. The Kain-Fritsch (KF) convective scheme (Kain 2004) is activated at 12.5 km resolution, while convection is resolved explicitly at 2.5 km and 0.5 km resolutions.

4.2.2 Urban physics in WRF model

In the WRF model, it is possible to simulate turbulent heat and momentum fluxes as well as other urban effects over developed land surfaces by coupling an urban canopy model with the Noah LSM. For this purpose, the performance of the Building Energy Parameterization (BEP) scheme (Martilli et al. 2002) and the Urban Canopy Model (UCM; Kusaka et al. 2001; Kusaka and Kimura 2004; Chen et al. 2006) is evaluated by comparing the simulated skin temperature with observations from the Moderate Resolution Imaging Spectroradiometer (MODIS). The single-layer UCM assumes that building heights in the urban canopy do not extend beyond the lowest model level. The multi-layer BEP scheme, on the other hand, recognizes a three-dimensional (vertical) distribution of urban surfaces (such as walls, roofs) while calculating sources and sinks of heat, moisture and momentum in the urban canopy (Schubert 2010). The MODIS skin temperature is derived from the split window algorithm developed by Wan and Dozier (1996). It is found that the nighttime skin temperature increase over Minneapolis is captured reasonably well by both schemes, but the observed daytime skin temperature anomaly is not adequately simulated by the

UCM. Therefore, the BEP scheme is chosen to represent urban physics in the model simulations. Moreover, the skin temperature anomaly pattern is improved when the MODIS-derived urban land cover used in WRF is spatially augmented with developed land cover (≥ 20% ISA) from the more recent NLCD (2006) dataset. Figure 4.2 compares against MODIS observations, the model simulated skin temperature with and without such augmentation. The skin temperature UHI, especially in the northwestern part of the urban region, is better represented in Fig. 4.2 (c). Therefore, the land cover augmentation is performed prior to running the model simulations.

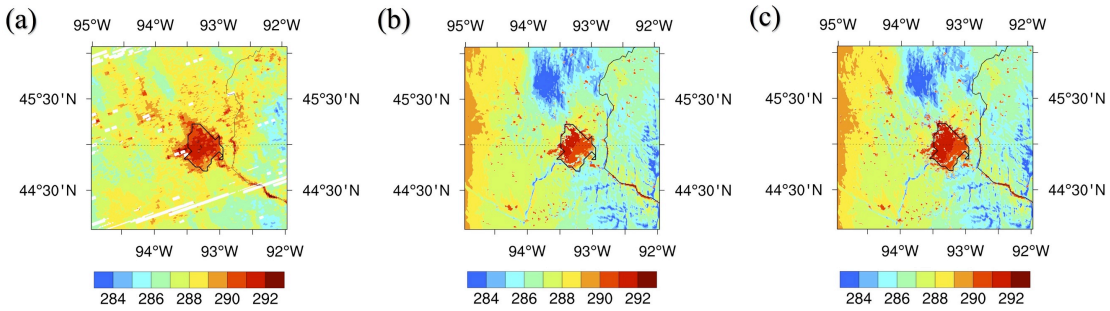

Figure 4.2 The surface skin temperature (K) at around 2200 LST on Aug 26, 2008, over Minneapolis, derived from (a) satellite observations (MODIS), (b) BEP simulation using WRF urban land cover, and (c) BEP simulation using WRF urban land cover augmented with NLCD data.

4.2.3 Experimental Design

Two nocturnal propagating storms occurring over Minneapolis are selected from the warm season (JJA) period of 2007-2008. The UHI-impact on propagating storms observed during this period has been discussed in the previous chapter. It is expected that model analyses of surface variables will help identify some urban mechanisms leading to the nocturnal rainfall increase, if observed. For each case, the

control experiment consists of the original as well as two ensemble member simulations (E1 and E2). The ensembles are created by introducing random perturbations of 2 °K to the initial surface air and skin temperature obtained from NARR. The 10-m horizontal winds are also perturbed by a small magnitude (0.5 ms^{-1}). Corresponding sensitivity simulations (original and ensemble) are performed by replacing the developed urban surface with the surrounding dominant land cover type (croplands). Note that a relatively high value (2 °K) is selected for temperature perturbation while creating ensembles because this is the average magnitude of the UHI (temperature difference between control and sensitivity experiments) expected due to land cover replacement over the urban region.

Model simulations are run for a period of four and a half days considering a spin-up time of 17 hours, and allowing a lead time of 50 and 54 hours for the first and second events, respectively. This allows an investigation of the urban instability not only during the rainfall event but also one day before and one day after the occurrence of the storm. The Stage IV precipitation data are used to evaluate differences in simulated precipitation between control and sensitivity experiments. The model results are discussed in the following section.

4.3 Results

4.3.1 Sensitivity of nocturnal precipitation to urban land cover

The first simulated event is an eastward propagating squall line that passes through the urban area between 2100 to 0200 LST on 27-28 August, 2008.

Observations indicate that a storm cell occurs over urban Minneapolis producing enhanced precipitation downwind of the city (see left panel of Fig. 4.3 (a)). In general, the model overestimates rainfall associated with this event and the simulated urban mean precipitation is higher than observed (Fig. 4.4 (a)). The spatial precipitation features such as the proximity of the storm cell to the urban area appear to be better represented in the control simulation (center panel of Fig. 4.3 (a)). The downwind rainfall intensification, however, is not captured by the model. In the sensitivity simulation without urban land cover, the storm cell does not occur over Minneapolis, but is constrained to the region upwind of the city (right panel of Fig. 4.3 (a)).

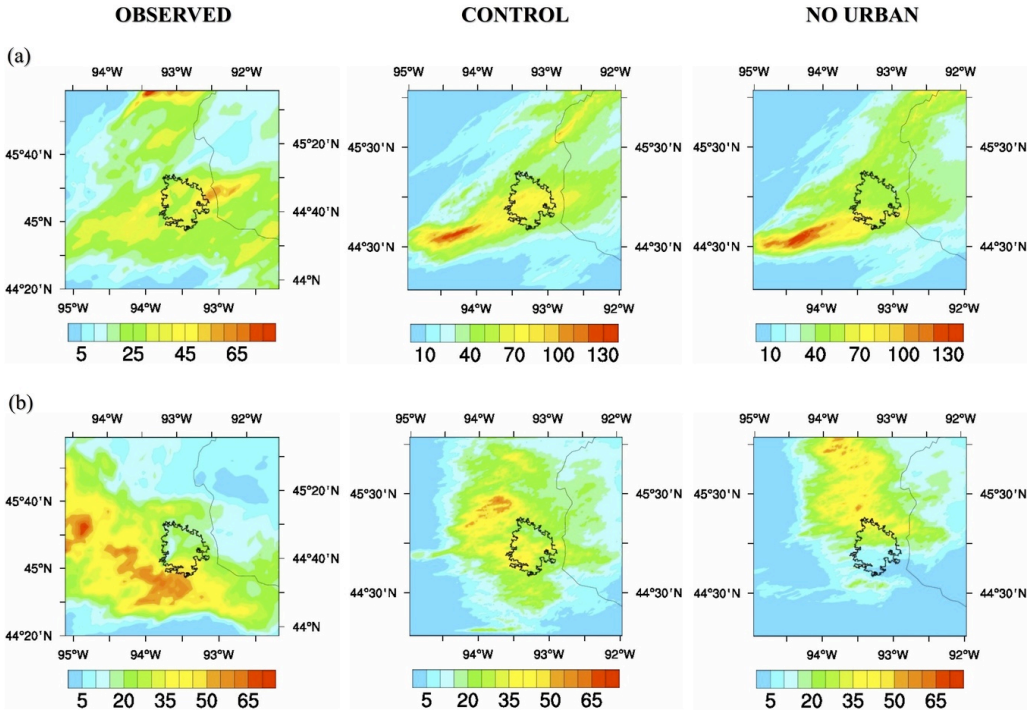

Figure 4.3 The total rainfall accumulation (mm) over the study domain from Stage IV observations (left), the control ensemble mean (center), and the sensitivity ensemble mean (right) for propagating storms occurring between (a) 2100 to 0200 LST on 27-28 August, 2008, and (b) 0100 and 0600 LST on 11 August, 2007.

The second event is a southeast propagating nocturnal outflow boundary that occurred between 0100 and 0600 LST on 11 August, 2007. An increase in precipitation is observed in the peripheral region southwest of the city (left panel of Fig. 4.3 (b)). Once again, the spatial characteristics, such as enhanced precipitation to the south and southwest of the city, are better reproduced by the control simulation (center panel of Fig. 4.3 (b)). In the sensitivity simulation, little precipitation is produced over and downwind of Minneapolis as the storm propagates through the region (right panel of Fig. 4.3 (b), and 4.4 (b)). Thus, it appears that the city of Minneapolis experiences a positive rainfall anomaly during both nocturnal propagating storms due to the presence of urban land cover. The role of the UHI and enhanced convergence, as well as other urban instability, is investigated in following subsections.

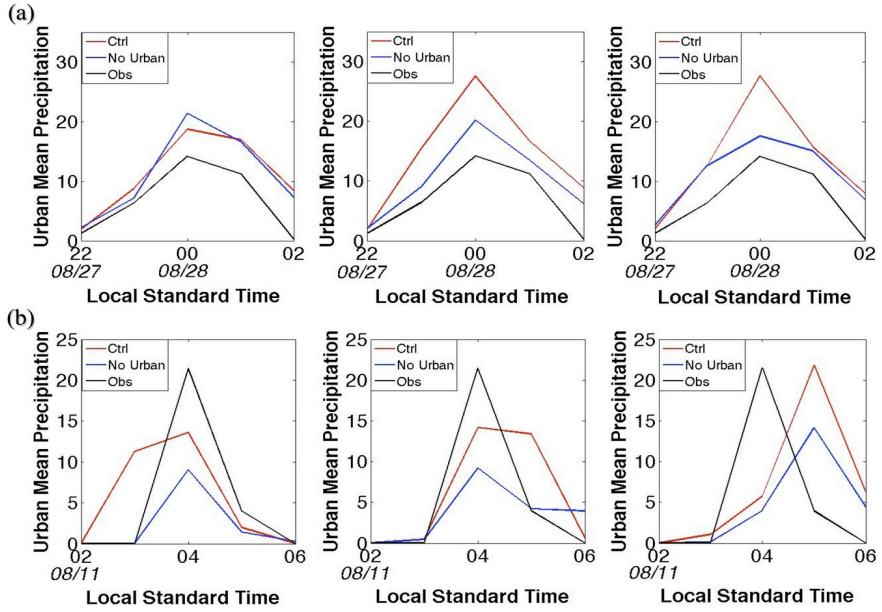

Figure 4.4 The temporal evolution of the hourly accumulated urban mean rainfall from (a) 2200 to 0200 LST on 27-28 August, 2008, and (b) 0200 and 0600 LST on 11 August, 2007, for the original (left panel), first ensemble or E1 (center panel), and second ensemble or E2 (right panel) simulations. The mean urban rainfall from Stage IV observations (black), control (red) and sensitivity (blue) simulations are shown.

4.3.2 Improvement in spatial precipitation features

In order to quantify the improved representation of the squall line and outflow boundary, the spatial rainfall field for each control and sensitivity ensemble pair is compared against observations using the Method for Object-based Diagnostic Evaluation (MODE). This features-based method is useful to evaluate the spatial characteristics of storm cells (objects). Davis et al. (2009) successfully demonstrated the use of this method to compare model rainfall accumulations against observations. The MODE software is obtained from the Development Testbed Center's Model Evaluation Tool (MET version 2.0) verification package (2009).

First, the 5-hr accumulated precipitation (shown in Fig. 4.3 (a) and 4.3 (b)) is interpolated on to NCEP's grid 227 (5 km resolution) using the budget interpolation method (Accadia et al. 2003). Storm cells (or objects) in the forecast and observation fields are identified using a convolution filter and a suitable rainfall threshold. (The rainfall threshold for each field is calculated by multiplying the maximum precipitation amount by a factor of 0.3). The objects in both fields are then matched by comparing several attributes (α), viz., position (centroid distance), orientation (angle difference), spatial extent (area ratio), and spatial overlap (intersection area). Note that each object attribute is calculated using simple measures such as the number of grid points occupied, moments, etc. An interest value (I; ranging from 0 to 1) is assigned for each attribute to quantify the similarity between the matched object pairs. For example, I has a maximum value of 1 for small centroid distance whereas a minimum value of 0 for small spatial overlap (or intersection area) between the forecast and the observed object pair. Finally, a total interest value (T) is computed for the identified

object pair using Eq. 4.1, where the subscript *i* denotes the various attributes considered, *w* is the weight assigned to each attribute, and *C* is the confidence level calculated for the attribute vector. (Note that *C* is calculated for the centroid distance and angle difference attributes only, in order to express the uncertainty involved while comparing small, round objects with large, angular ones).

$$T = \frac{\sum_i w_i C I_i(\alpha_i)}{\sum_i w_i C}. \tag{4.1}$$

In Eq. 4.1, the weight assigned to the centroid distance, angle difference, and intersection area attributes is 2, while *w=1* is used for the area ratio attribute.

Figure 4.5 demonstrates the matched object pairs (in red and green) for the squall line event (unmatched objects are shaded in blue). Since this study is primarily focused on the rainfall across urban Minneapolis, a comparison is made only for the storm cell that occurs over the city (red object in Fig. 4.5). Differences in the spatial extent and location of the storm cell are observed between the control and sensitivity simulations. Due to the presence of the urban land cover in the control simulation, the cell extends eastward, over and downwind of Minneapolis. In the original sensitivity run (Fig. 4.5 (c)), the storm cell has a southwest-northeast tilt as opposed to a west-east orientation that is observed (Fig. 4.5 (a)). The ensemble members (E1 and E2) of the sensitivity simulation produce a more accurate representation of the orientation, but the eastward propagation of the storm is constrained (Fig. 4.5 (e) and (g)). The spatial overlap and the centroid position are better simulated by the control ensemble

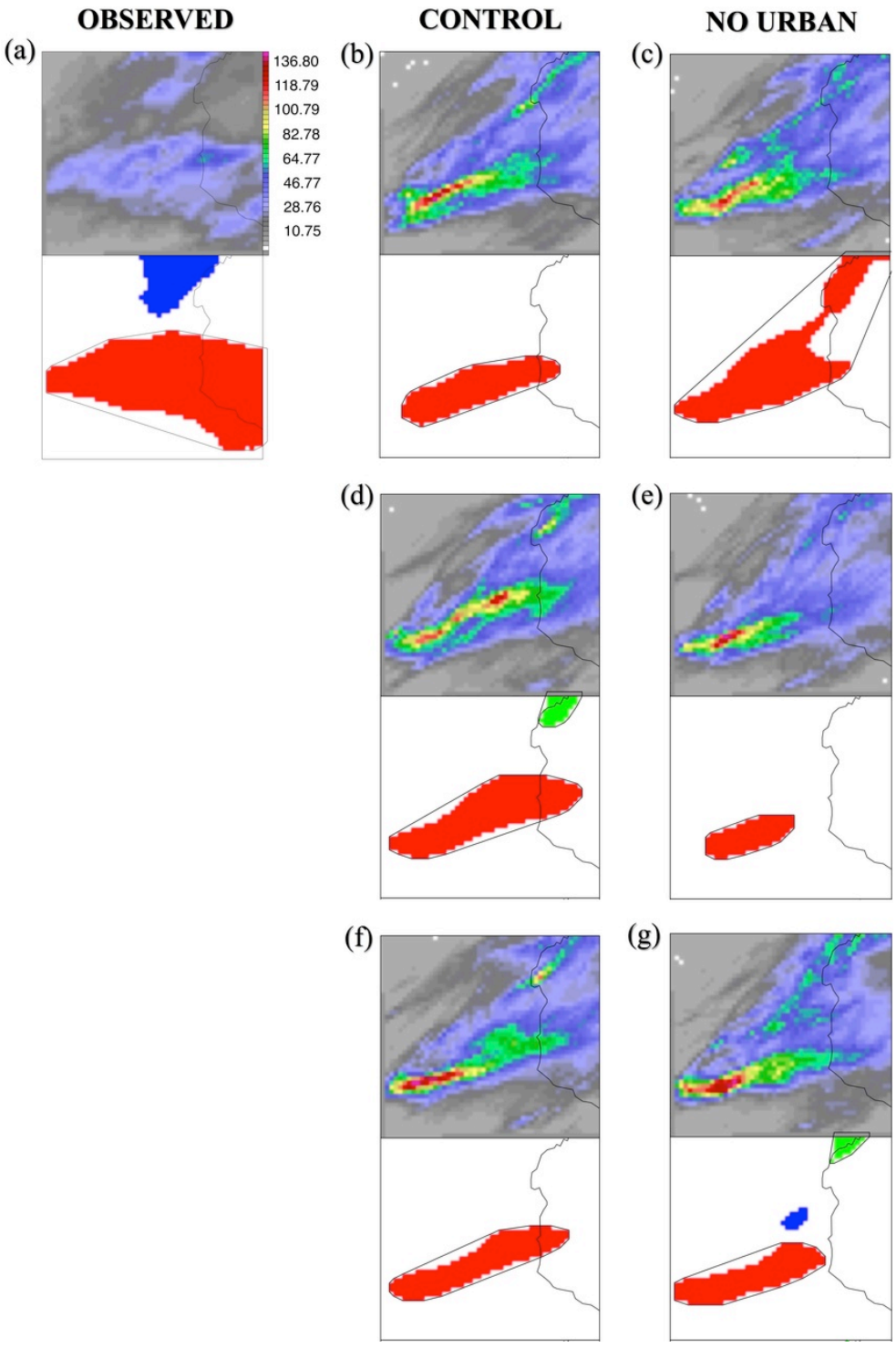

Figure 4.5 The top panel shows the accumulated rainfall in millimeters (2100 to 0200 LST on 27-28 August, 2008), and the bottom panel shows the objects (storm cells) identified using MODE for (a) Stage IV observations, (b) original control, (c) original sensitivity, (d) first ensemble member control, (e) first ensemble member sensitivity, (f) second ensemble member control, and (g) second ensemble member sensitivity simulation.

members (Fig. 4.5 (d) and (f)). This is evident in Table 4.1 which lists the various attributes along with the total interest (T) recorded for the storm cell (red object in Fig. 4.5). The largest improvement in the total interest, especially in the centroid distance and intersection area, is observed for the first ensemble pair (E1). The mechanisms leading to such an improvement will be investigated in the following subsection.

Table 4.1 Comparison of object attributes (α) and total interest values (T) for storm cells (red objects) shown in Figures 4.5 and 4.6. Shaded columns represent the ensemble member with greatest improvement in the total interest value compared between control and sensitivity simulations.

Event	**Centroid Distance (grid units)**		**Angle Difference (degrees)**		**Area Ratio (Forecast/ Observed)**		**Intersection Area (grid square units)**		**Total Interest (T)**	
Aug 27-28, 2008	*Control*	*No Urban*	*Control*	*No Urban*	*Control*	*No Urban*	*Control*	*No Urban*	*Control*	*No Urban*
Original	8.85	7.68	27.26	51.84	0.34	0.67	243	366	0.89	0.88
E1	6.36	13.18	29.49	27.51	0.48	0.17	371	116	0.93	0.83
E2	8.07	12.67	30.07	26.59	0.35	0.29	253	177	0.89	0.87
Aug 11, 2007	*Control*	*No Urban*	*Control*	*No Urban*	*Control*	*No Urban*	*Control*	*No Urban*	*Control*	*No Urban*
Original	2.99	14.97	48.54	26.22	0.34	0.38	311	104	0.82	0.88
E1	10.14	14.69	29.86	35.54	0.59	0.24	289	63	0.95	0.81
E2	8.74	14.18	29.26	8.59	0.41	0.51	251	112	0.90	0.87

For the southeast propagating outflow boundary, there are some differences in the direction of storm propagation between the model and the observations. The storm is observed to approach the city from the west before propagating southeast, whereas in the model simulations it approaches from north/northwest of the domain. In the sensitivity simulations, the storm weakens as it passes through the city, with hardly any urban and downwind rainfall. In fact, in the second ensemble sensitivity simulation (E2), the storm propagates eastward after impacting the city producing minimum rainfall to the south of Minneapolis. When the storm is simulated with the

urban land cover, it propagates southeast with more heavy urban rainfall especially in the south and west of the city. Thus, the enhanced precipitation observed in the southwest peripheral region of the urban area is evident only in the control simulation (see Figure 4.6). From Figure 4.6 and Table 4.1, it is clear that the control simulation

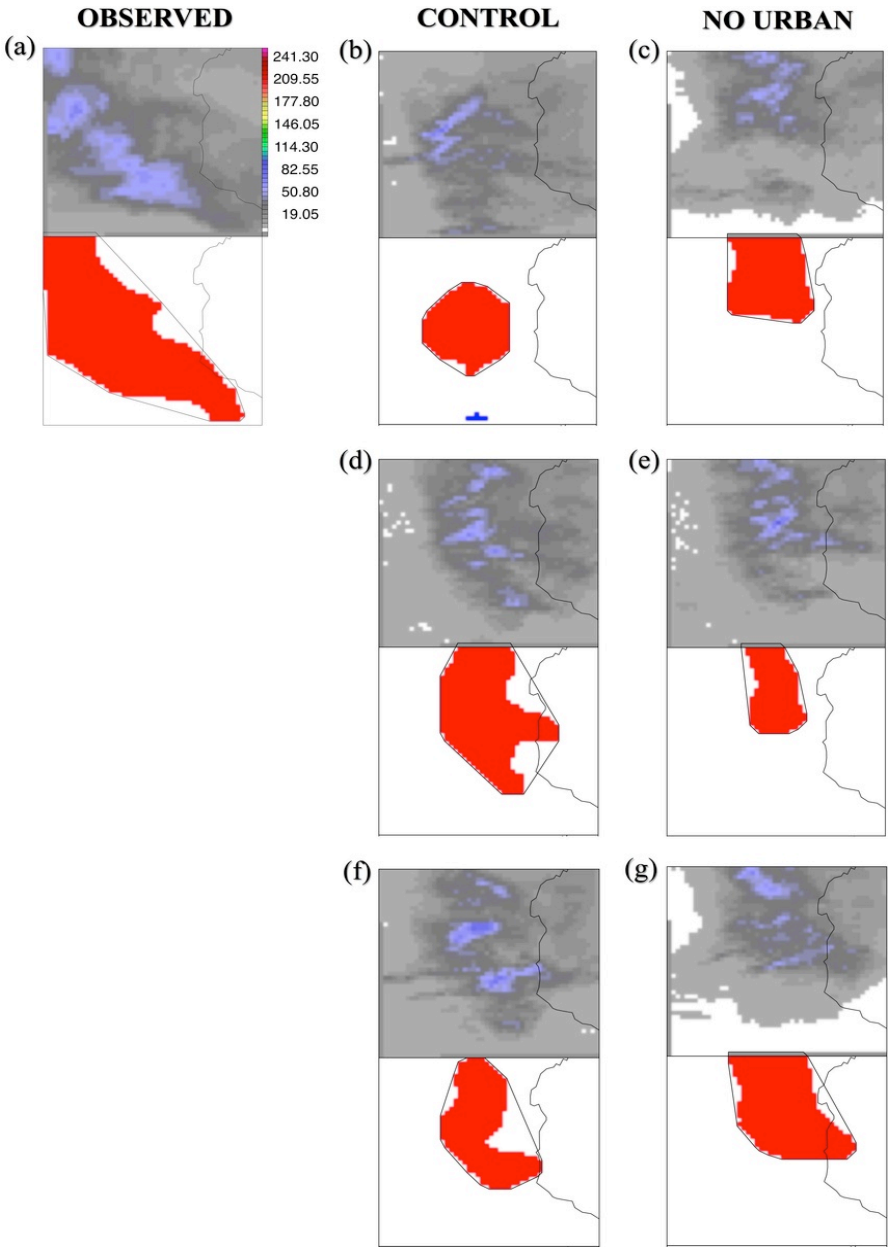

Figure 4.6 Same as Fig. 4.5 but for the accumulated rainfall (0100 to 0600 LST) associated with the outflow boundary event on 11 August, 2007.

is once again able to better represent spatial features, especially the centroid distance and the intersection area attributes, associated with this storm cell (red object). For this case also, the greatest improvement in the total interest is observed for the first ensemble pair (E1).

Thus, from the MODE analyses it appears that urban areas may indeed behave like "hot spots" that favor local convergence during nocturnal propagating events thereby influencing the position of the storm cell. In some cases, they may even alter the direction of the propagating rainfall feature. A qualitative analysis of the mechanisms that influence the storm cell location, and the role of the UHI, is explored in the following subsection.

4.3.3 The urban mechanisms that influence storm cell location

For both nocturnal events, the total interest value associated with the first ensemble member (E1) control simulation is not only the highest but also shows the largest improvement compared to that of the sensitivity simulation (Table 4.1). Therefore, model output from this particular ensemble member is first examined. Incidentally, E1 also records the strongest and most enduring UHI during both events (see Fig. 4.7). Note that the UHI is computed as the mean 2-m temperature difference (control minus sensitivity) averaged over the city polygon. The time period considered in Fig. 4.7 has a 1-hour lead with respect to the accumulated rainfall totals during the corresponding storm event (shown in Fig. 4.4 (a) and 4.4 (b)). This is because I wish to investigate UHI (or UHI-induced convergence) as a prognostic quantity for precipitation.

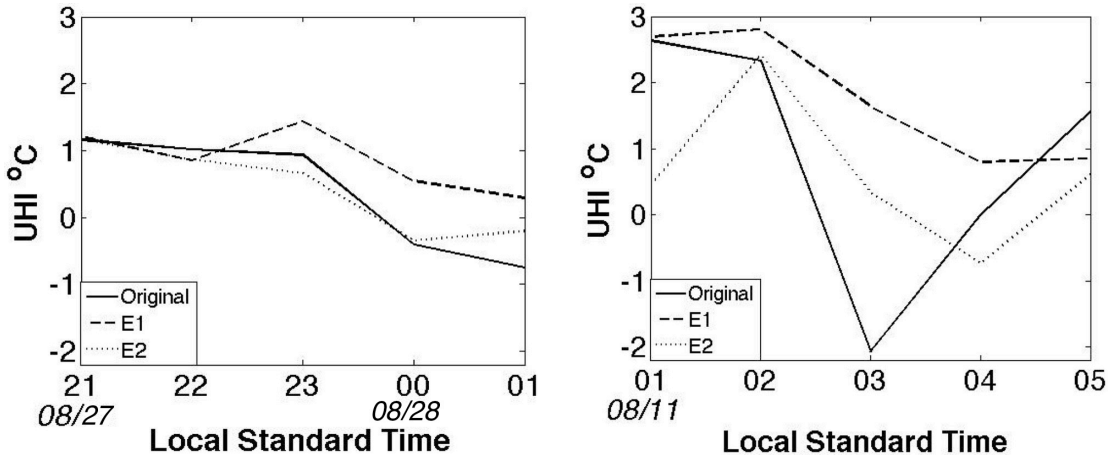

Figure 4.7 The model simulated UHI during the period 2100 to 0100 LST on 27-28 August, 2008 (left panel) and 0100 to 0500 LST on 11 August, 2007 (right panel).

4.3.3.1 Nocturnal propagating squall line

In order to investigate the urban induced mechanisms that may influence storm cell position associated with the squall line event, the differences between the first ensemble member (E1) control and sensitivity simulations are examined. The hourly accumulated rainfall associated with the squall line event, along with the 2-m temperature, 10-m winds and surface pressure vertical velocity during the previous hour, are shown in Figures 4.8 and 4.9. Note that the surface pressure vertical velocity (ω) is a proxy for convergence, with positive (negative) values indicating divergent (convergent) motion at the surface. The UHI is clearly evident at 2100 LST prior to the occurrence of the event (Fig. 4.9 (a)). As the westerly storm approaches, surface convergence (negative ω; Fig 4.9 (b)) occurs over the northwest edge of Minneapolis followed by precipitation in both control and sensitivity simulations. In the control simulation, there is enhanced convergence in the southwest urban region where the temperature is a maximum (Fig. 4.9 (b)).

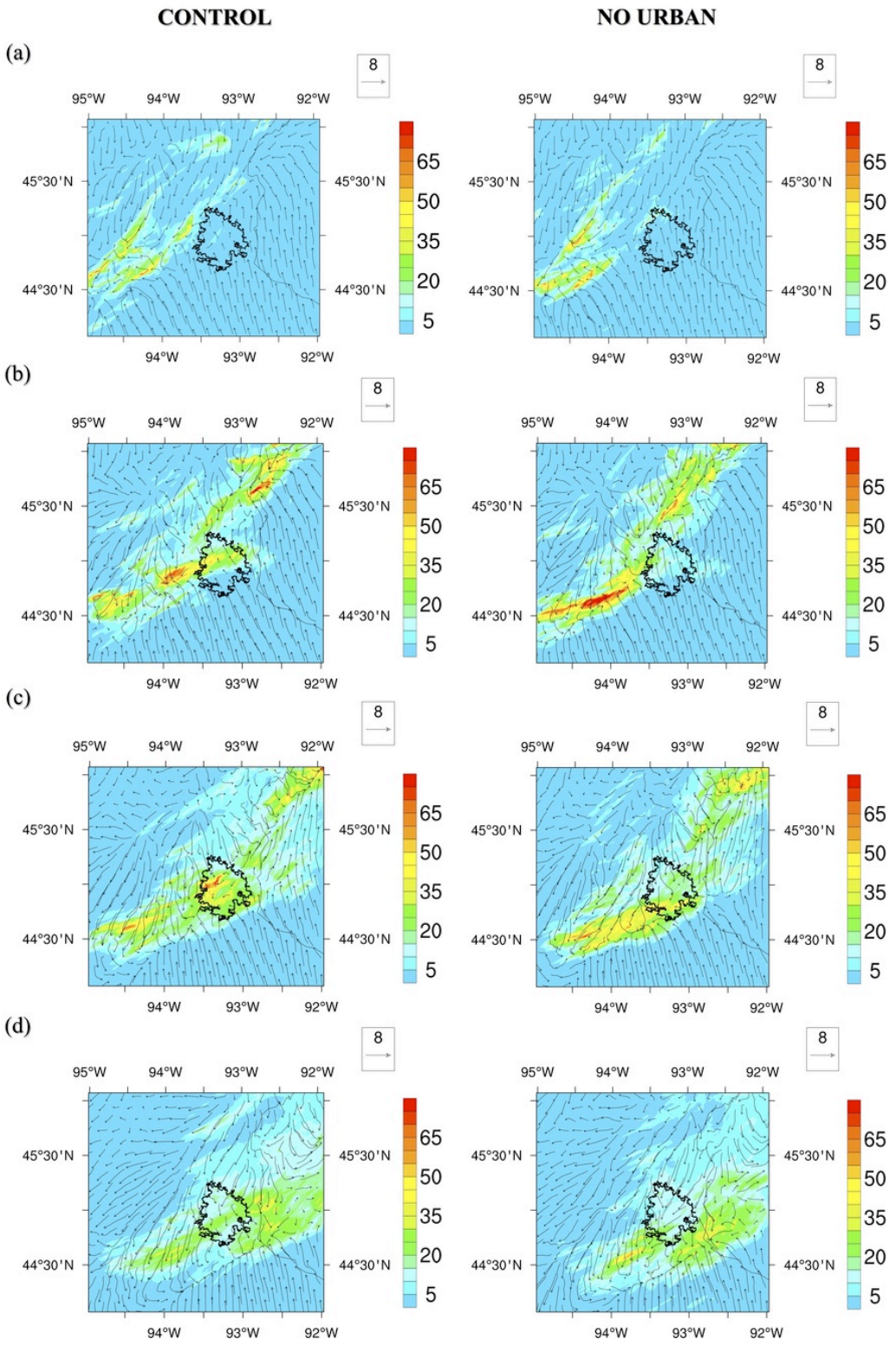

Figure 4.8 The hourly accumulated rainfall (mm) from 2200 to 0100 LST ((a)-(d)), and 10-m horizontal winds ($m.s^{-1}$) during the period 2100 to 0000 LST ((a)-(d)), for the first ensemble member control (left) and sensitivity (right) simulations on 27-28 August, 2008.

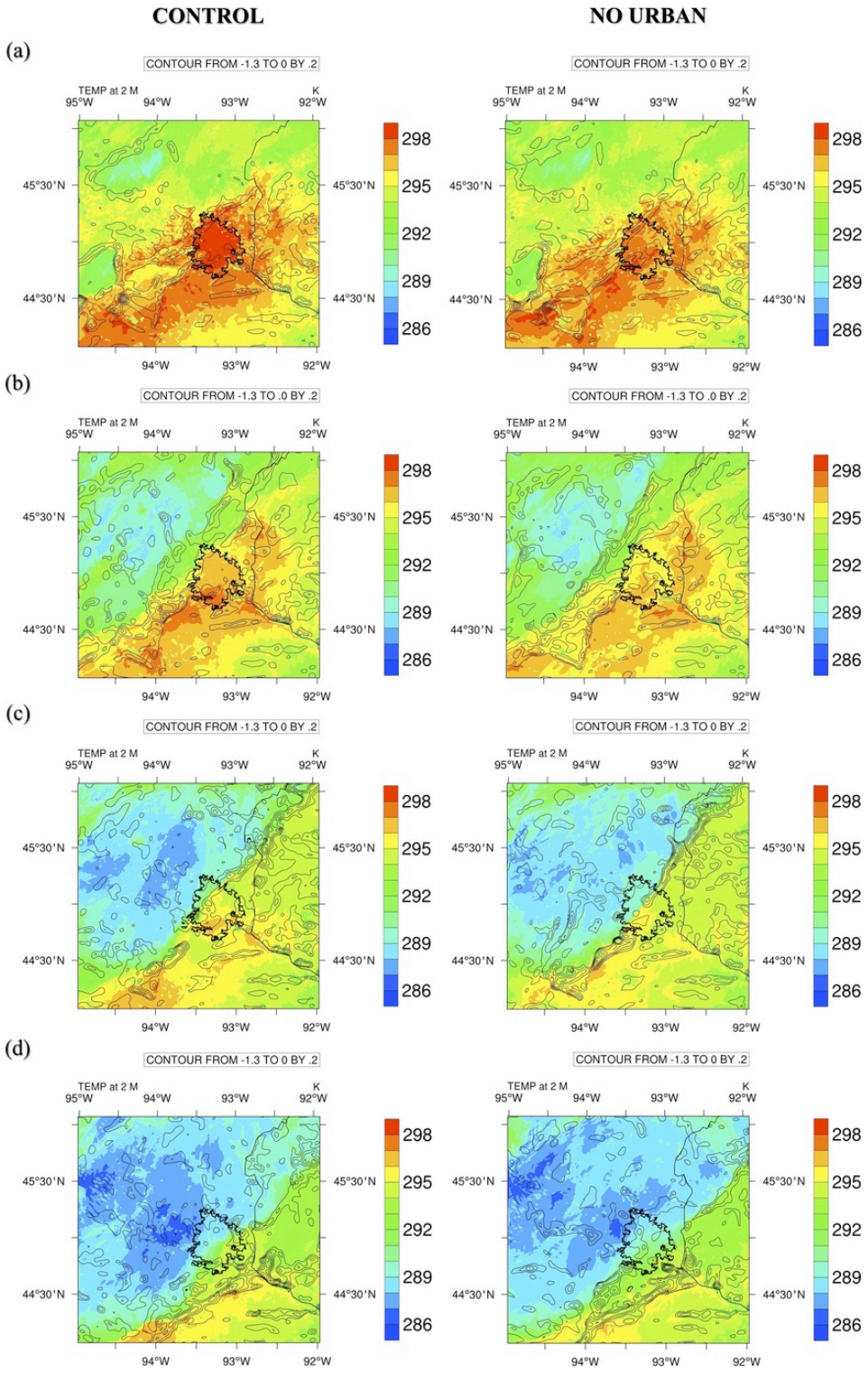

Figure 4.9 The 2-m temperature (K) and surface pressure vertical velocity (Pa.s^{-1}) during the period 2100 to 0000 LST ((a)-(d)), for the first ensemble member control (left) and sensitivity (right) simulations on 27-28 August, 2008.

When the storm occurs over the city at 2300 LST, the UHI is still visible in the control simulation (Fig. 4.9 (c)), and convergence followed by precipitation occurs along the southwest-northeast direction (left panels of Fig. 4.9 (c) and Fig. 4.8 (c)). The winds are weaker over the urban area during this hour (left panel of Fig. 4.8 (c)) suggesting that low-pressure conditions may exist. In the sensitivity simulation however, the surface winds do not appear to slow down (right panel of Fig. 4.8 (c)), and the convergent mesoscale boundary is not continuous over Minneapolis (right panel of Fig. 4.9 (c)). This could be the reason that the precipitation is less intense (right panel of Fig. 4.8 (c)). At 0000 LST, the UHI is nearly overcome due to precipitation except for the presence of warmer temperatures accompanied by enhanced convergence along the eastern peripheral urban region (Fig. 4.9 (d)). As the storm propagates eastward, the control simulation shows increased precipitation over this region that is not observed in the corresponding sensitivity simulation (Fig. 4.8 (d)).

Thus, from Figures 4.8 and 4.9, it appears that the spatial convergence and precipitation patterns associated with the nocturnal propagating squall line may be influenced to some extent by the UHI. The lower wind speeds observed in Fig. 4.8 (c) indicates that increased frictional convergence may possibly lead to reduced surface pressure over the urban area during the storm. Figures 4.8 (a), (b) and (c) also suggest that surface winds may turn cyclonically as the storm approaches the urban area. Several past studies have indicated a similar cyclonic effect on airflow over cities during conditions of strong winds and UHI (Shreffler 1978; Graham 1968; Lee 1977). Such an effect may also contribute to the enhanced convergence in the control simulation. The role of the UHI, frictional dampening, and cyclonic turning of surface

winds, in producing anomalous surface convergence is investigated further by comparing between various ensemble members.

For each ensemble simulation, the anomaly in the mean surface wind speed, wind direction, surface pressure vertical velocity (ω), vertical mixing height, and surface pressure, are examined by averaging these quantities over the city polygon for control and sensitivity simulations (Fig. 4.10). A low-pressure anomaly at the surface is a useful indicator of convergence and rising motion within the atmospheric column, whereas wind speed decrease is a proxy for frictional drag over the urban area. Enhanced vertical mixing height may also contribute to frictional retardation of winds (Wong and Dirks 1978). Note that the vertical mixing height is nothing but the PBL top calculated by the MYJ scheme. Hereafter, the term PBL height will be used synonymously with mixing height. The start and end time of the trends shown in Figure 4.10 include a 1-hr lead with respect to the accumulated urban mean rainfall predicted by the model during the storm event (compare with Fig. 4.4 (a)). The decrease in surface winds over the urban area and the cyclonic turning prior to the storm's approach is visible for all members. Similarly, PBL heights are in general higher due to the urban land cover. Lower pressure, indicating enhanced rising motion, is observed for both the control ensemble members (E1 and E2). Not surprisingly, these simulations demonstrate a more significant impact on the centroid distance and intersection area attributes of the storm cell (see Table 4.1). It can be seen that along with the UHI, the anomaly in pressure vertical velocity (ω) at the surface is a maximum at 2300 LST for the first ensemble member (E1). Thus, the stronger UHI appears to be mainly responsible for the enhanced surface convergence associated with

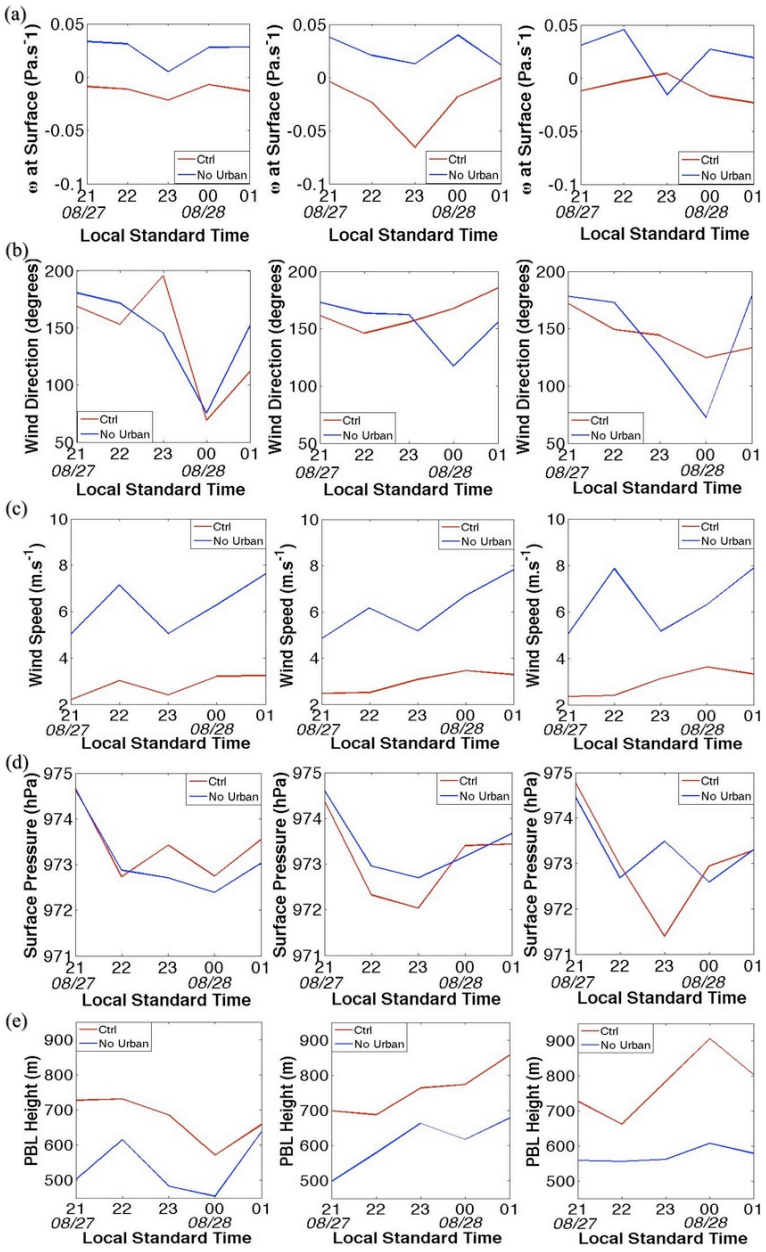

Figure 4.10 The temporal evolution of mean surface quantities averaged over the city polygon viz. (a) pressure vertical velocity (ω), (b) horizontal wind direction, (c) horizontal wind speed, (d) pressure, and (e) the mean PBL height from the control (red) and sensitivity (blue) simulations for the original (left), first ensemble (center) and second ensemble (right) members. The time period is from 2100 to 0100 LST on 27-28, August, 2008.

E1, which could in turn be the most important factor influencing the storm cell position. The surface wind and mixing height anomalies are not perceivably higher for

the first ensemble simulation, and therefore may not be particularly sensitive to the variability in the UHI. They may however, contribute to the storm cell position by influencing the surface pressure anomaly. Note that the differences in surface pressure between control and sensitivity simulations are negligible throughout the diurnal cycle except during the occurrence of the storm. This suggests that unlike the low-pressure anomaly associated with the thermally direct (UHI-driven) circulation under calm conditions (Dixon and Mote 2003), the pressure perturbation during propagating storms may occur *due to the* UHI-enhanced convergence (not the UHI itself). Therefore, the UHI may have an *indirect* influence on the pressure field (which can influence storm spatial characteristics) during synoptically active conditions.

4.3.3.2 Nocturnal propagating outflow boundary

The features associated with the nocturnal propagating outflow boundary that occurred on 11 August 2007, as simulated by the first ensemble member (E1), is shown in Figure 4.11 and Figure 4.12. As the storm approaches (Fig. 4.11 (a)), the surface winds in the control simulation are slower and more cyclonic as was observed for the squall line case. The UHI persists throughout the duration of the storm (Fig. 4.12). The major difference in accumulated rainfall is observed at 0500 LST (Fig. 4.11 (c)) when the storm moves just south of the urban area (4.12 (c)). The sensitivity simulation shows very little precipitation over Minneapolis, whereas the control run shows enhanced rainfall over the southwest as well as other parts of the city. At 0400 LST, a weak UHI exists and is accompanied by enhanced surface convergence over the southwestern part of the urban region in the control simulation (Fig. 4.12 (c)).

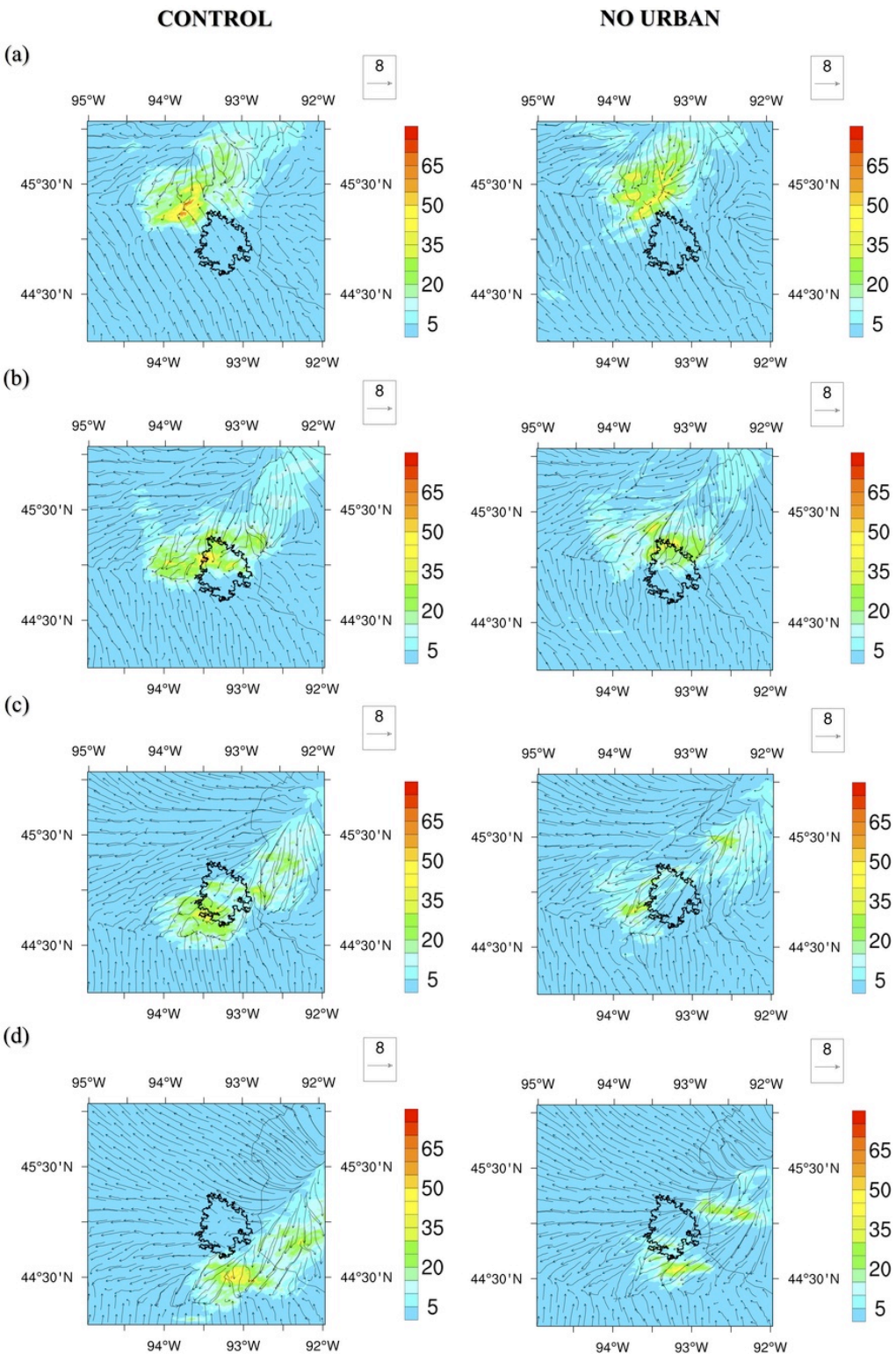

Figure 4.11 The hourly accumulated rainfall (mm) from 0300 to 0600 LST ((a)-(d)), and 10-m horizontal winds ($m.s^{-1}$) during the period 0200 to 0500 LST ((a)-(d)), for the first ensemble member control (left) and sensitivity (right) simulations on 11 August, 2007.

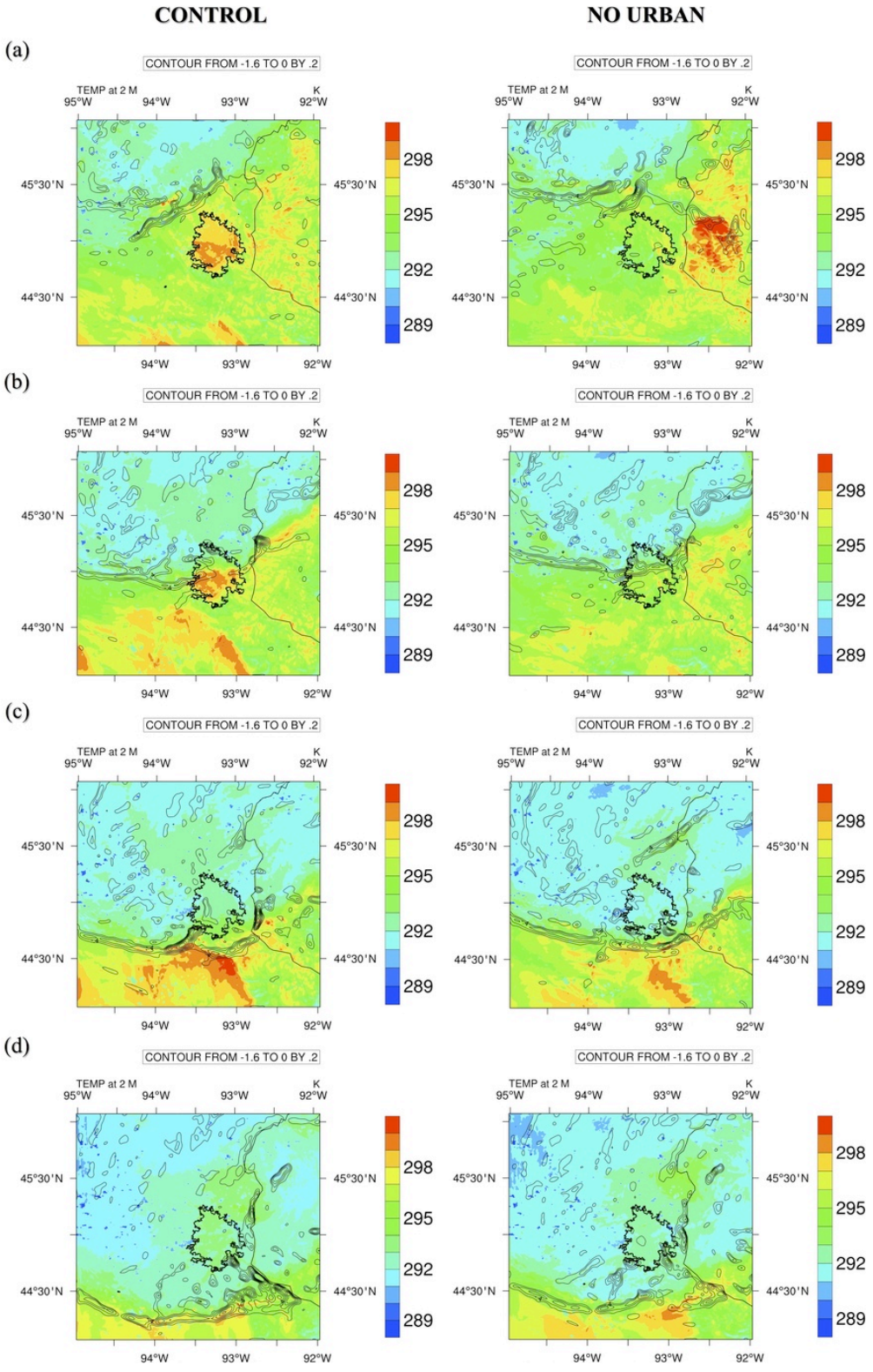

Figure 4.12 The 2-m temperature (K) and surface pressure vertical velocity (Pa.s^{-1}) during the period 0200 to 0500 LST ((a)-(d)), for the first ensemble member control (left) and sensitivity (right) simulations on 11 August, 2007.

Fig. 4.13 compares the divergence field between the control and sensitivity simulations at the same hour. There is stronger subsidence over the eastern part of the city in the sensitivity simulation which may be the reason for the reduced precipitation received during this hour. Also note that the UHI is stronger in southern Minneapolis (Fig. 4.13) where the maximum rainfall in the control simulation occurs (Fig. 4.11 (c)). Thus, the lack of surface divergence in the east as well as UHI-enhanced convergence in the southwestern part of the city, appear to produce more urban rainfall in the control simulation during the subsequent hour (0500 LST).

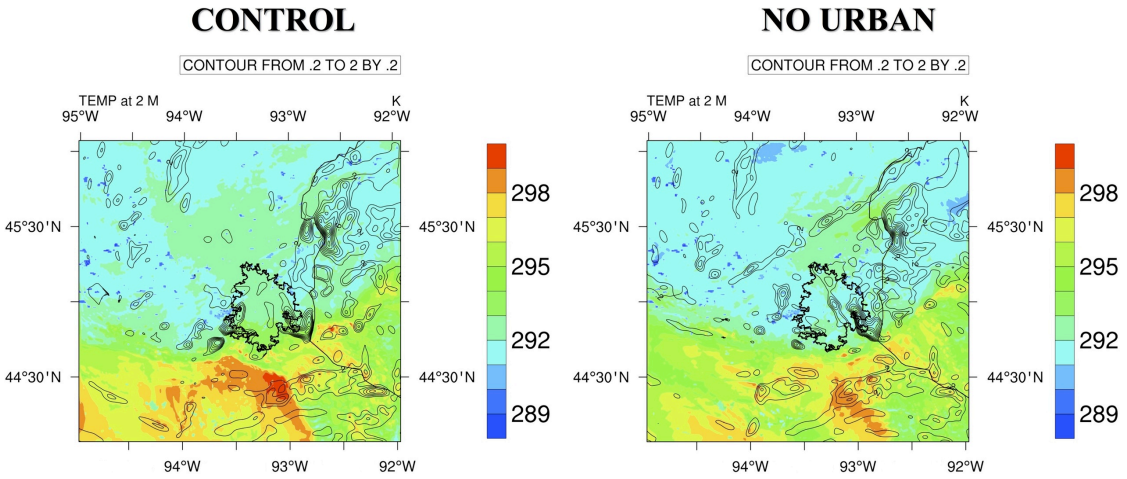

Figure 4.13 The 2-m temperature (K) and surface pressure vertical velocity (Pa.s^{-1}) for the first ensemble member control (left) and sensitivity (right) simulations at 0400 LST on 11 August, 2007.

Similar to Fig. 4.10, the evolution of spatially-averaged quantities over Minneapolis (surface ω, surface wind, surface pressure and vertical mixing height) is compared between control and sensitivity simulations for this event (see Fig. 4.14). Note that the differences in the original control and sensitivity simulations (left panel of Fig. 4.14) indicate that there is a 1-hr lead in the propagation of the storm in the original control

simulation. The reason for this appears to be related to differences in the boundary conditions, and not the urban instability.

In Fig. 4.14, the wind speeds are slower in the control simulation for all ensemble pairs. Larger wind speed differences and a cyclonic turning prior to the occurrence of the storm are observed for the first ensemble member (E1) (center panels of Fig. 4.14 (b), (c)). Moreover, a lack of divergence at 0400 LST for E1 (center panel of Fig. 4.14 (a)) appears to be related to the UHI which is not observed for the remaining two ensemble simulations at this hour (right panel of Fig. 4.7). A low-pressure anomaly, which occurs as a result of this reduced divergence (see center panel of Fig. 4.14 (d)), may influence the storm cell location. Thus, the UHI and related convergence (lack of divergence) appear to play a crucial role in storm spatial characteristics for the first ensemble member (E1), although the frictional drag and the cyclonic turning of winds may also contribute to the low-pressure anomaly. Note that the ensemble member (E1) does not have deeper mixing heights (center panel of Fig. 4.14 (e)) suggesting that the retardation of winds due to frictional drag may primarily result from enhanced surface roughness (not increased vertical mixing).

Therefore, the UHI-induced surface convergence (and related surface pressure anomaly) appears to be important in influencing the storm cell position during both nocturnal events. The relative significance of the surface wind anomaly (compared to UHI) in producing increased frictional convergence needs further investigation. The UHI, enhanced surface convergence as well as lower wind speeds over the urban area, are observed throughout the diurnal cycle. As explained in section 4.3.3.1, the wind speed decrease is a proxy for the frictional drag. It is worth exploring the diurnal

variability in the surface convergence anomaly with respect to the UHI and the frictional drag (wind speed difference) on the days before, after, and during each storm event.

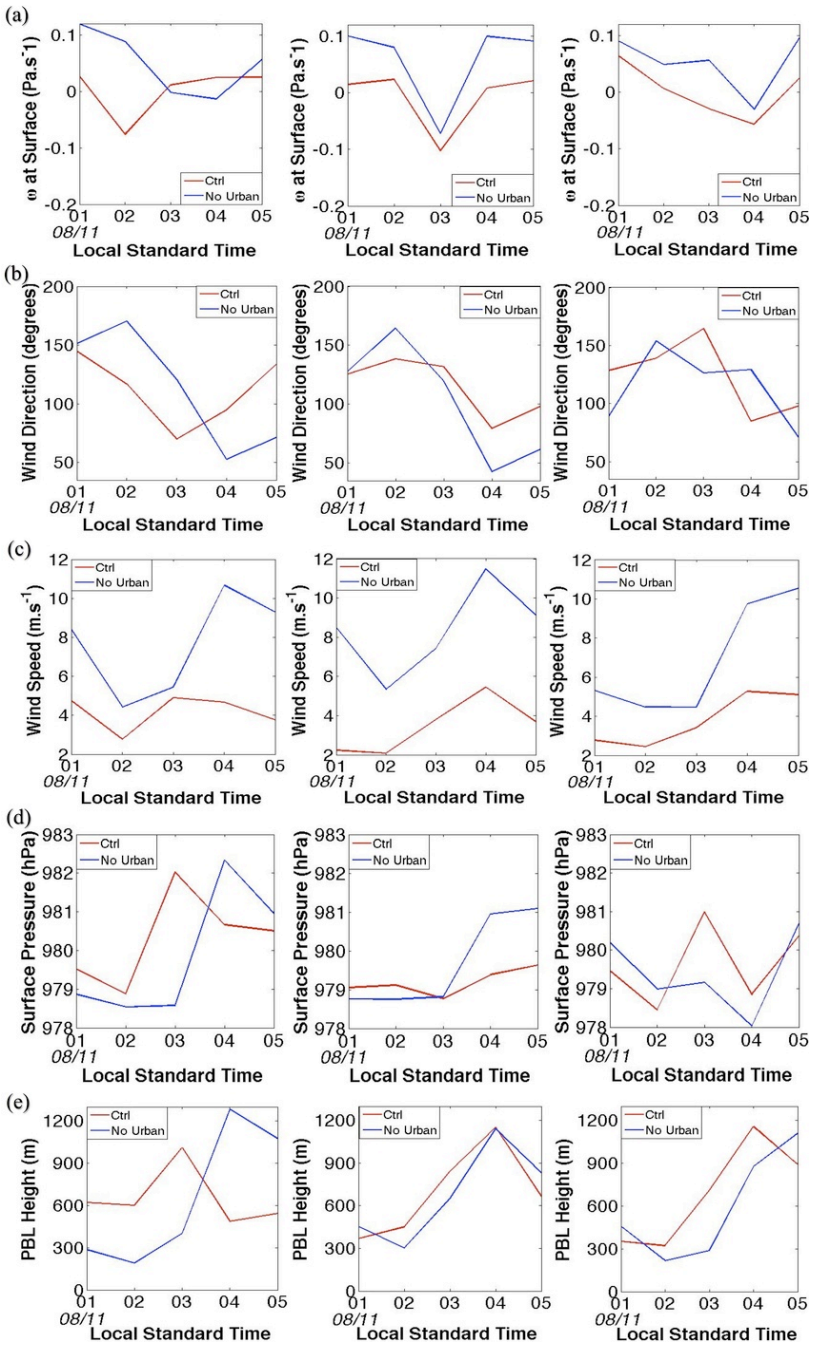

Figure 4.14 Same as Figure 4.10 but for time period between 0100 to 0500 LST on 11, August, 2007.

Figures 4.15 and 4.16, demonstrate the diurnal cycle in the surface ω difference (sensitivity minus control), the UHI, and the surface wind speed difference (sensitivity minus control) for both nocturnal events. The UHI appears to have a stronger influence on the diurnal pattern of surface convergence anomaly during no storm days (see Fig. 4.15 (a) and Fig. 4.16 (a)). When nocturnal storms occur, the UHI is typically weaker (< 2 °C) and the surface wind speed differences are larger (> 3 m s^{-1}). This is because storm days are associated with stronger winds, which increases frictional retardation but may weaken the UHI due to temperature advection effects (Wong and Dirks 1978). As a result, frictional drag appears to contribute more heavily to the surface convergence during rainfall events (center panels of Fig. 4.15 (b) and Fig. 4.16 (b)). Future sensitivity experiments will be conducted to quantify the role of UHI versus surface friction in influencing the convergence and storm spatial characteristics associated with nocturnal propagating storms.

Thus, it is evident that the role of the urban land cover is to produce an increase in local rainfall during nocturnal storms. This occurs due to convergence resulting from thermal (UHI) as well as dynamical (frictional) effects. The divergence (if any) due to the building barrier effect does not appear to be a prominent influence on urban rainfall patterns.

The downwind rainfall intensification was observed and discussed in Chapter 3, but not simulated by the model. Nevertheless, the presence of a nocturnal urban PBL instability is examined in the following subsection.

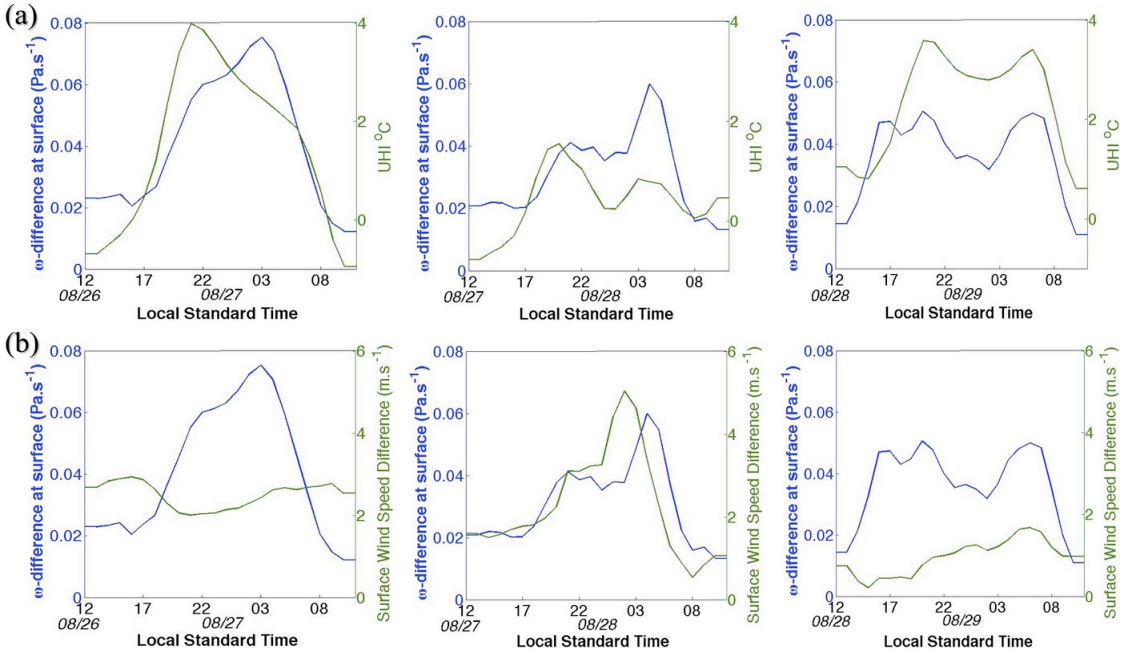

Figure 4.15 The diurnal cycle of the ensemble-mean difference in surface ω (sensitivity minus control), compared with (a) UHI, (b) the ensemble-mean difference in surface wind speed (sensitivity minus control), on 26-27 August, 2008 (left), 27-28 August, 2008 (center) and 28-29 August, 2008 (right).

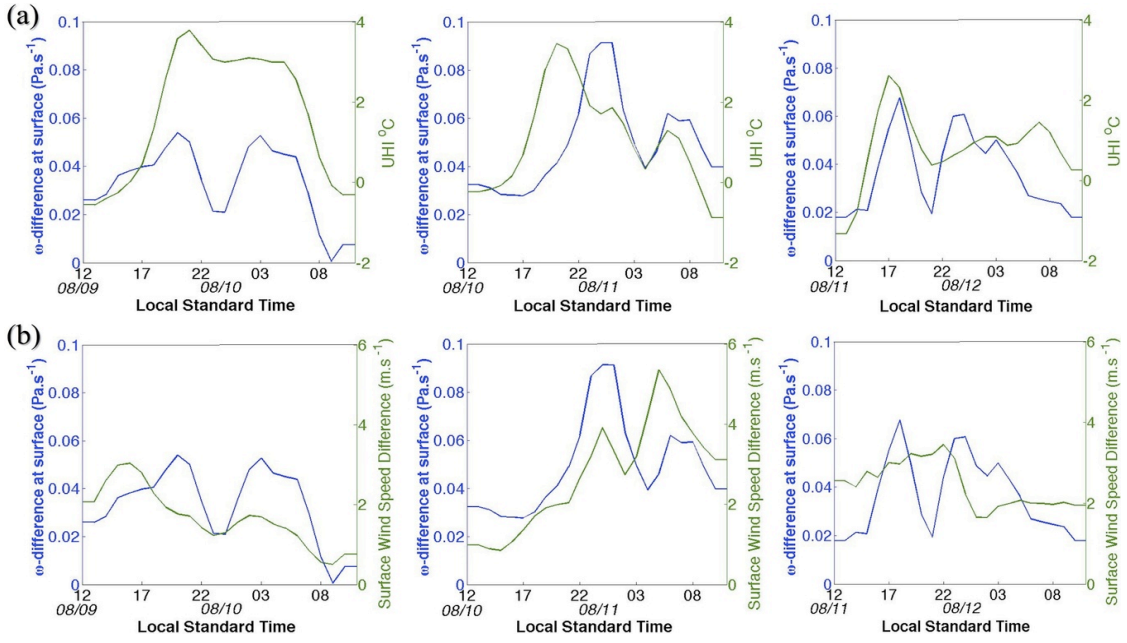

Figure 4.16 Same as Fig. 4.15 but for 09-10 August, 2007 (left), 10-11 August, 2007 (center) and 11-12 August, 2007 (right).

4.3.4 Instability in the urban nocturnal boundary layer

As discussed in section 4.3.3.1, deeper mixing heights may occur over the urban region during storm events. This suggests that the urban PBL perturbation may even exist during the night. Figure 4.17 (a) and Figure 4.18 (a) compare the diurnal cycle of the PBL height differences (control minus sensitivity) to inspect this.

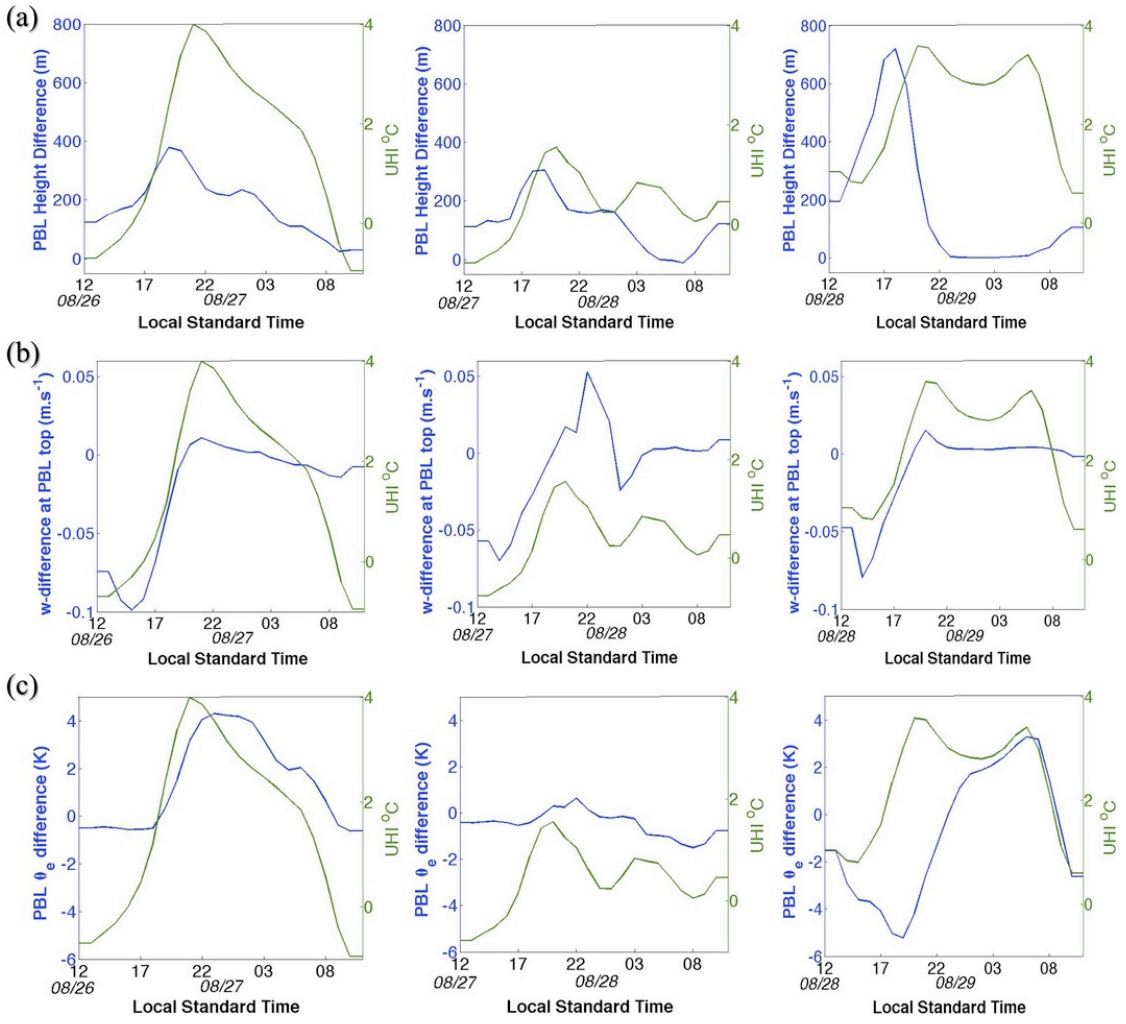

Figure 4.17 The diurnal cycle of the ensemble-mean UHI and the ensemble-mean differences (control minus sensitivity) in (a) PBL height, (b) PBL top vertical velocity, and (c) PBL mean θ_e, on 26-27 August, 2008 (left), 27-28 August, 2008 (center) and 28-29 August, 2008 (right).

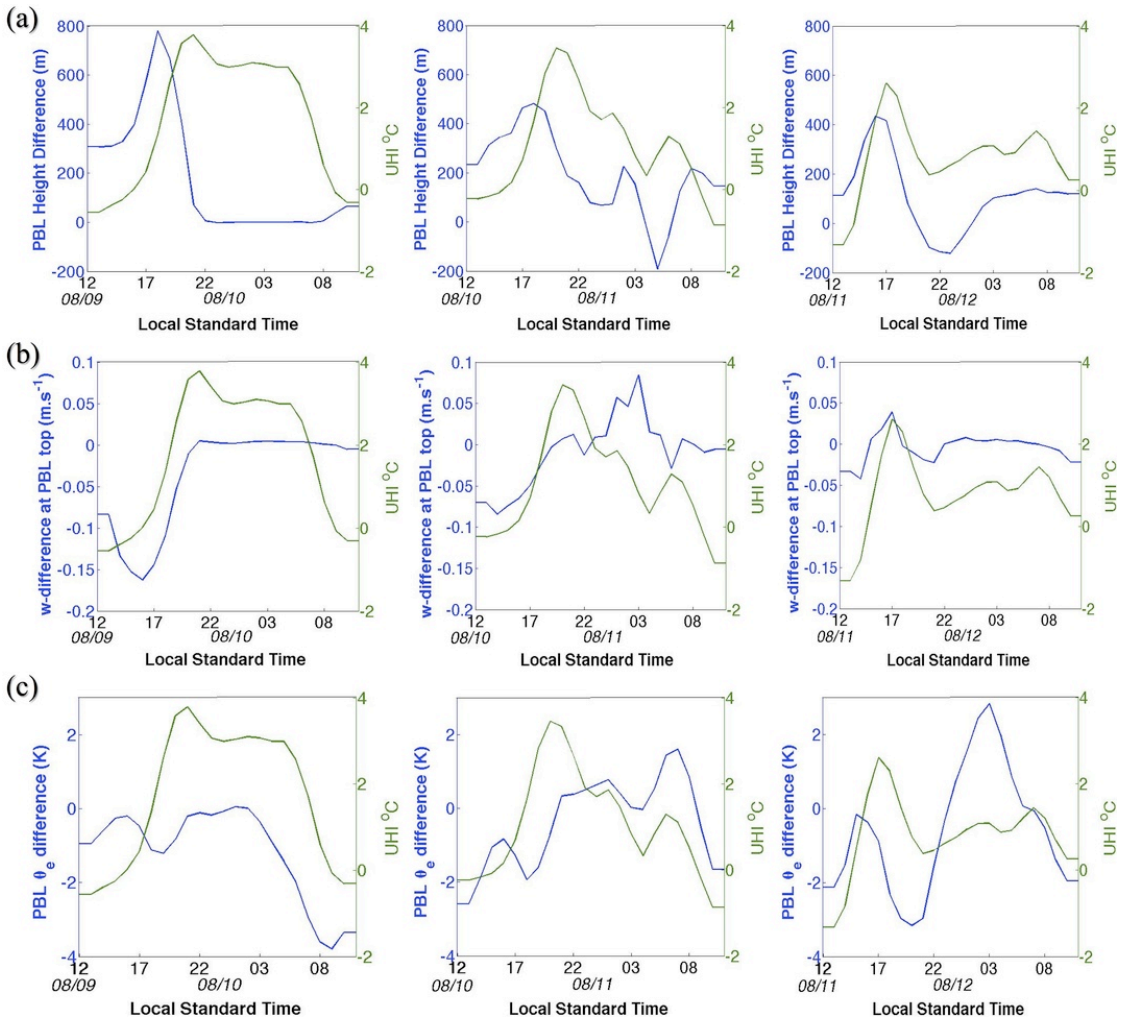

Figure 4.18 Same as Fig. 4.17 but for 09-10 August, 2007 (left), 10-11 August, 2007 (center) and 11-12 August, 2007 (right).

Although the PBL may remain slightly higher over the urban area during nighttime, the peak in the height differences occurs during late-afternoon or evening hours (between 1700-2000 LST). Even with a strong nocturnal UHI, a positive PBL height anomaly may not appear on some nights (right panel of Fig. 4.17 (a) and left panel of Fig. 4.18 (a)). A comparison of the diurnal cycle of vertical velocity differences (w-difference) at PBL top (control minus sensitivity) suggests that the urban nocturnal boundary layer does not support a UHI-perturbed circulation. The

velocity differences (Fig 4.17 (b) and Fig. 4.18 (b)) are negligible during nocturnal hours (except during storm days). Just like the surface pressure anomaly, the vertical velocity at the top of the urban PBL only maximizes during the time of maximum convergence associated with the storm (see center panel of Fig. 4.17 (b) and Fig. 4.18 (b)). Thus, it appears that the nocturnal UHI does not precondition the stable boundary layer to support enhanced vertical motion during nighttime.

The presence of a thermodynamic instability in the form of enhanced equivalent potential temperature (θ_e) in the nocturnal urban PBL is also investigated (Fig. 4.17 (c) and Fig. 4.18 (c)). A positive anomaly in θ_e-values may occur during nighttime in the urban PBL (left and center panels of Fig. 4.17 (c); right and center panels of Fig. 4.18 (c)). This suggests that the Urban Hygrothermal Anomaly (UHA) may exist at the surface, which will be investigated in the following subsection.

4.3.5 The Urban Hygrothermal Anomaly (UHA)

Figure 4.19 compares the diurnal cycle of the UHA with that of UHI as well as the surface mixing ratio difference (control minus sensitivity) for both nocturnal events. The UHA (or positive surface θ_e-values over the urban area) typically occurs during nocturnal hours. It appears to be modulated by both the UHI as well as the difference in the surface mixing ratio (Fig. 4.19). Although a daytime UHI is common, the UHA may not be visible because of drier conditions during the day (bottom panels of Fig. 4.19 (a), (b)). The surface mixing ratio remains largely negative throughout the diurnal cycle, except during nighttime when the urban-rural differences are small and may turn positive. Therefore, it appears that urban areas may develop an UHA during

nocturnal hours due to the combination of less negative moisture differences and the nocturnal UHI.

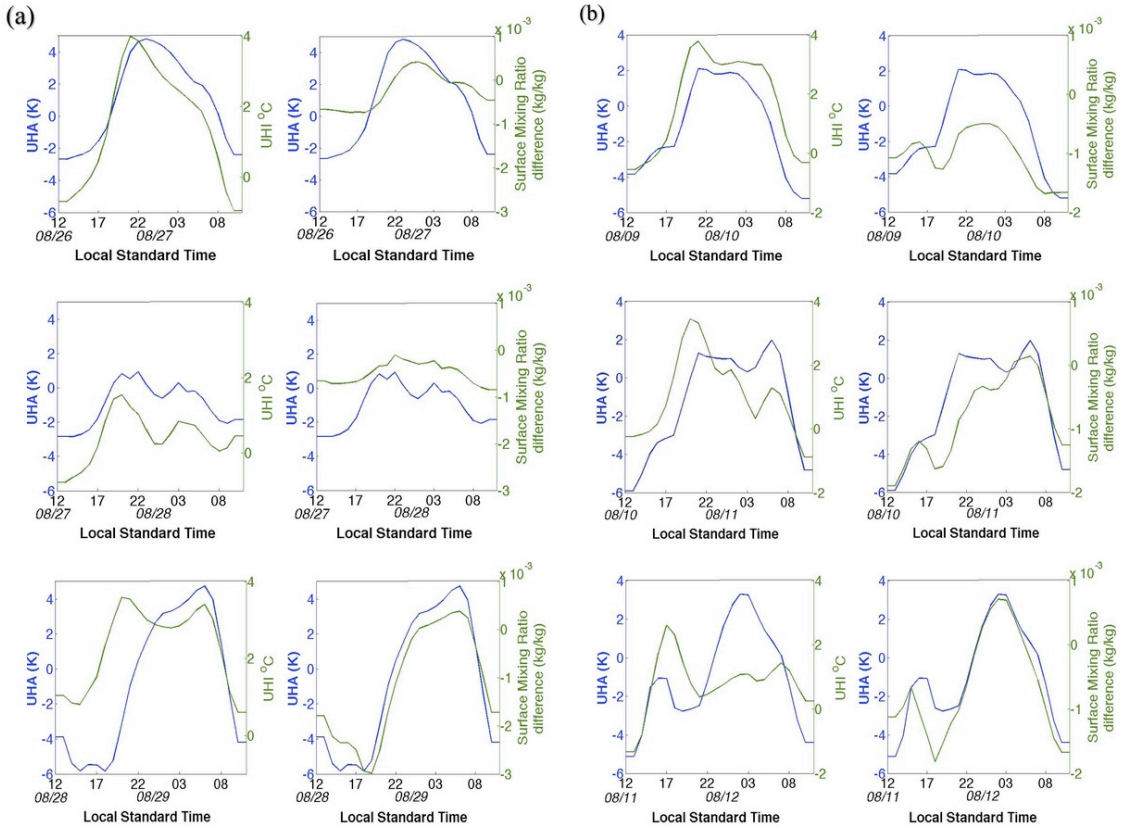

Figure 4.19 The diurnal cycle of the ensemble-mean UHI (left) and the difference (control minus sensitivity) in surface mixing ratio (right) shown along with the UHA on (a) 26-27 August, 2008 (top), 27-28 August, 2008 (center) and 28-29 August, 2008 (bottom); and (b) 09-10 August, 2007 (top), 10-11 August, 2007 (center) and 11-12 August, 2007 (bottom).

The surface latent heat flux differences averaged over the city polygon is compared between the control and sensitivity simulations (Fig. 4.20). It can be confirmed that rural areas indeed experience an increased latent heat flux during the day, but the differences are almost negligible during night. In some cases, the latent heat flux turns negative over the rural area during nocturnal hours due to the condensation of dew, but continues to remain positive over the urban region (left panel

of Fig. 4.20 (a)). This suggests that urban surfaces may experience lack of dew condensation, leading to a positive surface moisture anomaly during nighttime. Thus, it appears that a nocturnal thermodynamic instability (UHA) may indeed exist over urban areas. Its contribution to downwind intensification of storms will be investigated in future modeling studies.

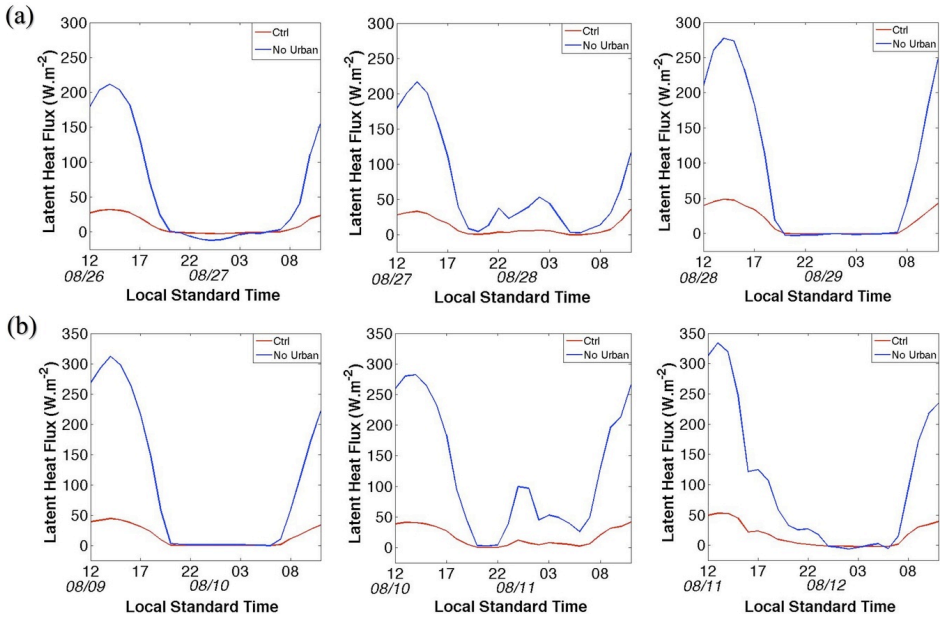

Figure 4.20 The diurnal cycle of the ensemble-mean latent heat flux from control (red) and sensitivity (blue) simulations on (a) 26-27 August, 2008 (left), 27-28 August, 2008 (center) and 28-29 August, 2008 (right), and (b) 09-10 August, 2007 (left), 10-11 August, 2007 (center) and 11-12 August, 2007 (right).

4.4 Conclusions

In summary, it is seen that the storm cells associated with nocturnal propagating events are sensitive to the presence of the urban land cover. Urban areas behave like "hot spots" experiencing an increase in surface convergence and rainfall during such events. The divergence due to the building barrier effect (if any) does not appear to have a dominant influence on storm spatial characteristics. Model analysis

using MODE suggests that the centroid distance and intersection area attributes of storm cells are most greatly influenced by the presence of urban land cover. The convergence, produced due to thermal (nocturnal UHI) as well as dynamical (frictional drag) effects, leads to a negative surface pressure anomaly which appears to influence the position of the storm cell. A cyclonic turning of surface winds is also observed prior to the storm's approach that may further contribute to the low-pressure anomaly. Frictional convergence appears to be more pronounced during storm days, likely due to stronger winds. A comparison between various ensemble members suggests that the UHI and the associated convergence (lack of divergence) are the most significant factors influencing local urban rainfall and storm spatial characteristics. This may be the reason for the observed increase in the urban mean rainfall anomaly (URA_{mean}) associated with nocturnal propagating storms over Minneapolis (discussed in the previous chapter). It is also possible that this steering of storm cells due to the UHI, may increase the nocturnal thunderstorm frequency that has been reported for other urban areas in the past (Huff and Changnon 1973). Future sensitivity experiments will be conducted to quantify the role of UHI versus frictional drag in influencing surface convergence and storm spatial characteristics in the vicinity of urban areas.

An examination of the urban boundary layer instability suggests that the perturbed PBL circulation may not be active during nighttime. A positive surface θ_e-anomaly or UHA may occur due to the nocturnal UHI and less negative moisture difference at night. This may lead to increased θ_e-values within the urban nocturnal PBL. The contribution of this thermodynamic instability to the downwind intensification of propagating storms will be investigated in the future.

Chapter 5: Summary and Future Work

5.1 Thesis Summary

In the first part of this thesis, the cause for some common biases associated with the diurnal cycle of warm season rainfall is investigated. The problem of premature, light rain is observed when several late-afternoon, surface-based convective events are simulated using two popular cumulus parameterization schemes (viz., Betts-Miller-Janjić and Kain-Fritch), which are both considered suitable for use in mesoscale models. It appears that explicit convection at increased horizontal resolution may reduce this bias to some extent. The negative buoyancy constraints in the trigger for moist convection in the parameterization schemes are evaluated. Apart from modeling analyses, the use of high-resolution satellite-derived soundings to understand and verify relevant trigger processes in the real atmosphere is demonstrated. The results suggest that more stringent criteria, especially for the CIN between the LCL and the LFC, may be required for delaying parameterized convection in mesoscale models. For example, the Kain-Fritsch (KF) scheme triggers moist convection from the LCL, employing implicit constraints for negative buoyancy above this level. A simple modification is made to allow moist convection (shallow and deep) to begin from the LFC instead of the LCL. Simulations with the revised Kain-Fritsch scheme (KF_{CIN}) indicate that it can be used successfully in a mesoscale model, since the grid-resolvable processes are able to overcome the negative buoyancy below the LFC prior to activating parameterized convection. The revised scheme leads to a small but positive improvement in the diurnal phase and amplitude of rainfall. In a

seasonal climate simulation using the same mesoscale model, the scheme improves the nocturnal phase propagation in the Central Plains region by curbing overactive daytime convection. As discussed in section 1.1, the characteristics of nocturnal rainfall in this region have thus far been simulated based on the quasi-equilibrium assumption, by cumulus schemes that are sensitive to the free-tropospheric forcing (Liang et al. 2004; Zhang 2003; Lee et al. 2008). In particular, studies have shown that by decoupling convection from the PBL in cumulus schemes, processes such as mid-level moisture advection due to the low-level jet may easily generate nocturnal instability (increase in CAPE) (Zhang 2003; Lee et al. 2008). The resulting nighttime convection simulated by such schemes is considered to be in quasi-equilibrium with the free-tropospheric forcing (Zhang 2002; 2003). In this study, it is shown that by including appropriate thermodynamic constraints to better represent non-equilibrium (or triggered) convection in the KF scheme, it is possible to capture both daytime as well as nocturnal phase of rainfall in mesoscale models, without the exclusion of boundary layer processes. In the revised trigger of the Kain-Fritsch scheme (KF_{CIN}), the CIN below the LFC inhibits daytime boundary layer convection over the Great Plains region, thereby favoring the scheme's response to dynamical processes that occur during the nighttime. The sensitivity of the convective trigger to the large-scale forcing at the LCL is thus reduced, and the potential of the scheme to capture the geographical variability of warm season rainfall characteristics is enhanced. However, the scheme's performance still remains highly sensitive to the *type* of large-scale (mesoscle) forcing. For example, the use of moisture advection (KF_{MA}) instead of mass convergence (KF) trigger produces significant differences in the precipitation

characteristics (discussed in section 2.3.8). This suggests that additional observational studies are needed to better understand the mesoscale variability of processes that constrain (or trigger) convective initiation in nature. In the future, regional and global modeling experiments will be used to test the robustness of the revised scheme (KF_{CIN}) in simulating convection under varying regimes. Moreover, the sensitivity of convective rainfall to the type of mesoscale (large-scale) forcing in different regions will be explored using satellite observations and modeling analyses.

The second part of this thesis investigated the UHI-influence on warm season precipitation by conducting a multi-city analysis using high-resolution surface observations over several US cities. The variability in UHI-rainfall impacts is explored. The characteristics of rainfall anomalies are especially found to differ for inland and coastal cities. The rainfall anomalies are more pronounced over coastal urban areas, occurring mainly during the daytime likely due to the UHI-sea breeze (or UHI-lake breeze) interaction. Additional model-based sensitivity studies are needed to investigate the role of this interaction in producing extreme positive rainfall anomalies. This may have important implications for coastal urban areas especially in the forecasting of flood events, and for water resources planning. For inland cities, the rainfall anomalies have lesser magnitude but the UHI appears to be the dominant mechanism influencing afternoon and nocturnal precipitation, locally as well as downwind.

The afternoon rainfall anomaly has been studied in the past during METROMEX (Ackerman et al. 1977; Changnon et al. 1981), and verified

subsequently by several modeling studies (Vukovich and Dunn 1978; Hjemfelt 1982; Baik et al. 2001). METROMEX however did not investigate the cause for the nocturnal rainfall increase (Changnon and Huff 1986). Earlier studies have speculated that the UHI-induced thermal convergence may be responsible for an observed increase in the frequency of nocturnal urban thunderstorms (Huff and Changnon 1973; Changnon and Huff 1986). In more recent literature, the focus has shifted from analyzing UHI effects on propagating storms to studying the urban impact on thunderstorm development under calm background flow conditions (Dixon and Mote 2003; Bentley et al. 2010; Ashley et al. 2012). In Chapter 3 of the present study, an increase in the urban mean rainfall anomalies associated with nocturnal propagating storms is observed for Minneapolis and DC, suggesting that storms are favored over the urban center. The storm intensification, however, is found to occur in the downwind region. From model sensitivity analyses performed in Chapter 4, it is found that urban areas indeed act like "hot spots" during nighttime, steering storm cells associated with propagating storm events towards the urban core. Thus, an inland urban area may easily experience an increase in the frequency of nocturnal thunderstorms. The UHI-induced convergence, enhanced surface roughness over the urban area, and more cyclonic winds prior to the storm's approach, appear to be responsible for altering the storm cell location. The model simulations, however, do not capture the downwind intensification of rainfall observed during these nocturnal storm events.

The downstream advection of the UHI-perturbed PBL circulation is the most well-known cause for the daytime rainfall increase observed downwind of cities

(Ackerman et al. 1977; Shepherd et al. 2005). The mechanism for the nocturnal downwind rainfall increase associated with propagating thunderstorms has not yet been explored in the literature. In Chapter 3, it is seen that the low-level (1000-700 hPa) urban mean wind vector is well-correlated with the downwind maximum rainfall anomalies during both night as well as daytime events. This suggests that an urban low-level instability, similar to the daytime PBL perturbation, may exist even during night. The hypothesis that urban areas may have high PBL θ_e values during nighttime is explored. Increased low-level θ_e-gradients and its downstream advection are known to have prognostic applications for determining regions of maximum rainfall (Campbell 1991; Smith 1993; Farina and DiStefano 1998). In Chapter 3 of the present study, a nocturnal positive surface θ_e anomaly is indeed observed for the cities considered. This is named the Urban Hygrothermal Anomaly (UHA). It may arise due to the much warmer temperature anomaly, and the nearly negligible but less negative moisture anomaly over urban areas during nighttime hours. In Chapter 4, the presence of this anomaly is confirmed in the model simulations but the downwind rainfall increase is not simulated. Therefore, additional experiments will be performed in the future to investigate the hypothesis that positive low-level θ_e-gradients produce increased precipitation downwind of urban areas.

5.2 Future Work

5.2.1 Investigating the applications of the revised Kain-Fritsch scheme

Convection and its interaction with the large-scale environment have been widely studied with a view to understand as well as parameterize the effect of cumulus clouds within numerical models. As discussed in Chapter 1 (Introduction), there are different approaches for parameterizing convection, for e.g., consideration of Type I versus Type II instability, coarse resolution versus mesoscale models, the choice of the dynamical (large-scale) trigger mechanism, and so on. In Chapter 2, it was observed that proper negative buoyancy considerations in the KF scheme may reduce, to some extent, the sensitivity of the convective trigger to the large-scale forcing especially within the PBL. Although this is a positive result, it needs further exploration. The use of this revised scheme in accurately simulating the late-afternoon peak of surface-based convection, nocturnal elevated convection, shallow convection in stratus clouds, propagating Mesoscale Convective Systems (MCSs), and tropical features such as the Madden-Julian Oscillation (MJO), will be investigated using model-based case studies in the future. Sensitivity simulations will be carried out in a regional modeling framework using both versions of the Kain-Fritsch scheme (KF and KF_{CIN}), followed by a qualitative and quantitative examination of the role of negative buoyancy. Note that the importance of the free-tropospheric (above boundary layer) forcing for parameterizing propagating convection has been demonstrated not only for midlatitude nocturnal convection but also in the tropics (Liang et al. 2004; Zhang et al. 2003; Lee et al. 2008; Zhou et al. 2012). For example, Zhou et al. (2012) suggested that the slow-occurring, free-tropospheric moistening is important to delay deep convection

associated with eastward propagating MJOs in the tropics. They showed that by employing the dilute plume approximation which inhibits deep convection in the Zhang and McFarlane scheme (Zhang and McFarlane 1995), it is possible to improve the MJO simulation. In the future, I will compare the ability of the revised Kain-Fritsch scheme (KF_{CIN}) to improve MJO simulations in a similar way, but by using the strict negative buoyancy trigger criterion to delay deep convection.

5.2.2 Exploring the regional variability in large-scale convective forcing mechanisms

Even after explicitly considering parcel buoyancy below the LFC, the large-scale forcing such as moisture flux convergence (Kuo 1974), horizontal mass convergence (Kain 2004), moisture advection (Tiedtke 1989), will have a significant influence on parameterized convection in mesoscale models. The sensitivity to this forcing is evident in the prominent differences observed between the KF and KF_{MA} simulations (section 2.3.8). This research has shown that thermodynamic constraints may reduce this sensitivity by a small amount, but understanding the variability in dynamical processes appears to be much more crucial for the accurate representation of warm season rainfall in mesoscale models. The relevant trigger mechanisms in midlatitudes, tropics, dry regions, and wet regions, must be clearly understood in order for any cumulus parameterization scheme to adequately represent the geographical variability in rainfall characteristics. Kuo (1965,1974) proposed the use of moisture flux convergence (MFC) to predict convection in tropical cumulonimbus based on the flux form of the moisture budget equation as follows,

$$\frac{\partial q}{\partial t} + \nabla . q v_h + \frac{\partial qw}{\partial p} = E - P \,. \tag{5.1}$$

where the first term represents the time-rate of change in the column integrated specific humidity, the second term is the horizontal MFC (negative), the third term represents the vertical MFC (negative) in pressure coordinates, and this is balanced by the net freshwater flux at the surface. He assumed that in a tropical environment, the moisture provided to the atmosphere is condensed to form clouds and precipitation thereby allowing little scope for change in moisture storage (1st term in the LHS of Eq. 5.1). Arakawa (2004) further suggested that between the two terms contained in the expression for horizontal moisture flux convergence (see Eq. 5.2), only the advection of moisture (1st term in the RHS of Eq. 5.2) will determine the cloud buoyancy (or CAPE) through specific humidity changes that typically occur within the planetary boundary layer (for e.g., see schematic in Fig. 5.1 (a)). Thus, according to Arakawa (2004), moisture advection, as opposed to mass convergence, is useful for predicting convection.

$$\nabla.qv_h = v_h.\nabla q + q\nabla.v_h \tag{5.2}$$

Contrary to this reasoning, Banacos and Schultz (2005) recommend the forecast utility of horizontal mass convergence (proportional to the 2nd term in the RHS of Eq. 5.2) over moisture flux convergence in the midlatitudes. If it is assumed that evaporation and large-scale moisture advection directly lead to an increase in the moisture storage, then precipitation is forced simply by the product of specific humidity and the mass convergence. The authors investigate this theory through scale-analysis and several case studies, and highlight the dominance of the mass convergence term in triggering convective precipitation especially in the vicinity of mesoscale boundaries. The

increased vertical mixing due to mass convergence may easily over come low-level CIN, and thereby trigger convection in the presence of CAPE (for e.g., see schematic in Fig. 5.1 (b)). Both scenarios illustrated by the schematic in Fig 5.1 seem plausible as a forcing mechanism to initiate sub-grid scale convection, but it is reasonable to expect variability in their control. For example, the CAPE changes through moisture advection (analogous to Type II instability) may be suitable for elevated convection occurring above the boundary layer, whereas removal of CIN through mass convergence (Type I instability) appears to be significant for surface-based or PBL-based convection. Thus, although the present research has demonstrated that proper thermodynamic considerations can reduce the sensitivity to the dynamical forcing, it is not yet clear that a single cumulus scheme can be used to model all types of convection.

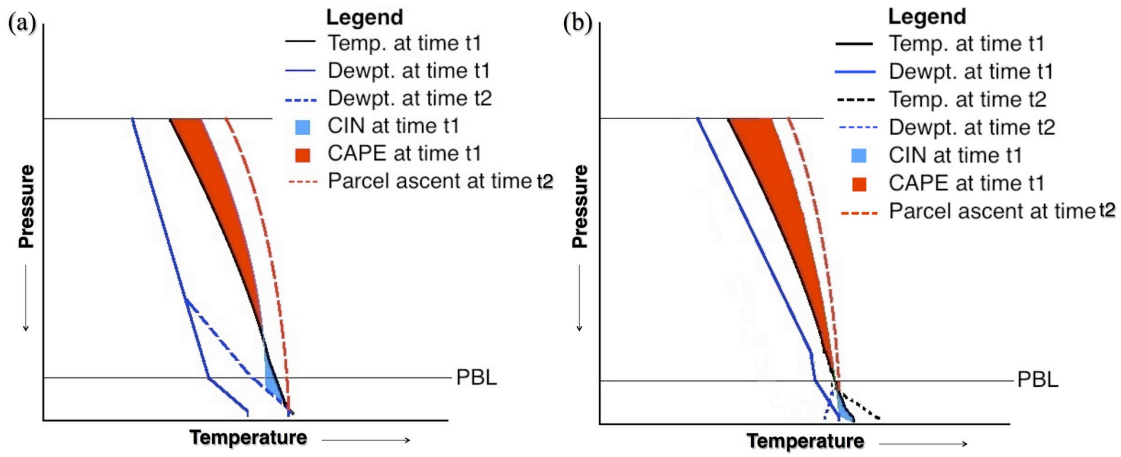

Figure 5.1 Schematic representing the development of parcel instability through (a) low-level moisture advection leading to build-up of CAPE, and (b) mass convergence leading to vertical mixing within the PBL (removal of CIN).

By separately considering large-scale convective forcing mechanisms based on the tendency for CAPE changes through moisture advection (Type II) and CIN removal through mass convergence (Type I), it may be possible to identify the regions or regimes that are sensitive to each type of instability. For this purpose, using convective and pre-convective satellite-derived soundings as described in section 2.2.5, I will distinguish between the two processes that are shown in Fig. 5.1. In regions where both mechanisms are found to be important, the total MFC (LHS of Eq. 5.2) will be examined as a potential trigger for convection. Regionally classified datasets of satellite-derived soundings will be prepared for dry and wet regions in both the midlatitudes and the tropics. Similarly, the influence of the forcing mechanism will be separately evaluated for surface-based and elevated convection episodes. Principal component analyses will be performed on the differences between convective and pre-convective soundings for each region (and regime) in order to identify the dominant trigger mechanism based on empirical orthogonal functions (EOFs). The aim is to broadly classify regions (wet versus dry, midlatitudes versus tropics) and regimes (boundary layer versus elevated convection) based on the dominance of horizontal mass convergence, moisture advection, or both large-scale trigger mechanisms.

The observations will then be used to validate and improve the performance of cumulus schemes. For example, both dynamical trigger versions of the Kain-Fritsch scheme (KF and KF_{MA}) can be tested and modified based on the observed characteristics. From the present study, it appears that for wet, coastal midlatitude regions such as the Chesapeake Bay watershed, the mass convergence forcing may work well. The atmosphere over wet regions is more likely to have high moisture

content and a presence of instability (CAPE). Therefore, a lifting mechanism (mass convergence) may be sufficient to trigger convection (as observed in Fig. 2.8). This is probably the reason that the Kain-Fritsch scheme (KF) performs better in simulating convection over the Southeast US compared to KF_{MA} (Fig. 2.13 - 2.15). In drier midlatitude regions, since both atmospheric humidity and CAPE will be comparatively less, large scale moisture advection may be necessary to increase the specific humidity of the atmospheric column in order for convection to occur. Mesoscale boundaries may not be adequate to predict convection in these regions. Note that this might explain the poor representation of the phase of convection over southern Texas and the weaker amplitude over western US by the KF scheme. In comparison, the KF_{MA} scheme performs reasonably better (Fig. 2.14 and 2.15). Thus, moisture advection may be a more potent trigger mechanism for drier regions. Similarly, for elevated convection occurring above the PBL, mid-tropospheric moistening due to advection of moisture (for e.g., from low-level jets) may be the dominant trigger mechanism. In the tropics, convection is known to be sensitive to moisture flux convergence (Kuo 1965,1974). The relative dominance of each of the terms in Eq. 5.2 will be similarly investigated.

The variability in the trigger mechanisms for dry versus wet midlatitude regions is evident in the distribution of warm season precipitation events (1-day, 2-day, etc.). For the wet Southeast US, such a distribution yields a broad peak in the duration days (for 2-day, 3-day, 4-day and 5-day events). On the other hand, the distribution of total duration days has a narrow peak (for 1-day events) in the dry Southwest US. This may point to differences in the trigger for convection in both

regions. The narrower peak in the distribution of vertically integrated moisture flux convergence (MFC) events suggests moisture advection may initiate rainfall events over the southwest, but mechanisms other than MFC (perhaps mass convergence) may be important for triggering convection in the southeast.

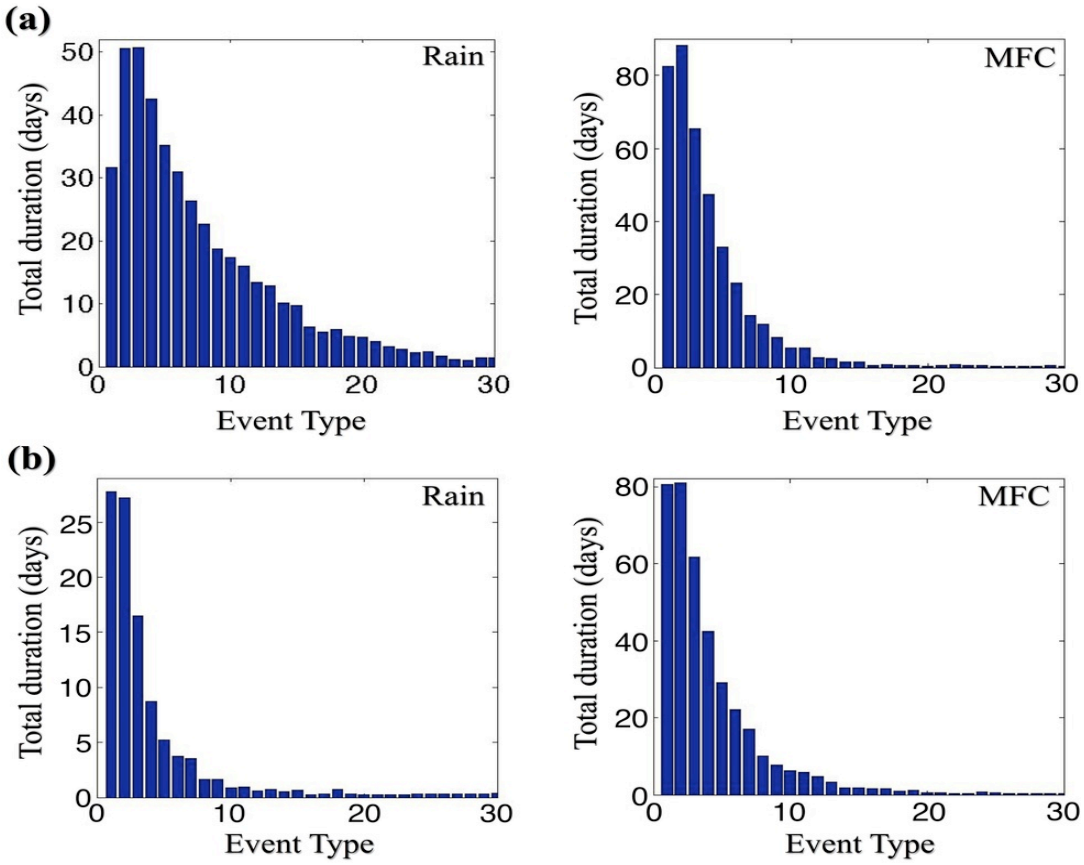

Figure 5.2 The distribution of precipitation events (left panel) and positive MFC events (right panel) based on total duration (days) associated with each event type (1-day, 2-day, etc.) for (a) Southeast US, and (b) Southwest US. The data is obtained from NARR (JJA; 2002-2010).

Therefore, the use of remote-sensing observations as well as modeling studies can help delineate the dominance of the varying large-scale convective trigger mechanisms in dry versus wet regions. Apart from satellite soundings, field observations from programs such as the Dynamics of the Madden-Julian Oscillation (DYNAMO) and the

Year of Tropical Convection (YOTC), may also be used to verify the relative importance of moisture advection, mass convergence and MFC as convective forcing mechanisms. A second study will be performed to investigate the applicability of the identified forcing variables to improve regional predictions of extreme warm season rainfall (such as drought, floods). For example, the interannual variability of drought conditions can be very different for a dry compared to a wet region (Seager et al. 2009). Therefore, apart from improving the representation of warm season rainfall climatology in cumulus schemes, the outcome of this research will also be used to enhance the confidence of seasonal forecasts for different regions.

5.2.3 Investigating urban processes that increase nocturnal thunderstorm frequency over cities

In Chapters 3 and 4, it was observed that urban mechanisms (especially UHI) may lead to a local increase in the frequency of nocturnal thunderstorms. Since most cities record a nocturnal UHI, and may therefore also experience more frequent storms than their surrounding rural regions, the results have consequences for local weather forecasting, urban planning, rainwater harvesting, etc. In the future, while planning for the reduction of urban induced weather modification, it is important to have quantitative estimates of the role of the various urban related processes in producing local rainfall increase. In Chapter 4, the UHI and the urban surface roughness were identified as important mechanisms for enhanced local convergence during storm events. The relative contribution of each process will be quantified using additional model sensitivity experiments. For example, the frequent nudging of urban temperatures to match background rural values in model simulations may be carried out, thereby diminishing the effect of the UHI and making it possible to study urban

roughness impacts on nocturnal storms. Alternatively, forcing a thermal perturbation over the rural land cover by nudging low-level temperatures to match urban values may also be useful. These sensitivity experiments will be used to quantify the relative significance of the UHI and the enhanced surface roughness in steering storm cells towards urban areas.

Moreover, the evidence and mechanism for nocturnal downwind rainfall intensification was only explored partially in the current study. Although a positive UHA may occur in the nocturnal atmosphere, its downstream propagation and consequent role in rainfall enhancement needs further investigation in the future. For this purpose, additional observational datasets and model sensitivity analyses will be used once again.

5.2.4 Understanding the relation between UHI-sea breeze interaction and extreme rainfall for coastal cities

In Chapter 3, it was seen that the UHI may interact with the local sea breeze circulation to produce extreme positive rainfall anomalies over coastal urban regions. Such a UHI impact appears to generate more intense and frequent anomalous precipitation for coastal cities (compared to inland cities). Since a large number of major, populous cities across the world are situated along continental coastlines, it is necessary to understand the mechanism for the increase in extreme rainfall events. This will be crucial for urban planning activities such as flood risk reduction, water resources management, and so on. Using a similar model sensitivity analyses, the UHI-sea breeze interaction and its role in producing extreme positive rainfall anomalies over the urban region will be investigated in the future.

Appendix

The location indices for atmospheric soundings discussed in Chapter 2 are given in the following tables.

Table A1 Location indices for skew T-log P soundings derived using AIRS satellite retrievals, shown in Figure 2.8.

Position / Figure	Top Left		Top Right		Bottom Left		Bottom Right	
	Latitude	Longi-tude	Latitude	Longi-tude	Latitude	Longi-tude	Latitude	Longi-tude
2.8 (a)	37.0732	-78.957	38.8631	-77.8195	36.3724	-79.3271	38.8238	-77.655
2.8 (b)	38.4320	-78.3142	40.5766	-77.5498	39.8232	-77.2065	38.7572	-78.0825

Table A2 Location indices for skew T-log P soundings obtained from model output, shown in Figures 2.9, 2.10 and 2.11.

Position / Figure	Left		Center		Right	
	Latitude	Longitude	Latitude	Longitude	Latitude	Longitude
2.9 (a)	42.2419	-75.3772	41.8283	-75.7923	41.8283	-75.7923
2.9 (b)	43.3083	-75.5002	42.8947	-75.9213	42.8947	-75.9213
2.9 (c)	39.7047	-78.8835	39.2790	-79.2627	39.2790	-79.2627
2.10 (a)	40.8404	-73.5166	40.4327	-73.9343	40.4327	-73.9343
2.10 (b)	40.0855	-76.9700	39.6660	-77.3629	39.6660	-77.3629
2.11	41.6672	-74.1617	-	-	41.2575	-74.5807

Bibliography

Accadia, C., S. Mariani, M. Casaioli, A. Lavagnini, and A. Speranza, 2003: Sensitivity of Precipitation Forecast Skill Scores to Bilinear Interpolation and a Simple Nearest-Neighbor Average Method on High-Resolution Verification Grids. *Wea. Forecasting,* **18**, 918-932.

Ackerman, B. and co-authors, 1977: Causes of Precipitation Anomalies: In summary of METROMEX Vol. 2, *Illinois State Water Survey Bulletin,* **62**, 260 pp.

Andreae, M. O., D. Rosenfeld, P. Artaxo, A. A. Costa, G. P. Frank, K. M. Longo, and M. A. F. Silva-Dias, 2004: Smoking rain clouds over the Amazon. *Science*, **303**, 1337–1341.

Arakawa, A., 1969: Parameterization of cumulus clouds. *Proc. Symp. on Numerical Weather Prediction, WMO/International Union of Geodesy and Geophysics, Tokyo, Japan,* pp. 1–6.

Arakawa, A., and W. H. Schubert, 1974: Interaction of a cumulus cloud ensemble with the large- scale environment, part I. *J. Atmos. Sci.,* **31**, 674 – 701.

_____, 2004: The cumulus parameterization problem: Past, present, and future. *Journal of Climate*, **17**(13), 2493-2525.

Ashley, W. S., Bentley, M. L., & Stallins, J. A., 2012: Urban-induced thunderstorm modification in the Southeast United States. *Climatic change*,**113**(2), 481-498.

Baik, J.-J., Y. H. Kim, and H. Y. Chun, 2001: Dry and moist convection forced by an urban heat island, *J. Appl. Meteor.,* **40**, 1462–1475.

Baldwin, M. E., and K. E. Mitchell, 1996: The NCEP hourly multi-sensor U.S. precipitation analysis. Preprints, *Conference on Weather Analysis and Forecasting, Norfolk, VA.*

____, J. S. Kain, and M. P. Kay, 2002: Properties of the convection scheme in NCEP's Eta Model that affect forecast sounding interpretation. *Wea. Forecasting*, **17**, 1063-1079.

Banacos, P. C. and D. M. Schultz, 2005: The use of moisture flux convergence in forecasting convective initiation: Historical and operational perspectives. *Wea. Forecasting,* **20**, 351-366.

Barbato, J. P., 1978: Areal parameters of the sea breeze and its vertical structure in the Boston basin. *Bull. Amer. Meteor. Soc*., **59**, 1420–1431.

Bechtold, P., Semane, N., Lopez, P., Chaboureau, J. P., Beljaars, A., & Bormann, N., 2013: Representing equilibrium and non-equilibrium convection in large-scale models. *Journal of the Atmospheric Sciences*.

Bentley, M. L., Ashley, W. S., and Stallins, J. A., 2010: Climatological radar delineation of urban convection for Atlanta, Georgia. *International Journal of Climatology*, **30**(11), 1589-1594.

Betts, A. K., 1986: A new convective adjustment scheme. Part I: Observational and theoretical basis. *Quart. J. Roy. Meteor. Soc.,* **112,** 677–691.

___, and M. J. Miller, 1986: A new convective adjustment scheme. Part II: Single column tests using GATE wave, BOMEX, and arctic air-mass data sets. *Quart. J. Roy. Meteor. Soc.,* **112**, 693–709.

___, and C. Jakob, 2002: Evaluation of the diurnal cycle of precipitation, surface thermodynamics, and surface fluxes in the ECMWF model using LBA data. *Journal of Geophysical Research,* **107**, D20, 8045, doi:10.1029/2001JD000427

Boatman, J. F., and A. H. Auer, Jr., 1974a: Inadvertent thunderstorm modification by an urban area. *Fifth Conference on Weather Forecasting and Analysis, AMS, Boston,* pp. 183-188.

_____, and _____, 1974b: Inadvertent thunderstorm modification by an urban area. *Fourth Conference on Weather Modification, AMS, Boston,* pp. 366-373.

Bornstein, R. D., and M. LeRoy, 1990: Urban barrier effects on convective and frontal thunderstorms, Preprints, *Conf. on Mesoscale Processes, Boulder, CO, Amer. Meteor. Soc*. 25–29.

_____, and Q. Lin, 2000: Urban heat islands and summertime convective thunderstorms in Atlanta: Three cases studies, *Atmos. Environ*., **34**, 507–516.

_____, and W. T. Thompson, 1981: Effects of frictionally retarded sea breeze and synoptic frontal passages on sulfur dioxide concentrations in New York City. *J. Appl. Meteor*., **20**, 843–858.

Campbell, M, 1991: Equivalent Potential Temperature (Theta-e) Applications. *Western Region Technical Attachment*, **91**, 37.

Chandler, T. J., 1967: Night-time temperatures in relation to Leicester's urban form, *Meteorol. Mag.,* **96,** 244-250.

Changnon, S. A., 1968: The LaPorte weather anomaly—Fact or fiction? *Bull. Amer. Meteor. Soc.,* **49,** 4–11.

_____, F. A. Huff, P. T. Schickedanz, and J. L. Vogel, 1977: Weather anomalies and impacts: In summary of METROMEX Vol. I, *Illinois State Water Survey Bulletin,* **62,** 260 pp.

_____, R. G. Semonin, A. H. Auer, R. R. Braham, and J. Hales, 1981: METROMEX: A Review and Summary. *Meteor. Monogr.*, **40**, 81 pp.

_____, and F. A. Huff, 1986: The Urban-related Nocturnal Rainfall Anomaly at St. Louis. *Journal of Climate and Applied Meteorology*, **25**, 1985-1995.

Chen, F., and J. Dudhia, 2001: Coupling an advanced land-surface/ hydrology model with the Penn State/ NCAR MM5 modeling system. Part I: Model description and implementation. *Mon. Wea. Rev.*, **129**, 569–585.

Chen, F., M. Tewari, H. Kusaka, and T. T. Warner, 2006: Current status of urban modeling in the community Weather Research and Forecast (WRF) model. *Joint with Sixth Symposium on the Urban Environment and AMS Forum: Managing our Physical and Natural Resources: Successes and Challenges, Atlanta, GA, USA*, Amer. Meteor. Soc., CD-ROM. J1.4.

Colby Jr, F. P. 1984: Convective Inhibition as a Predictor of Convection during AVE-SESAME II. *Mon. Wea. Rev.*, **112**, 2239-2252.

Colman, B. R., 1990: Thunderstorms above frontal surfaces in environments without positive CAPE. Part I: A climatology. *Mon. Wea. Rev.,* **118**, 1103–1122.

Dai, A. F., and K. E. Trenberth, 2004: The Diurnal Cycle and its Depiction in the Community Climate System Model. *Journal of Climate,* **17**, 930-95.

Davies, L., Plant, R. S., & Derbyshire, S. H., 2013: Departures from convective equilibrium with a rapidly varying surface forcing. *Quarterly Journal of the Royal Meteorological Society*.

Davis, C. A., Brown, B. G., Bullock, R., & Halley-Gotway, J., 2009: The method for object-based diagnostic evaluation (MODE) applied to numerical forecasts from the 2005 NSSL/SPC Spring Program. *Weather and Forecasting*, **24**(5), 1252-1267.

Development Testbed Center, 2009: MET Version 2.0 Model Evaluation Tools Users Guide. [Available online at *http://www.dtcenter.org/met/users/docs/overview.php*].

Diaconis, P., and B. Efron, 1983: Computer-intensive methods in statistics. *Sci. Amer.,* **248,** 116-130.

Diem, J. E., and D. P. Brown, 2003: Anthropogenic impacts on summer precipitation in central Arizona, U.S.A. *Prof. Geogr.,* **55,** 343–355.

Dirmeyer, P. A., and Coauthors, 2010: Simulating the hydrologic diurnal cycle in global climate models: Resolution versus parameterization. A Technical Report from Center for Ocean-Land-Atmosphere Studies, American Meteorological Society, **304**, 45 pp.

Dixon, P. G., and T. L. Mote, 2003: Patterns and causes of Atlanta's urban heat island-initiated precipitation. *J. Appl. Meteor.,* **42**, 1273–1284.

Draxler, R. R., 1986: Simulated and observed influence of the nocturnal urban heat island on the local wind field. *Journal of climate and applied meteorology*, **25**(8), 1125-1133.

Duckworth, F. S., and J. S. Sandberg, 1954: The effect of cities upon horizontal and vertical temperature gradients, *Bull. Amer. Meteor. Soc.,* **35**, 198–207.

Emanuel, K. A., 1994: *Atmospheric Convection*. New York: Oxford Univ. Press. 580 pp.

Farina, K. J., and J. T. DiStefano, 1998: A case of severe elevated convection over the Ohio Valley on March 22-23, 1995. Eastern Region Technical Attachment, **98**, 2.

Flood, S., 2004: Preferred Thunderstorm Patterns over the DC-Baltimore area. *Washington-Baltimore Climate Review.*

Freitas, E. D., Silva Dias, P. L., Carvalho, V. S. B., and co-authors, 2009: Factors involved in the formation and development of severe weather conditions over the megacity of Sao Paulo. *Eighth Symposium on the Urban Environment, AMS, Phoenix.*

Fritsch, J. M., and C. F. Chappell, 1980: Numerical prediction of convectively driven mesoscale pressure systems. Part 1: Convective parameterization. *J. Atmos. Sci.,* **37**, 1722-1733.

Givati, A., and D. Rosenfeld, 2004: Quantifying precipitation suppression due to air pollution. *J. Appl. Meteor*., **43**, 1038–1056.

Goforth, M. A., Gilcrest, G. W., Sirianni, J. D., 2002: Cloud Effects on Thermal Downwelling Sky Radiance, *SPIE*, **4710**.

Graham, I. R., 1968: An analysis of turbulence statistics at Fort Wayne, Indiana. *Journal of Applied Meteorology*, **7**(1), 90-93.

Grell, A. G., 1988: Semi-prognostic tests of cumulus parameterization schemes in the middle latitudes. Ph.D. dissertation, University of Miami, 225 pp.

_____, Y.-H. Kuo, and R. J. Pasch, 1991: Semiprognostic tests of cumulus parameterization schemes in the middle latitudes. *Mon. Wea. Rev.*, **119**, 5–30.

_____, 1993: Prognostic evaluation of assumptions used by cumulus parameterizations, *Mon. Weather Rev.,* **121**, 764–787.

Grimmond, C. S. B., and T. R. Oke, 1995: Comparison of heat fluxes from summertime observations in the suburbs of four North American cities, *J. Appl. Meteor.,* **34**, 873–889.

_____, and _____, 1999a: Heat storage in urban areas: Localscale observations and evaluation of a simple model, *J. Appl. Meteor*., **38**, 922–940.

_____, and _____, 1999b: Evapotranspiration rates in urban areas, Proceedings, *Impacts of Urban Growth on Surface Water and Groundwater Quality Symposium, Birmingham.*

_____, and _____, 2002: Turbulent heat fluxes in urban areas: Observations and a local-scale urban meteorological parameterization scheme (LUMPS), *J. Appl. Meteor.,* **41**, 792–810.

Hjemfelt, M. R., 1982: Numerical simulation of the effects of St. Louis on mesoscale boundary layer airflow and vertical motion: Simulations of urban vs. non-urban effects. *J. Appl. Meteor.,* **21**, 1239–1257.

Holtzman, B. G., and H. C. S. Thom, 1970: The La Porte precipitation anomaly. *Bull. Amer. Meteor. Soc*., **51,** 335–337.

Homer, C.H., Fry, J.A., and Barnes C.A., 2012: The National Land Cover Database, U.S. Geological Survey Fact Sheet 2012-3020, 4 p.

Hong, S., J. Dudhia, and S. Chen, 2004: A Revised Approach to Ice Microphysical Processes for the Bulk Parameterization of Clouds and Precipitation. *Mon. Wea. Rev.,* **132**, 103–120.

___, and J. J. Lim, 2006: The WRF Single-Moment 6-Class Microphysics Scheme (WSM6). *Journal of the Korean Meteorological Society,* **42**, 129–151.

____, Y. Noh, and J. Dudhia, 2006: A new vertical diffusion package with an explicit treatment of entrainment processes. *Mon. Wea. Rev.,* **134**, 2318–2341.

Huff, F. A. and S. A. Changnon, Jr., 1973: Precipitation modification by major urban areas, *Illinois State Water Survey Bulletin*, **54,** 1220-1232.

_____, and _____, 1972: Climatological assessment of urban effects on precipitation at St. Louis. *J. Appl. Meteor.,* **11**, 823–842.

Imhoff, M. L., P. Zhang, R. E. Wolfe, and L. Bounoua, 2010: Remote sensing of the urban heat island effect across biomes in the continental USA, *Remote Sensing of Environment,* **114**, 504-513.

Janjić, Z. I., 1994: The step-mountain eta coordinate model: further developments of the convection, viscous sublayer and turbulence closure schemes. *Mon. Wea. Rev.,* **122**, 927–945.

Jones, T. R., & Randall, D. A., 2011: Quantifying the limits of convective parameterizations. *Journal of Geophysical Research: Atmospheres (1984–2012)*, **116** (D8).

Kain, J. S., and J. M., Fritsch, 1992: The role of the convective "trigger function" in numerical forecasts of Mesoscale Convective Systems. *Meteorol. Atmos. Phys*., **49**, 93-106.

____, and ____, 1993: Convective parameterization in mesoscale models: The Kain-Fritsch scheme, in The Representation of Cumulus Convection in Numerical Models. *Meteorol. Monogr.*, **46,** 165 – 170.

____, 2004: The Kain-Fritsch Convective Parameterization: An Update. *Journal of Applied Meteorology,* **43**, 170-181.

Keeler, Jason M., David A. R. Kristovich, 2012: Observations of Urban Heat Island Influence on Lake-Breeze Frontal Movement. *J. Appl. Meteor. Climatol.,* **51**,702–710.

Kuo, H. L., 1965: On formation and intensification of tropical cyclones through latent heat release by cumulus convection. *J. Atmos. Sci*., **22**, 40–63.

_____, 1974: Further studies of the parameterization of the influence of cumulus convection on large-scale flow. *J. Atmos. Sci.,* **31**, 1232– 1240.

Kusaka, H., F. Kimura, H. Hirakuchi, and M. Mizutori, 2000: The effects of land-use alteration on the sea breeze and daytime heat island in the Tokyo metropolitan area. *J. Meteor. Soc. Japan*, **78**, 405–420.

_____, H. Kondo, Y. Kikegawa, and F. Kimura, 2001: A simple single-layer urban canopy model for atmospheric models: Comparison with multi-layer and slab models. *Bound.-Layer Meteor*., **101**, 329–358.

_____, and F. Kimura, 2004: Coupling a single-layer urban canopy model with a simple atmospheric model: Impact on urban heat island simulation for an idealized case. *J. Meteor.Soc. Japan*, **82**, 67–80.

Landsberg, E. H., 1981: The urban climate. *International Geophysics Series*, **28**, pp. 5 New York: Academic Press.

Lee, D. O., 1977: Urban influence on wind directions over London. *Weather*, **32**(5), 162-170.

Lee, M.-I., and Coauthors, 2007: An Analysis of the Warm-Season Diurnal Cycle over the Continental United States and Northern Mexico in General Circulation Models. *Journal of Hydrometeorology*, **8**, 344-366.

_____, S. D. Schubert, M. J. Suarez, J.-K. E. Schemm, H.-L. Pan, J. Han, and S.-H. Yoo, 2008: Role of convection triggers in the simulation of the diurnal cycle of precipitation over the United States Great Plains in a general circulation model. *J. Geophys. Res.*, **113**, D02111, doi:10.1029/2007JD008984.

Liang, X., L. Li, A. Dai, and K. E. Kunkel, 2004: Regional climate model simulation of summer precipitation diurnal cycle over the United States. *Geophysical Research Letters,* **31**, L24208, doi:10.1029/2004GL021054.

Lin, Y., and K. E. Mitchell, 2005: The NCEP Stage II/IV Hourly Precipitation Analyses: Development and Applications. Proceedings, *19th AMS Conference on Hydrology, San Diego, CA.*

Loughner, Christopher P., Dale J. Allen, Da-Lin Zhang, Kenneth E. Pickering, Russell R. Dickerson, Laura Landry, 2012: Roles of Urban Tree Canopy and Buildings in Urban Heat Island Effects: Parameterization and Preliminary Results. *J. Appl. Meteor. Climatol.*, **51**, 1775–1793.

Ma, L-M. and Tan Z-M, 2009: Improving the behavior of cumulus parameterization for tropical cyclone prediction: Convective trigger. *Atmospheric Research*, **92**, 190-211.

Manabe, S., J. Smagorinsky, and R. F. Strickler, 1965: Simulated climatology of a general circulation model with a hydrological cycle. *Mon. Wea. Rev.,* **93,** 769–798.

Manuel S. F and others, 2011: The Real-Time Mesoscale Analysis at NOAA's National Centers for Environmental Prediction: Current Status and Development. *Weather and Forecasting,* **26**, 593–612.

Martilli, A., A. Clappier and M.W. Rotach, 2002: 'An urban surface exchange parameterisation for mesoscale models'. *Boundary-Layer Meteorology* 104.2, pp. 261-304.

Masunaga, H., 2012: A satellite study of the atmospheric forcing and response to moist convection over tropical and subtropical oceans. *J. Atmos. Sci.,* **69**, 150– 167.

Mellor, G. L., and T. Yamada, 1982: Development of a turbulence closure model for geophysical fluid problems. *Rev. Geophys. Space Phys.*, **20**, 851–875.

Mesinger, F. and Coauthors, 2006: North American Regional Reanalysis. *Bull. Amer. Meteor. Soc.,* **87**, 343-360.

Molders, N., and M. A. Olson, 2004: Impact of urban effects on precipitation in high latitudes. *J. Hydrometeor.,* **5**, 409–429.

Monin, A.S. and A.M. Obukhov, 1954: Basic laws of turbulent mixing in the surface layer of the atmosphere. *Contrib. Geophys. Inst. Acad. Sci*., USSR, **151**, 163–187 (in Russian).

Morris, C. J. G., I. Simmonds, and N. Plummer, 2001: Quantification of the influences of wind and cloud on the nocturnal urban heat island of a large city, *J. Appl. Meteor.,* **40**, 169–182.

Niyogi, Dev, Patrick Pyle, Ming Lei, S. Pal Arya, Chandra M. Kishtawal, Marshall Shepherd, Fei Chen, Brian Wolfe, 2011: Urban Modification of Thunderstorms: An Observational Storm Climatology and Model Case Study for the Indianapolis Urban Region. *J. Appl. Meteor. Climatol.*, **50**, 1129–1144.

Oke, T.R., 1973: City size and the urban heat island, *Atmospheric Environment*, **7,** 769-779.

_____, 1982: The energetic basis of the urban heat island, Quart. *Journal of the Royal Meteorological Society,* **108**, 1-24.

_____, 1988: The urban energy balance, *Progress Phys. Geogr*., **12**, 471–508.

Oleson, K. W., G. B. Bonan, J. Feddema, M. Vertenstein, 2008: An Urban Parameterization for a Global Climate Model. Part II: Sensitivity to Input Parameters and the Simulated Urban Heat Island in Offline Simulations, *J. Appl. Meteor. Climatol*., **47,** 1061–1076.

Ohashi, Y., and H. Kida, 2002: Local circulations developed in the vicinity of both coastal and inland urban areas: Numerical study with a mesoscale atmospheric model. *J. Appl. Meteor.,* **41**, 30–45.

Perryman, Nyssa, and Dixon D. G., 2013: A Radar Analysis of Urban Snowfall Modification in Minneapolis-St. Paul. *Journal of Applied Meteorology and Climatology,* (2013).

Ramanathan, V., P. J. Crutzen, J. T. Kiehl, and D. Rosenfeld, 2001: Aerosols, climate, and the hydrological cycle. *Science***, 294**, 2119–2124.

Rosenfeld, D., 1999: TRMM observed first direct evidence of smoke from forest fires inhibiting rainfall. *Geophys. Res. Lett*., **26,** 3105–3108.

_____, 2000: Suppression of rain and snow by urban air pollution. *Science*, **287**, 1793–1796.

_____, and co-authors, 2008: Flood or drought: how do aerosols affect precipitation? *Science,* **321** (5894), 1309-1313.

Schubert, S., 2010: Implementation and testing of the building energy parameterization model (BEP) in the Climate Local Model (CLM). Preprints, *Ninth Symposium on the Urban Environment, Keystone, CO*.

Seager, R., Tzanova, A., & Nakamura, J., 2009: Drought in the southeastern United States: causes, variability over the last millennium, and the potential for future hydroclimate change. *Journal of Climate*, **22**(19), 5021-5045.

Shepherd, J. M., H. Pierce, and A. J. Negri, 2002: Rainfall modification by major urban areas: Observations from spaceborne rain radar on the TRMM satellite. *J. Appl. Meteor.,* **41**, 689–701.

_____, and S. J. Burian, 2003: Detection of urban-induced rainfall anomalies in a major coastal city. *Earth Interactions,* **7**.

_____, 2005: A Review of Current Investigations of Urban-Induced Rainfall and Recommendations for the Future. *Earth Interactions,* **9**, 12.

Sheridan, S.C., L.S. Kalkstein, and J.M. Scott, 2000: An evaluation of the variability of air mass character between urban and rural areas, *Biometeorology and Urban Climatology at the turn of the Millennium*, World Meteorological Organization, 487-490.

Shreffler, J. H., 1978: Detection of centripetal heat-island circulations from tower data in St. Louis. *Boundary-Layer Meteorology*, **15**(2), 229-242.

Skamarock, W. C., and Coauthors, 2008: A description of the Advanced Research WRF version 3. NCAR Tech Note NCAR/TN-475+STR, 113 pp.

Smith, G. S., 1993: A case study of a fast moving snowstorm in Central Ohio on January 25, 1992. Eastern Region Technical Attachment, **93**, 7B.

Smith, W. L., E. Weisz, S. Kirev, D. K. Zhou, Z. Li, and E. E. Borbas, 2012: Dual-regression retrieval algorithm for realtime processing of satellite ultraspectral radiances. *J. Appl. Meteor. Climatol*., **51**, 1455–1476.

Sundborg, A., 1950: Local climatological studies of the temperature conditions in an urban area, *Tellus,* **2**, 222–232.

Swinbank, W.C., 1963: Long-wave Radiation from Clear Skies, *Quart. Journal of the Royal Meteorological Society of London,* **89**.

Tiedtke, M., 1989: A comprehensive mass flux scheme for cumulus parametrization in large-scale models. *Mon. Wea. Rev.,* **117**, 1779–1800.

The National Center for Atmospheric Research, 2012: The NCAR Command Language Version 6.0. UCAR/NCAR/CISL/VETS.

Van Den Heever, Susan C., and William R. Cotton, 2007: Urban aerosol impacts on downwind convective storms. *Journal of Applied Meteorology and Climatology,* **46** (6), 828-850.

Vukovich, F. M., and J. W. Dunn, 1978: A theoretical study of the St. Louis heat island: Some parameter variations. *J. Appl. Meteor.,* **17,** 1585–1594.

Wallace, J. M., 1975: Diurnal variations in precipitation and thunderstorm frequency over the conterminous United States. *Mon. Wea. Rev.,* **103**, 406–419.

Wan, Z. and J. Dozier, 1996: A generalized split-window algorithm for retrieving land-surface temperature from space, *IEEE Trans. Geosci. Remote Sens*., **34**, 4, pp. 892-905.

Weisz, E., H.-L. Huang, J. Li, E. Borbas, K. Baggett, P. Thapliyal, and L. Guan, 2007a: International MODIS and AIRS processing package: AIRS products and applications. *Journal of Applied Remote Sensing*, **1**, 013519.

_____, J. Li, D. K. Zhou, H.-L. Huang, M. D. Goldberg, P. Yang, 2007b: Cloudy sounding and cloud-top height retrieval from AIRS alone single field-of-view radiance measurements. *Geophysical Research Letters*, **34**, L12802.
Westcott, Nancy E, 1995: Summertime cloud-to-ground lightning activity around major Midwestern urban areas. *Journal of Applied Meteorology*, **34** (7), 1633-1642.

Western Regional Climate Center, 2013: "Monthly Precipitation Totals - Sacramento 5 ESE". http://www.wrcc.dri.edu/cgi-bin/cliMAIN.pl?ca7633 (21/2/2013).

Wong, K. K., & Dirks, R. A., 1978: Mesoscale perturbations on airflow in the urban mixing layer. *Journal of Applied Meteorology*, **17**(5), 677-688.

Yoshikado, H., and H. Kondo, 1989: Inland penetration of the sea breeze over the suburban area of Tokyo. *Bound.-Layer Meteor*., **48**, 389–407.

_____ 1994: Interaction of the sea breeze with urban heat islands of different sizes and locations. *J. Meteor. Soc. Japan,* **72,** 139–142.

Zhang, D., Y. Shou, and R. Dickerson, and F. Chen, 2011: Impact of Upstream

Urbanization on the Urban Heat Island Effects along the Washington–Baltimore Corridor. *Journal of Applied Meteorology and Climatology,* **50**, 2012-2029.

Zhang, G. J., and N. A. McFarlane, 1995: Sensitivity of climate simulations to the parameterization of cumulus convection in the Canadian Climate Centre general circulation model, *Atmos. Ocean,* **33**, 407–446.

_____, 2002: Convective quasi-equilibrium in midlatitude continental environment and its effect on convective parameterization. *Journal of Geophysical Research,* **107,** D14, doi:10.1029/2001JD001005.

_____, 2003: Roles of tropospheric and boundary layer forcing in the diurnal cycle of convection in the U.S. southern great plains. *Geophys. Res. Lett.*, **30**, 2281, doi:10.1029/2003GL018554, 24.

Zhou, Lei, Richard B. Neale, Markus Jochum, Raghu Murtugudde, 2012: Improved Madden–Julian Oscillations with Improved Physics: The Impact of Modified Convection Parameterizations. *J. Climate*, **25**, 1116–1136.